DISSERTATION

Titel der Dissertation

Mineralogical studies on zircon

Verfasser

Mag. Tamás Váczi

angestrebter akademischer Grad

Doktor der Naturwissenschaften (Dr. rer. nat.)

Wien, 2009

Studienkennzahl lt. Studienblatt: A 091 427

Dissertationsgebiet lt. Studenblatt: Mineralogie–Kristallographie

Betreuer: Univ.-Prof. Dr. Lutz Nasdala

Abstract

This work summarises the results of seven studies in the area of zircon research. The studies span a broad range of phenomena, namely (i) the Raman spectroscopic properties of zircon under high pressure, (ii) the causes of low electron microprobe analytical totals and back-scattered electron (BSE) yields in zircon, (iii) radionuclide mobility scenarios in altered zircon, (iv) the factors influencing the thermal decomposition of zircon, (v) Fe incorporation in zircon, and finally the effects of (vi) He-ion irradiation and (vii) of electron beam microanalysis on existing self-irradiation damage in zircon. The discussion of the research and its results is preceded by a summarising introduction to zircon and a brief description of the various analytical techniques applied.

The high-pressure study (Appendix 1) helps to understand vibrational spectra of radiation-damaged zircon under pressure. It was found that the band width of the zircon $v_3(SiO_4)$ asymmetric stretching vibration, which indicates the degree of radiation damage, is largely unaffected by compression. This result established that Raman analysis of (potentially strain-affected) zircon inclusions in gemstones is able to determine whether a heat treatment has been applied to the host gem or not.

Low electron microprobe totals are measured in zircon zones where electron back-scattering is notably lowered, seen as dark, mostly irregular patches on BSE images. The study reprinted in Appendix 2 establishes the chemical and textural reasons behind these phenomena. The low-total areas were found to contain hydrous species in the wt% concentration, and to consist of a highly porous zircon material with nanometre-sized pores. Together with strongly increased non-formula element (Fe, Ca, Al *etc.*) concentrations, these results imply that the low-total and low-BSE areas were produced by a secondary alteration process in strongly radiation-damaged zones. Both the deficient analytical totals and the lowered BSE yield are explained by a combination of a decreased average atomic number, the hydrous content and the porosity.

In a case study of zircon alteration (Appendix 3) it was found that the radionuclide mobility was particularly low and did not exceed the loss of the major elements. This finding has important implications on the assessment of zircon U–Pb geochronology and the design of radioactive waste forms: the loss of actinides will not always be as high as that predicted by some hydrothermal leaching experiments.

Zircon is known, and exploited, for decomposing into oxide components during heat treatment at temperatures significantly lower than predicted by its phase diagram. Factors influencing zircon stability at 1400 °C were evaluated by a series of experiments. Results suggest that to avoid a breakdown at high temperatures the decrease of the activity of silica vapour in the reaction vessel should be avoided by a careful choice of sample containers and by the control of reactive gases in the reaction atmosphere.

Iron is a trace element in primary zircon but in altered samples it may be measured in the wt% range. A study (Appendix 5) was dedicated to the question whether Fe at high concentrations is incorporated into secondary zircon. Synthetic, Fe-doped zircon single crystals were shown to contain the majority of measured Fe as hematite. Some Fe was found in interstitial sites in the zircon lattice, whereas the substitution of lattice ions was minimal. Iron enrichment in secondary zircon, therefore, was concluded to be present as other phases.

The irradiation studies, outlined at the end of the introductory chapter, had contrasting results. Helium irradiation was found to increase radiation damage in zircon, seen through the creation of luminescence centres and Raman band broadening. The annealing of pre-existing damage was not observed. In contrast, moderate-energy electron irradiation (20 kV) was found to partially anneal radiation damage in pre-damaged zircon. Structural studies (such as micro-spectroscopy) should therefore always been done prior to the electron microprobe analysis of the same micro-areas, to avoid biased results.

This PhD project, and in particular the seven studies above, has led to new, significant results that add to our knowledge on natural zircon and its synthetic analogue. These results are documented in four published papers and one submitted manuscript, one more paper is currently in preparation. Results will prove particularly useful in the interpretation of spectroscopic and chemical analyses of zircon and in avoiding analytical artefacts and biased results. Perspective future research and experimental work and applications are also discussed.

Zusammenfassung

Die vorliegende Arbeit fasst die Ergebnisse von sieben Studien am Mineral Zirkon zusammen. Die Untersuchungen umfassen eine breite Palette von Phänomenen, wie (i) Veränderungen der Ramanspektren von Zirkon unter hohem Druck, (ii) Ursachen der an alterierten Zirkonen gelegentlich beobachteten defizienten Analysensummen und extrem niedrigen Elektronenrückstreuintensitäten, (iii) Mobilität/Stabilität von Radionukliden bei chemischen Alterationsprozessen, (iv) Ursachen der bei Ausheilungsexperimenten gelegentlich beobachteten thermische Dekomposition von Zirkon, (v) kristallchemische Effekte des Einbaus von Fe in Zirkon, und schließlich die Effekte von (vi) He-Ionen-Bestrahlung und (vii) Elektronenbestrahlung (letztere z.B. während der Elektronenstrahl-Mikrosonden-Analyse) auf die durch natürliche Selbstbestrahlung verursachten Strukturschäden in Zirkon. Der Diskussion der Forschungsergebnisse sind eine zusammenfassende Einführung zum Mineral Zirkon und eine kurze Beschreibung der verwendeten analytischen Methoden vorangestellt.

Die Ergebnisse der Druckexperimente (Anhang 1) tragen zum Verständnis der druckinduzierten Veränderungen der Ramanspektren strahlengeschädigter Zirkone bei. Es wurde festgestellt, dass die Breite der $v_3(SiO_4)$-Schwingungsbande vom Druck weitgehend unbeeinflusst ist und der Strahlenschädigungsgrad der Probe mehr oder weniger unabhängig von Druck oder Stress widerspiegelt. Eine beobachtete signifikante Schwingungsbandenverbreiterung ist damit ein zuverlässiger Indikator für Strahlenschädigung. Dieses Ergebnis ermöglicht es, Raman-Analysen zur Evaluierung von Zirkoneinschlüssen in metamorphogenen Edelsteinen zu nutzen, insbesondere um mögliche Temperaturbehandlungen zu prüfen.

Defiziente Analysensummen bei der Elektronenmikronsondenanalyse werden in solchen Bereichen des Zirkons gemessen, in welchen die Elektronenrückstreuung deutlich erniedrigt ist; diese sind in den Elektronenrückstreubildern als dunkle, meist unregelmäßige Stellen erkennbar. Die Studie in Anhang 2 beschäftigt sich mit den chemischen und texturellen Ursachen dieses Phänomens. Es wurde festgestellt, dass die durch zu niedrige Summen gekennzeichneten Bereiche Wasser im Gewichtsprozentbereich enthalten und aus einem hochporösen Zirkonmaterial mit Poren im Nanometerbereich bestehen. Zusammen mit einer stark angestiegenen Konzentration an Fremdelementen (Fe, Ca, Al *etc.*) implizieren diese Beobachtungen, dass diese Zirkonbereiche durch chemische Alteration stark strahlengeschädigter Bereiche entstanden. Sowohl die zu niedrigen analytischen Summen als auch die stark verringerte Rückstreuelektronenintensität werden durch eine Kombination von erniedrigter mittlerer Ordnungszahl, dem Wassergehalt und der Porosität erklärt.

In einer Fallstudie zur chemischen Alteration von Zirkon (Anhang 3) wurde eine besonders niedrige Mobilität der Radionuklide festgestellt, die nicht den Verlust an Hauptelementen überstieg. Diese Beobachtung hat bedeutende Auswirkungen auf die Interpretation von U-Pb Isotopenanalysen (Geochronologie) und die Entwicklung von Material für die Lagerung von radioaktivem Abfall: der Verlust von Radionukliden bei chemischen Alterationsprozessen ist längst nicht immer so erheblich wie durch einige experimentelle Studien vorhergesagt.

Es ist bekannt, dass Zirkon bei Heizexperimenten in seine Oxidkomponenten zerfallen kann, und dass dies bereits bei relativ moderaten Temperaturen erfolgt, welche jene im Phasendiagramm deutlich unterschreiten. Die Stabilität von Zirkon bei 1400 °C wurde in einer Serie von Experimenten untersucht. Die Ergebnisse deuten darauf hin, dass die Zerfallsreaktion stark von der SiO_2–Dampfaktivität im Reaktionsbehälter abhängt. Letztere sollte daher durch eine sorgfältige Auswahl der Probenbehälter und die Kontrolle der reaktiven Gase in der Reaktionsatmosphäre kontrolliert hochgehalten werden, um unbeabsichtigte Probendekomposition zu verhindern.

Eisen tritt in primärem Zirkon nur in Spurenelementkonzentrationen auf, in alterierten Proben kann es jedoch im Gewichtsprozentbereich vorliegen. Eine Studie (Anhang 5) widmete sich der Frage, ob hohe Eisenkonzentrationen in sekundären Zirkon eingebaut werden können. Es wurde gezeigt, dass synthetische, Fe-dotierte Zirkon-Einkristalle einen großen Teil des vorhandenen Eisens als Hämatit einbauen. Signifikante Eisenmengen (bis in den Zehntelprozentbereich) wurden jedoch auch auf Zwischengitterplätzen im Zirkongitter gefunden, wohingegen die Substitution von Zirkon-Gitterionen minimal ist. Es wurde daher gefolgert, dass Eisenanreicherung in sekundärem Zirkon in Form anderer Phasen erfolgt.

Die Bestrahlungsstudien, welche am Ende des Einführungskapitels kurz dargestellt sind, zeigten gegensätzliche Ergebnisse. Bestrahlung mit He resultierte in allen Fällen in einer Zunahme der Strahlenschädigung des Zirkon, erkennbar durch die Bildung von Emissionszentren und der Verbreiterung der Ramanbanden. Ein Ausheilen von bestehender Schädigung wurde nicht beobachtet. Elektronenbestrahlung mit moderaten Energien (20 kV) resultiert dagegen in einem partiellen Ausheilen von Strahlenschäden in vorgeschädigtem Zirkon. Strukturelle Untersuchungen (wie z.B. Mikro-Spektroskopie) sollten daher grundsätzlich vor der Elektronenstrahlmikrosondenanalyse durchgeführt werden, um verfälschte Ergebnisse zu vermeiden.

Dieses Doktoratsprojekt und insbesondere die sieben oben beschriebenen Studien führten zu neuen, wichtigen Ergebnissen, die zu unserem Kenntnisstand über natürlichen Zirkon und seine synthetischen Analoga beitragen. Diese Ergebnisse wurden in vier publizierten Arbeiten und einem eingereichten Manuskript dokumentiert, eine weitere Veröffentlichung ist derzeit in Vorbereitung. Die Ergebnisse werden sich besonders bei der Interpretation spektroskopischer und chemischer Analysen von Zirkon sowie zur Vermeidung analytischer Artefakte als nützlich erweisen. Mögliche zukünftige Forschungsrichtungen und Anwendungen werden diskutiert.

Table of contents

Appendix 1 Nasdala, L., Miletich, R., Ruschel, K. & Váczi, T. (2008): Raman study of radiation-damaged zircon under hydrostatic compression.
Physics and Chemistry of Minerals, **35/10:** 597–602.

Appendix 2 Nasdala, L., Kronz, A., Wirth, R., Váczi, T., Pérez-Soba, C., Willner, A. & Kennedy, A.K. (2009): The phenomenon of deficient electron microprobe totals in radiation-damaged and altered zircon.
Geochimica et Cosmochimica Acta, **73/6:** 1637–1650.

Appendix 3 Nasdala, L., Hanchar, J.M., Rhede, D., Kennedy, A.K. & Váczi, T. (2009): Retention of uranium in complexly altered zircon: An example from Bancroft, Ontario.
Chemical Geology, DOI: 10.1016/j.chemgeo.2009.10.004.

Appendix 4 Váczi, T., Nasdala, L., Wirth, R., Mehofer, M., Libowitzky, E. & Häger, T. (2009): On the breakdown of zircon upon “dry” thermal annealing.
Mineralogy and Petrology, **97/1–2:** 129–138.

Appendix 5 Váczi, T., Nasdala, L., Hanchar, J.M., Kronz, A., Götze, J., Dyar, M.D. & Wiedenbeck, M. (2009): Iron incorporation in zircon.
Submitted to *European Journal of Mineralogy.*

1. Introduction

Zircon, the most common zirconium-bearing mineral on the Earth, is the “leitmotif” in the topics covered by the PhD project presented here. In spite of being an accessory mineral, zircon can be found in the most varied settings: in meteorites and lunar rocks, in ultrabasic to acidic igneous rocks, in weakly metamorphic rocks to ultrahigh-pressure ones, but also in sedimentary rocks, sediments and soils.

Zircon, however, is not simply one of the many accessory minerals. Natural actinides are readily built in the zircon structure upon growth from melts and during metamorphism. The actinides then gradually undergo radioactive decay and eventually convert to lead isotopes. Although the energy released during decay introduces structural damage, zircon seems to survive but the harshest conditions, while being able to preserve chemical (*e.g.* U/Th and Pb content) and structural properties (even the accumulated self-irradiation damage). Zircon is therefore one of the most important materials used for U–Pb geochronology, able to record the memory of effectively the entire history of the Earth. It serves also a model material for studying long-term, low-intensity displacive irradiation, a condition not achievable in laboratory work. The insights learnt from radiation damage in zircon are essential in modern, high-tech applications such as the design of waste forms for the long-term geological of high-activity radioactive waste, for instance plutonium from dismantled nuclear warheads and commercial nuclear power plants.

Zircon is also a raw material of ever-increasing significance. It is found in industrial quantities mostly in heavy mineral sands of coastal placer deposits. Zircon sand is used as the raw material for a large number of specialty applications. Zircon is not wetted by molten metals and glass, therefore moulds lined with zircon and zircon refractory bricks are often used in foundry and the glass industry. Zircon has been applied as armour plating on military aircraft and in the heat shield of spacecrafts as well. The ceramic industry uses either purified/synthetic zircon as an opacifier additive in glazes to increase their brilliance, or, doped with different elements, as popular pigments (*e.g.* Fe: pink, V: blue, Pr: yellow). Zircon doped with rare-earth elements is also used as a luminescent phosphor. The chemical stability of zircon makes it suitable for environmental barrier coatings in the chemical industry and in desalination plants. Radiation-amorphised zircon has also been described as an optical waveguide material, making use of its high refractive index. Sintering zircon with alumina produces a mullite–zirconia composite ceramic material, with excellent chemical and mechanical properties. To end this list, zircon as the main source of the metal zirconium must also be mentioned.

As seen from this extensive, though still incomplete, set of applications, zircon or its synthetic analogue is an important and interesting material. Accordingly, the scientific and technological interest in zircon is truly remarkable. As of late November 2009, a search in *Science Citation Index Expanded*™ with the keyword *zircon*, limited to the last 20 years, returns 10 282 hits. In contrast, a similar search for *quartz* gives only about 4.5 times as many, 47 628 hits, in spite of being one of the most common terrestrial minerals. Note that over 8500 of the above search hits on zircon and about 19 000 on quartz are relevant to planetary, earth and environmental sciences. This extreme “popularity” of zircon has led to the coining of the term *zirconology*, which is a pseudo-discipline dealing with every aspect of the material zirconium silicate.

The research topics outlined in this dissertation focus on several features of the mineral zircon and its synthetic analogues. The studies were motivated primarily by geological aspects, but certain examples and results bear relevance to technical applications as well. The first chapter of the dissertation includes an Introduction to zircon research. Zircon as a material, radiation damage and Raman spectroscopy will be key issues in the discussions, therefore a concise review of these three topics will be given below in sections 1.1 to 1.3. The introduction is followed by an enumeration of analytical methods used in the experimental work (section 2), complemented by examples of what the tools may be used for. Section 3 briefly reports the results, conclusions and implications of seven studies. Five of these have been documented in four published papers and one submitted manuscript. They deal with the spectroscopic and/or textural properties of zircon under high pressure and high temperature (section 3.1); the peculiar properties of altered zircon (section 3.2); and the incorporation of iron, a non-formula element, in zircon (section 3.3). The last two studies, presented and discussed in more detail in section 3.4, discuss the effects of alpha particle irradiation and moderate-energy electron beam analysis on damage in zircon. These two topics were published as conference contributions; the alpha-particle irradiation study is being prepared for publication in a journal. Finally, the five complete journal contributions are reprinted in Appendices 1 to 5, in chronological order of their appearance.

Two of these completed studies (Appendices 4 and 5) and the electron-irradiation experiment (section 3.4.2), were lead (*i.e.*, planned, coordinated and conducted) by the author of this dissertation. In the three other completed works (Appendices 1 to 3) and the He-irradiation study (section 3.4.1), the author was involved to a major degree as contributor, in charge of vibrational (Raman and infrared absorption) spectroscopy and scanning electron microscopy and involved in data reduction and interpretation.

1.1. Mineralogical properties of zircon

Zircon is an accessory orthosilicate mineral. Its nominal chemical formula is $ZrSiO_4$ ($Z = 4$), space group $I4_1/amd$. The zircon structure (for a review see Finch & Hanchar, 2003) can be described as chains of alternating, edge-shared SiO_4 and ZrO_8 polyhedra running parallel to the *c* axis; these chains are connected by the screw axis (Fig. 1). The structure is relatively open; it has “channels” of nominally empty sixfold sites, running parallel to the [001] direction, which can host a number of non-formula elements (Robinson *et al.*, 1971). The ZrO_8 triangular dodecahedra are connected through edges in a zigzag pattern along the ⟨100⟩ directions. This arrangement is responsible for the most common prismatic habit of zircon and the indistinct cleavage along {110}.

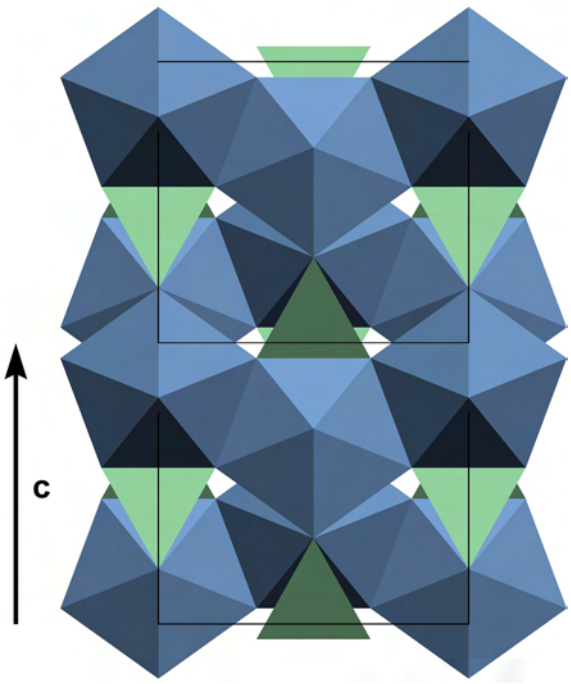

Fig. 1. The idealised structure of zircon in a polyhedral representation, showing two unit cells. Green: SiO_4 tetrahedra; blue: ZrO_8 dodecahedra.

Natural zircon always contains non-formula elements. As a general rule of thumb, large cations (U, Th, Y, lanthanides, Hf) substitute Zr in the eightfold dodecahedral site, whereas smaller cations may be hosted in the sixfold position.

Silicon may be replaced by four H^+ ions ("hydrozircon" substitution; *e.g.* Frondel, 1953; Mumpton & Roy, 1961) or P (*e.g.* Hanchar *et al.*, 2001). Among the elements compatible with the *Zr* site, most notable is Hf, which is present in virtually all natural zircon samples; hafnon ($HfSiO_4$) is the only mineral with which zircon forms a complete solid solution (Finch & Hanchar, 2003). Rare-earth elements (REEs) and Y are also not uncommon in zircon; REEs give rise to luminescence phenomena (*e.g.*, cathodo- and photoluminescence). Radioactive actinides (U and Th) are also often incorporated into natural zircon, introducing self-irradiation damage through time as they undergo radioactive decay (see section 1.2). A very important property of crystalline zircon is that it very strongly discriminates against Pb^{2+} upon crystal growth, therefore is it exceptionally well suited for U/Th–Pb dating, especially considering the exceptionally low volume diffusivity of Pb in zircon (see *e.g.* Cherniak & Watson, 2001).

Both natural igneous and synthetic zircon frequently shows sector and/or oscillatory growth zoning. Sector zoning is caused by different non-formula element concentrations in different growth sectors, while oscillatory zoning in zircon is a result of the succession of growth layers with alternating high and low impurity levels. Zoning is therefore primarily chemical in origin; however, it is often apparent on cross-polarised optical microscopic, back-scattered electron (BSE) and cathodoluminescence (CL) images. It has been shown that the main factor controlling birefringence and BSE (and partly CL) intensity in single crystals of zircon is not trace element content directly but rather the level of radiation damage (Chakoumakos *et al.*, 1987; Nasdala *et al.*, 2002; Nasdala *et al.*, 2006a).

There is a sharp physical, chemical and microtextural distinction between primary zircon crystallised from melts, solutions or during metamorphic events, and secondary zircon grown as a result of fluid-driven replacement reactions (*e.g.* Pointer *et al.*, 1988; Smith *et al.*, 1991; Corfu *et al.*, 2003; Nasdala *et al.*, 2009c; see also Geisler *et al.*, 2001b). Primary zircon grows as a dense solid; incorporated non-formula elements mostly include those replacing Zr. However, the decay of radioactive actinides introduces (through atomic displacements) disorder and amorphisation in the structure, reducing resistance against dissolution (*e.g.* Lumpkin, 2001; Tromans, 2006) so much that strongly damaged zircon is attacked even by pure water (*e.g.*, Geisler *et al.*, 2003a). Zircon alteration is characterised by the growth of porous, secondary zircon, which often contains many mineral inclusions (*e.g.* Pérez-Soba *et al.*, 2007). In analogy with primary zircon, secondary zircon always grows crystalline, subsequent self-irradiation may destroy its structure (Nasdala *et al.*, 2009c). Compatible elements may be enriched or depleted depending on the fluid driving the alteration (*e.g.* Nasdala *et al.*, 2009b). Most notable is, however, that the U/Th–Pb isotope systems may be disturbed by depleting ("leaching"), but also by enriching, actinide and/or Pb concentrations. In age determination results these effects show up as normal or reverse discordance, or may entirely prevent data interpretation. Note that structural damage strongly enhances the susceptibility of zircon to Pb loss, but metamictisation in itself will not generate discordance. At high temperatures (above the closure temperature of the U/Th–Pb system, *i.e.* 800–900 °C) Pb is lost by diffusion. Even for this, percolating amorphous regions (Salje *et al.*, 1999) are needed since Pb diffusion is only practically feasible along crystalline–amorphous grain boundaries (Cherniak & Watson, 2003). Another possibility for isotopic disturbance is fluid-driven alteration, during which extensive element mobilisation takes place (often referred to as "dissolution–reprecipitation"; Putnis, 2002).

Lead is not the only element whose concentration may change appreciably during an alteration event. Elements such as Ca, Al, Fe, P *etc.*, which are normally highly incompatible with and practically missing from primary zircon, may occasionally be measured up to wt% concentrations; their presence may be taken as an indicator for secondary altered zircon. (For a detailed discussion of the properties of altered zircon, the reader is referred to Nasdala *et al.*, 2009c, in Appendix 2, whereas Váczi *et al.*, submitted, in Appendix 5 focuses on the case of Fe incorporation in zircon.)

1.2. Radiation damage

When discussing natural zircon one cannot neglect the phenomenon of radiation damage. Radiation damage is the partial to total destruction of a crystalline structure by high-energy radiation. One may speak about external irradiation, where the source of the energetic particles is not the damaged solid itself. Natural examples are radiohaloes, which are spheres of damage caused by alpha particles (*e.g.* Nasdala *et al.*, 2005; Nasdala *et al.*, 2006b; Krickl *et al.*, 2008), while artificial irradiation may be done using different sources. To cite examples from zircon research, irradiation studies using heavy ions (*e.g.* Weber *et al.*, 1994; Meldrum *et al.*, 1998; Wang & Ewing, 1992; Lian *et al.*, 2003), light ions (Nasdala *et al.*, 2009a), electrons (*e.g.* Meldrum *et al.*, 1997; Jiang & Spence, 2009) or dual ion and/or electron beams (*e.g.* Wang & Ewing, 1992; Lian *et al.*, 2009) are known. The damage caused by natural alpha-particle irradiation can be approximated with artificial irradiation with light ions, alpha recoil (see below) creates damage similar to heavy ions, while beta (β^-) decay (not treated in detail here) is a kind of high-energy electron radiation.

In contrast to external radiation sources, self-irradiation has a distributed source within the material in the form of radioactive atoms (ions) chemically bound in the structure; self-irradiation is therefore not directional. Self-irradiation damage may be caused by alpha and beta decay and spontaneous fission events. Beta decay is rather ineffective in creating permanent damage (atomic displacements). A single fission event creates considerable damage but is significantly less probable compared to alpha decay (decay constants $8.51 \cdot 10^{-17}$/year *vs.* $1.55 \cdot 10^{-10}$/year, respectively, for ^{238}U; this translates to one fission per *ca.* 1.8 million alpha decay chains). Furthermore, a single actinide ion in natural zircon undergoes six (^{232}Th), seven (^{235}U) or eight (^{238}U) alpha decays until a stable isotope is formed (^{206}Pb, ^{207}Pb and ^{208}Pb, respectively). For these reasons most of the radiation damage in zircon (or other actinide-containing solids) is caused by alpha decay.

During an alpha decay event an unstable, heavy nucleus spontaneously transforms into another nucleus ("daughter" isotope, with atomic number, *Z*, two less than the "parent") and emits a ^{4}He nucleus, *i.e.* an alpha particle. Due to the conservation of momentum, the alpha particle acquires an enormous kinetic energy (4.0–8.8 MeV) and is able to travel a few tens of micrometres through zircon: the stopping range of 8.8 MeV alpha particles is up to *ca.* 32 µm in non-porous, crystalline zircon (*e.g.* Nasdala *et al.*, 2009a). Throughout most of its path there is very little interaction with nuclei in the structure; most of the energy is lost through non-displacive interactions such as ionisation losses and electronic or vibrational excitations. An alpha particle is able to create up to a few hundred vacancy–interstitial pairs (so-called Frenkel defects) by collision with atoms in zircon, most of which is concentrated at the end of the trajectories (*e.g.* Weber *et al.*, 1998).

The heavy alpha recoil nucleus of the daughter element has a lower kinetic energy (70–160 keV) but a large mass, and a significant part of its energy is dissipated through collisions with structure atoms. The stopping range of such heavy nuclei is a few times 10 nm, but in this short distance a ballistic collision cascade is formed with a few thousand displaced atoms (may exceed 6000 defects at 300 K; Devanathan *et al.*, 2006). Most of the damage due to a chain of alpha events is thus created in a small volume. As a consequence, even very fine-scale compositional zoning in zircon is commonly preserved even when higher-U zones have become metamict (Chakoumakos *et al.*, 1987; Nasdala *et al.*, 2009b), allowing *in-situ* microbeam analyses of elemental and isotopic compositions of growth zones. The progressing stages of damage accumulation may be described as (i) isolated amorphous damage clusters scattered in a crystalline matrix with a few defects; (ii) amorphous clusters overlap (percolate) due to their increasing number, while the defect density and strain in crystalline volume increases; (iii) defect-laden crystalline "islands" are no longer interconnected in an amorphous matrix; (iv) finally the entire material becomes amorphous (Murakami *et al.*, 1991; Salje *et al.*, 1999). In the crystalline remnants of stages (ii) and (iii), isolated Frenkel defects accumulate with progressing metamictisation, and

strain develops due to both the point defects and the heterogeneous swelling of the bulk material (see below).

Radiation damage that happens on the microscale introduces changes in the bulk physical and chemical properties of zircon as well (see Ewing *et al.*, 2003, for a review). The most important effects include, for example, an expansion of the unit cell and bulk swelling (and hence density decrease; Holland & Gottfried, 1955). Damage also decreases birefringence (Fig. 2; see *e.g.* Holland & Gottfried, 1955; Nasdala *et al.*, 2009b). An interesting observation of Pirkle (1992) is that in heavy mineral placer deposits radiation-damaged zircon tends to be subordinate because metamictisation makes it more brittle and, thus, less resistant to mechanical weathering (Chakoumakos *et al.*, 1987, Chakoumakos *et al.*, 1991). A phenomenon of major importance is that diffusion is enhanced when amorphous domains start to overlap (first percolation point; Salje *et al.*, 1999) due to the opening of diffusion pathways along interfaces between crystalline and amorphous domains.

One major argument against the use of zircon as a radioactive waste form comes from radiation-induced swelling (see above). Natural (Corfu *et al.*, 2003) and doped synthetic zircon is most often chemically zoned (*e.g.* Hanchar *et al.*, 2001; see also Váczi *et al.*, submitted), and when radioactive elements are incorporated into zircon heterogeneously, heterogeneous expansion causes cracking in non-expanded zones (*e.g.* Chakoumakos *et al.*, 1987) and gives fluids access to internal, damaged zones while increasing the surface area for dissolution (see *e.g.* Lee & Tromp, 1995). Dissolution, in turn, may mobilise major and trace elements, causing an unwanted deterioration of radionuclide retention capabilities.

Radiation damage in zircon is not stable under all conditions. Heat treatment (thermal annealing) experiments revealed that short- and long-range order can be restored at elevated temperatures. In fact, whether or not a crystalline solid becomes metamict depends largely on the ratio of damage accumulation and temperature-dependent annealing rates specific to the material itself. For example, the temperature above which monazite (zircon-structured rare-earth phosphate) can no longer be amorphised, because the annealing rate is faster than damage accumulation, is *ca.* 600 °C lower than for zircon (Meldrum *et al.*, 1998). It follows that the observed self-irradiation damage level in natural zircon samples, for example as determined by Raman spectroscopy, will be a function of actinide concentration and age (causing metamictisation) counteracted by potential thermal annealing (causing recovery).

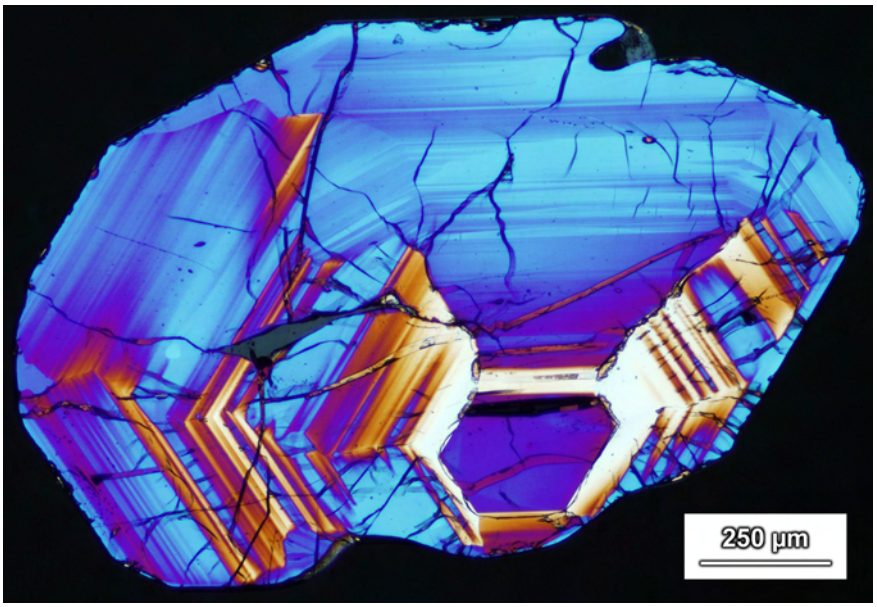

Fig. 2. A polarised-light microscope image (crossed polarisers) of a zircon grain from Plešovice, Czech Republic, illustrating the importance of micro-analysis. Areas with whitish interference colours indicate zones where birefringence is lowered by strong self-irradiation damage. Swelling-induced cracks are filled with another material. Sample courtesy J. Košler (University of Bergen, Norway); for details see Sláma *et al.* (2008).

The recovery of radiation damage in partially metamict zircon is still a subject of controversy. One opinion states that that the point defects (Frenkel pairs) in the remnant crystalline volume are annihilated first (Colombo & Chrosch, 1998a; Geisler *et al.*, 2001a), followed by the epitaxial recrystallisation of amorphous domains on existing crystalline zircon (Capitani *et al.*, 2000). The other view says that the recombination of Frenkel pairs in a crystalline lattice needs more energy (*e.g.* occurs at higher temperatures) than the reorganisation of amorphous domains on crystalline templates (see *e.g.* Presby & Brown, 1974).

In the case of fully amorphised (metamict) zircon, *i.e.* with the lack of any crystalline template, amorphous zircon first dissociates into a mixture of crystalline ZrO_2 and amorphous SiO_2 (*e.g.* Colombo & Chrosch, 1998b; Capitani *et al.*, 2000; Nasdala *et al.*, 2002; see also Kim & McIntyre, 2002; Monaghan *et al.*, 2005). During further annealing, and especially at higher temperatures, the ZrO_2–SiO_2 mixture fuses and forms crystalline $ZrSiO_4$. Note that after zircon has passed the second percolation point (where connections within the remnant crystalline fraction are broken and crystalline islands become crystallographically misaligned), *i.e.* in severely and fully damaged zircon, annealing produces polycrystalline grains; whereas below the second percolation point single crystals are restored.

The phenomenon of radiation damage is relevant to some extent in all studies in this dissertation, with the sole exception of the iron doping study (Váczi *et al.*, submitted; see Appendix 5). The behaviour of Raman parameters (see below) of damaged zircon at high pressures was discussed in Nasdala *et al.* (2008; see Appendix 1), the influence of damage on the high-temperature stability was evaluated in Váczi *et al.* (2009; see Appendix 4), the fluid-driven alteration (Nasdala *et al.*, 2009b; 2009c; see Appendices 2 and 3) is inherently linked to earlier metamictisation, and finally the changes in the damage state due to artificial irradiation with energetic particles (He ions and electrons) on zircon was also investigated (Nasdala *et al.*, 2009a; Váczi & Nasdala, 2008; see section 3.4).

1.3. Raman spectroscopy

The Raman effect is an inelastic scattering process that happens when an electromagnetic radiation interacts with a molecule or solid. The incoming photon excites the system to a virtual state (an excited energy level of the system that is not a discreet state) while the incident photon is annihilated. The excited state relaxes through the creation of a new photon. In the absence of any energy transfer, *i.e.*, if the energy of the incident photon is the same as the energy of the scattered one, we talk about Rayleigh (or elastic) scattering. As a rough estimate, about one in a million of incident photons, however, causes a perturbation in the molecule or solid and opens the possibility of a vibrational transition, while the scattered photon has an energy different from the incident one (Raman scattering). The energy of the incident photon is equal to the sum of the energy of the Raman-scattered photon plus the energy transferred to or from the vibrational transition. The scattered light thus shows a red shift (*i.e.*, a shift towards lower energies) if part of the incident energy is used to raise a vibration to the excited state; this is called the Stokes shift. If an excited vibration relaxes to the ground state due to a Raman scattering event, the scattered light shows a blue shift (anti-Stokes Raman scattering). Under ambient conditions, the Stokes side of the Raman spectrum is much more intensive and therefore in classical Raman spectroscopy only that is measured and shown.

Raman scattering provides chemical information about molecules and solids. Chemical bonds are not fixed “sticks”, in contrast to figures in static visualisations. In the classical harmonic model of molecular vibrations, bonds act as forces between atoms (also ions; in the followings “atoms” will be used to cover both for brevity), whereas atoms are never at rest: bonded atoms oscillate around an equilibrium position which is where restoring forces cancel each other. In complex, polyatomic systems the vibrations may seem very complicated but in all cases the vibrational properties of a system can be described as the super-

position of elementary vibrations (the so-called fundamental modes) such as stretching, bending and rotation of atom pairs or groups.

Vibrations carry energy; a quantum (energy unit) of vibrational energy is called a phonon. Raman spectra are thus phonon spectra, consisting of bands that correspond to excitations (Stokes) or relaxations (anti-Stokes) of individual vibrations of molecules or solids, all recorded on an energy shift scale relative to the elastic scattering. Note that not all vibrations of a molecule or a solid show up as a band in Raman spectra. Raman scattering of light, *i.e.* an inelastic interaction between the excitation source (*e.g.* a laser light) and vibrations, only occurs if the polarisability of the bond changes during the oscillation, which is determined by symmetry constraints (the so-called selection rules). The energies of the phonons depend on bond strengths and the masses of the bonded atoms, for which reason the Raman spectrum, *i.e.* the sum of all Raman-active transitions, of every substance is unique and can be thought of as a "fingerprint" and used for identification.

Most common Raman spectrometer configurations used today in Earth science research employ lasers as excitation source, microscopes for observation, sample illumination and light collecting, and dispersive gratings for spectral decomposition. The laser beam is guided by mirrors or glass fibres through a beam expander to the laser line rejection filter. This filter is either a low-pass edge filter (for Stokes Raman) or a band-stop notch filter (which allows recording Stokes and anti-Stokes Raman scattering as well). Laser rejection filters are reflective for the laser energy but transmissive for other energies starting typically from a few ten wavenumbers away from the laser line. The filter is fixed in a way that it reflects the laser spot into a microscope, parallel to the optical axis. The laser spot is focused onto the sample, the interaction takes place in the focal spot and the scattered light is collected by the microscope objective (quasi-backscattering geometry). It is transmitted again through the edge or notch filter, most of the laser energy is rejected and the inelastically scattered component is spectrally decomposed in the spectrometer and projected into the detector. In most instruments charge-coupled device (CCD) detectors are used that are able to record a spectral window (*i.e.*, a spectrum) during a single exposure.

A confocal optical arrangement may be used to improve the spatial resolution of the instrument. A pair of conjugate apertures (pinholes) installed in the light path at appropriate positions have the effect of cutting off light collected beyond a distance from the focal plane (Tabaksblat *et al.*, 1992). The smaller the pinholes are the better is the depth discrimination, and therefore the vertical and, to some extent, the lateral resolution of the system, though at the expense of light collection efficiency. Such instruments are often called "Raman microprobes", referring to the very small excitation volume (down to 5 μm^3; Markwort *et al.*, 1995) possible to achieve. A similar effect on resolution may be reached by focusing Raman light on a slit before the spectrometer grating and software masking the image height on the detector (Williams *et al.*, 1994). Such "pseudo-confocal" instruments offer good light throughput and an improved spatial resolution (but lag behind truly confocal systems) over non-confocal setups.

Raman spectroscopy has proven very useful in the study of zircon. Pure, crystalline zircon is a fairly strong Raman scatterer and is very stable under the laser beam. The short-range order (atomic configuration, coordination, symmetry) is disturbed by strain, caused for example by the substitution of Zr by elements with a different ionic radius, or by defects (vacancies, interstitials) and strain due to self-irradiation damage; these changes are observable in the Raman spectrum as well. The most sensitive indicator of a decrease of the short-range order in zircon is the asymmetric stretching vibration of the SiO_4 group, denoted as $v_3(SiO_4)$ (B_{1g} mode; Dawson *et al.*, 1971). It has been found, for instance, that the extensive replacement of Zr by Hf (Hoskin & Rodgers, 1996) or U (Geisler *et al.*, 2005) influences the $v_3(SiO_4)$ band parameters at substitution levels in the 10 at% range. However, this influence at the concentration of non-formula elements commonly found in natural zircon is negligible. Therefore, Raman analysis is ideal for the studying of radiation-induced damage in zircon, without having to consider notable chemical effects.

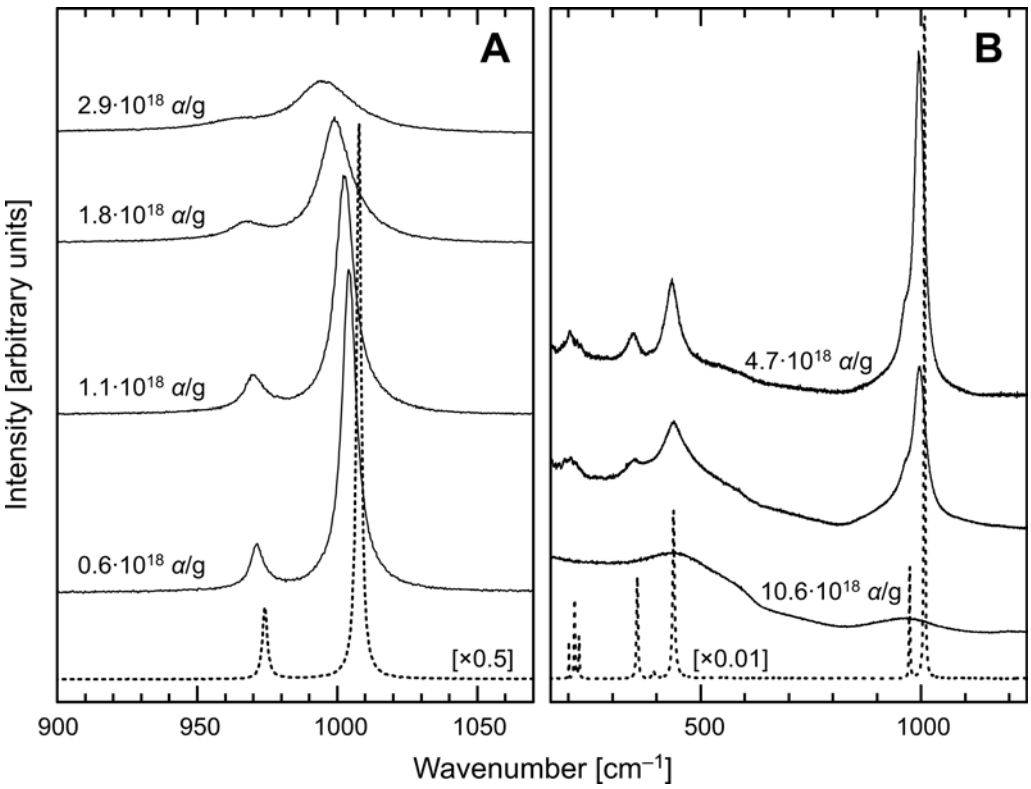

Fig. 3. Plots showing the evolution of the zircon Raman spectra (band shift, broadening) with increasing radiation damage. **A** Spectra of four samples from zero (dotted line) to moderate radiation damage in the SiO_4 stretching range. **B** Spectra showing that strong radiation damage gradually obscures the Raman scattering of zircon. The completely metamict sample ($10.6 \cdot 10^{18}$ α events) shows only a weak scattering coming from amorphous $ZrSiO_4$. The zero-damage spectrum (dotted line) is shown for comparison. (Modified after Nasdala *et al.*, 2003.)

The $v_3(SiO_4)$ zircon Raman band shifts to lower relative wavenumbers and broadens with increasing radiation damage (Fig. 3; see Nasdala *et al.*, 1995; Zhang *et al.*, 2000). The full with at half maximum (FWHM) of this band has been shown to be directly correlated with radiation damage doses (Nasdala *et al.*, 2001), which can be used as a guide to estimate, with high spatial resolution, the degree of damage in zircon. In the absence of significant structural damage, Raman analysis can also be used to study disorder due to impurity incorporation in zircon. These properties have been used in all research topics in this dissertation, including a high-pressure study (Nasdala *et al.*, 2008; see Appendix 1), investigations of zircon alteration (Nasdala *et al.*, 2009b, 2009c; see Appendices 2 and 3) and the iron incorporation in zircon (Váczi *et al.*, submitted; see Appendix 5), and the measurement of damage caused by external He ion (Nasdala *et al.*, 2009a) and electron irradiations (Váczi & Nasdala, 2008).

2. Methods

In this section a summary with very brief descriptions are given of the numerous analytical techniques used in the studies presented, including what problems they may be applied to. Instrumental parameters are not listed, they may be found in the Appendices. The techniques are listed here in groups approximately according to imaging, spectroscopic techniques, element and isotope analysis, and supplementary techniques (see Table 1 for an overview).

Most of the analyses (Raman point analysis, infrared absorption spectroscopy, scanning electron imaging, photoluminescence spectroscopy *etc.*) were done at the University of Vienna. For special equipment and expertise, a number of short research visits were made to other institutions. These included the Helmholtz Centre Potsdam (GFZ German Research Centre for Geosciences), Germany, in 2006 for focused ion beam sample preparation and transmission electron microscopy; the Forschungszentrum Dresden-Rossendorf, Germany in 2007 for He ion implantation at a tandem accelerator facility; the Curtin University of Technology, Perth, Australia, in 2007 for U–Pb isotope analysis; the University of Innsbruck, Austria, in 2008 for Raman mapping; and finally the Johannes Gutenberg University Mainz, Germany, in 2009 for electron irradiation and Raman mapping.

2.1. Imaging

Optical light microscopy is used perhaps for all samples, from preparation and observation with a stereomicroscope to the estimation of birefringence with a polarised light petrographic microscope. The same microscope with ultraviolet illumination may be used to take real-colour photoluminescence (PL) images. A scanning electron microscope (SEM) can be used to record several signals. The most common imaging technique is the secondary electron (SE) image, used almost exclusively to record surface topography. Backscattered electron (BSE) images can be obtained in several ways; best known is the average atomic number ($\overline{Z}$) imaging. Note, however, that compositional contrast is not the only phenomenon recorded by a BSE detector. Orientation contrast may be observed between two, differently oriented crystals of the same material; while electron channelling reduced for instance by radiation damage causes a contrast within single crystals, as is the case with most zoned zircons (for more background see Nasdala *et al.*, 2006a, and references therein). Flat, polished samples were mostly carbon-coated before SEM imaging. In the special case where unprepared grains were imaged, the variable pressure SEM was used to spare the carbon coat, thus avoiding a strong luminescence background in later Raman measurements. Transmission electron microscopy (TEM) offers a variety of imaging methods, including bright field (BF) and dark field (DF) images, selected area electron diffraction patterns (SAED; where the image is actually a Fourier transform of the BF image). High-resolution TEM (HRTEM) provides images down to nanometre resolution. In the scanning TEM (STEM) mode a very tightly focused electron beam is scanned over the surface and the high-angle annular dark field (HAADF) detector is used to record high-resolution images with compositional contrast. Cathodoluminescence (CL) imaging may be done in a hot-cathode CL system, where a defocused electron beam excites CL and the emission is observed optically in real colours through an optical microscope (OM-CL). In contrast, a CL system in a SEM (SEM-CL) uses

an optical light guide to record CL intensity point by point as the focused electron beam is rastered over the sample surface; the resulting image is monochrome. Cathodoluminescence images are very effective in revealing internal textures of complex, zoned zircon.

Raman maps ("hyperspectral images") may be generated from an *x*–*y* (or in transparent samples *x*–*z*, *y*–*z*) dataset of Raman spectra (see below), by recording a single spectrum at each raster point and reducing the data to show a desired spectral parameter at each point. The so-called "chemical images" generated from the datasets show the spatial distribution of a certain feature, for instance the level of radiation damage or strain in zircon. An electron probe microanalyser (EPMA, also electron microprobe; see below) may be used to generate maps of element distributions on polished sample surfaces, for instance aiding the correlation of the depletion or enrichment of different elements with textures seen with other methods.

2.2. Spectroscopic techniques

Raman scattering and infrared (IR) absorption probe transitions between vibrational energy levels, and therefore characteristic for any given material (molecule or solid). The two methods can be used as fingerprinting for material identification but specific vibrations may carry detailed information on certain material properties. The IR technique is very sensitive for instance to absorption due to H–O bonds and may be used to analyse hydrogen incorporation (hydrous species) in solids. Raman spectroscopy offers a way to quantify for instance structural properties such as the short-range order in zircon as a function of irradiation dose. Photoluminescence (PL) spectroscopy uses luminescence emission excited by a laser source. For instance the pressure shift of the ruby luminescence (*R* lines) may be recorded using a Raman instrument. Note that PL bands may easily show up in Raman spectra and *vice versa*; discrimination between the two signals may require the changing of the excitation wavelength. A spectrometer coupled to a CL system is able to record CL spectra for the identification of CL emission centres. Mössbauer spectroscopy is a tool most often used for the identification of the valence and the coordination number of Mössbauer-active isotopes in solids. In geological samples, Mössbauer spectroscopy is most often used to determine the oxidation state and coordination of Fe.

2.3. Element and isotope analysis

Electron probe microanalysis is a widely used method to measure major to trace element concentrations *in situ*. It is an electron beam method, where the characteristic X-rays generated by moderate-energy (15–20 keV) electrons are detected. High precision may be reached by wavelength-dispersive X-ray (WDX) detectors, down to µg/g concentration levels, depending on the element and measurement conditions. For lower detection limits and especially for analysing low atomic number elements (*e.g.* Li) and certain isotopes, the secondary-ion mass spectrometer (SIMS) may be used. This instrument uses a primary ion beam to sputter a small amount of material (from a *ca.* 10 µm diameter pit) from the sample surface, which forms a secondary ion beam that is dispersed and analysed according to the mass to charge ratio of the ions. The sensitive high mass resolution ion microprobe (SHRIMP) is basically a SIMS instrument with an oversized secondary ion beam path and increased mass discrimination, primarily used for isotope geochronology (see Appendices 2 and 3). An analytical TEM (ATEM) is a STEM equipped with an energy-dispersive X-ray (EDX) detector, capable of element analysis with the resolution of a few nanometres. Electron energy loss spectroscopy (EELS) is an analytical technique in the TEM, where the energy of forward scattered electrons passed through the sample is measured; the spectra may be used for instance to identify the incorporation of hydrous species at a much smaller scale than IR (a few nm *vs.* a few times 10 µm, respectively).

2.4. Supplementary techniques

The instruments listed here are not analytical tools but are important in sample preparation or performing certain experiments. The focused ion beam (FIB) technique uses a Ga ion beam to mill into sample surfaces; it is possible, among other things, to cut an electron transparent (*ca.* 100 nm thick) foil for TEM investigations. A diamond anvil cell (DAC) is a mechanical device that presses together two clear, transparent diamond "anvils" to reach very high pressures through a pressure transmitting medium. The diamonds act as windows, through which a number of analytical methods (including Raman and PL spectroscopy) are possible. And finally, a tandem accelerator can generate high kinetic energy ions, such as $^{4}He^{2+}$ (identical to an alpha particle). The accelerated ions are implanted in the sample and resulting changes in material properties may be investigated using other methods. Implantation depths (stopping ranges) and damage (point defects) created by the implanted particles were calculated using the Monte Carlo (MC) simulation program package SRIM/TRIM.

Table 1. Summary of applied analytical tools to characterise samples, and in which study the given techniques were used. The abbreviations of analytical techniques are explained in the text.

Analytical method	**Study where used** (see key below)
Imaging	
SEM SE	TD
SEM BSE	UR, TD, Fe, EI
TEM BF, DF	LT, TD
TEM SAED	LT, TD
HRTEM	LT, TD
STEM	LT, TD
CL imaging (OM, SEM)	LT, Fe, He
PL imaging	He
element mapping	UR
Raman mapping	Fe, EI
Spectroscopy	
Raman	HP, LT, UR, TD, Fe, He, EI
IR	LT
PL	HP
CL spectroscopy	Fe, EI
Mössbauer	Fe
EELS	LT
Element/isotope analysis	
EPMA	LT, UR, Fe, EI
ATEM	TD
SIMS	Fe
SHRIMP	LT, UR
Supplementary methods	
FIB	LT, TD
DAC	HP
tandem accelerator	He
MC simulation	He

HP: high-pressure Raman study; Nasdala *et al.* (2008), Appendix 1
LT: low analytical totals; Nasdala *et al.* (2009c), Appendix 2
UR: uranium retention in altered zircon; Nasdala *et al.* (2009b), Appendix 3
TD: thermal decomposition; Váczi *et al.* (2009), Appendix 4
Fe: iron-doping of zircon; Váczi *et al.* (submitted, Appendix 5
He: helium irradiation; Nasdala *et al.* (2009a)
EI: electron irradiation; Váczi *et al.* (2008)

3. Main results

In this section the major results of the dissertation are summarised. The outcome of the research activity has been written up in five journal papers, four of which have already been published, while one is submitted for publication. All five papers are reprinted in Appendices 1–5 in full length. Here only a brief overview of these studies on zircon is given, outlining the most important conclusions. Two studies on external irradiation were presented at conferences; therefore slightly extended summaries of them are given in section 3.4. The studies are grouped according to the phenomenon investigated, namely (i) zircon properties at high pressure and high temperature, (ii) fluid driven alteration and resulting characteristic features, (iii) effects of iron doping, and (iv) the influence of external irradiation on zircon.

3.1. Properties of zircon at non-ambient conditions

Zircon is mostly investigated under ambient conditions. However, there are certain geological conditions, applications and experiments where high pressures or temperatures are encountered. There is a need, therefore, to understand zircon behaviour under such conditions as well. The works presented in Appendices 1 and 4 do not investigate simultaneous high-pressure (HP) and high-temperature (HT) conditions; instead, they are focused on two aspects of zircon research: (i) the identification of heat treatment of gemstones with unknown history and zircon inclusions and (ii) the behaviour of zircon during dry annealing using everyday laboratory equipment and conditions.

3.1.1. Raman spectroscopy of zircon under pressure (Appendix 1)

Zircon inclusions in certain minerals formed deep in the Earth's crust (*e.g.*, corundum, spinel, diamond) often experience considerable strain under ambient conditions due to differential decompression upon uplift. The zircon inclusions are affected, however, by self-irradiation damage due to their actinide content, but also by the thermal history of the host (Wang *et al.*, 2006; Wanthanachaisaeng *et al.*, 2006). If the host gemstone is heat-treated for instance to improve its colour, then the inclusions are also annealed, possibly erasing radiation-induced damage and related changes in Raman properties. The main goal of Nasdala *et al.* (2008; reprinted in Appendix 1) is to evaluate how strain influences the spectral parameters of the $\nu_3(SiO_4)$ zircon band used for the determination of self-irradiation damage (after Nasdala *et al.*, 1995), and whether Raman spectra of zircon inclusions may be used to recognise heat treatments of their host gemstones.

Four natural zircon gemstones from Sri Lanka, spanning a range between moderate and heavy damage levels, and a pure, synthetic $ZrSiO_4$ sample were subjected to hydrostatic compression in a diamond anvil cell (DAC) up to *ca.* 10 GPa, to record their Raman spectra. Such conditions are far below the pressure required for the zircon to reidite (zircon structure to scheelite, $CaWO_4$, structure) phase transformation (20 GPa in Knittle & Williams, 1993; 23 GPa in van Westrenen *et al.*, 2004). The results have shown that the peak position of the $\nu_3(SiO_4)$ zircon Raman band follows a similar trend, namely an upshift with increasing pressure, in all investigated samples. At the same time, the broadening of the same Raman

band is only very slightly influenced by pressure. This means that the band broadening follows comfortably well the trend defined by ambient-pressure observations (Nasdala *et al.*, 2001, Nasdala *et al.*, 2004) and may therefore be used to estimate the damage levels in zircon inclusions *in situ* inside gemstones, despite any strain ("fossilised pressure"). This information may then be used to establish whether any heat-treatment has been applied to the host gemstone or not, to improve its colour or other properties.

3.1.2. High-temperature behaviour of zircon (Appendix 4)

Naturally-formed zircon rarely encounters circumstances where the temperature reaches 1400 °C. In experiments and technical applications, however, zircon may be exposed to such and even higher temperatures (*e.g.* furnace linings and moulds in metallurgy and the glass industry, environmental barrier coatings *etc.*). For geologists, zircon at high temperatures comes into question mostly in experiments aimed at or simply involving heat treatment (*e.g.* to study the structural recovery of radiation damage and the related changes in physical and chemical properties, or radioactive dating methods that exploit reactions in zircon at high temperature; for a discussion and references see Appendix 4). The aim of the study in Appendix 4 (Váczi *et al.*, 2009) is to evaluate phases and textures formed as a result of zircon decomposition during annealing at 1400 °C, and to discuss the relevance of reaction conditions (sample container, inclusion host, atmosphere) on the breakdown behaviour.

To explore the influence of sample properties, a set of zircon samples were chosen, ranging from pure, synthetic $ZrSiO_4$ through slightly and moderately damaged gem zircon to heavily altered secondary zircon. The results show that breakdown at 1400 °C occurs in all samples (Fig. 4), despite the fact that thermal decomposition is predicted to occur only at significantly higher temperatures (*e.g.* Butterman & Foster, 1967), in accordance with many empirical observations (*e.g.* references in Kaiser *et al.*, 2008). Different radiation damage levels were found to have little qualitative effect on decomposition. On the contrary, secondary altered zircon (see also Nasdala *et al.*, 2009b; 2009c) undergoes major textural changes. The crucible material was found to have a strong effect on the extent and textures of thermal breakdown: a reaction, inferred to take place between alumina crucibles and volatile silica released from zircon, significantly accelerated decomposition, especially on grain surfaces in contact with or at short distances to the crucible. In contrast, such acceleration of breakdown was not observed in inert platinum crucibles. In this study the effects of the atmosphere (gaseous species or vacuum) on the decomposition reaction were also discussed. An attempt was made to explain the relevance of the above influences to the mechanism and success of two zircon dating methods (Mattinson, 2005; Kober, 1986, 1987).

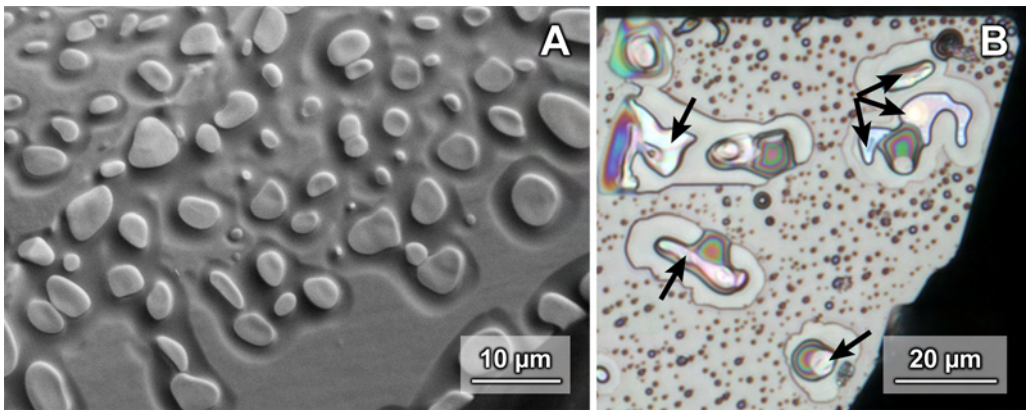

Fig. 4. Breakdown textures on zircon grain surfaces after annealing at 1400 °C.
A SE image of sample M257, showing the morphology of surface corrosion pits and decomposition products. Mid-gray is zircon; lighter gray, rounded grains are ZrO_2. The presence of silica cannot be undoubtedly confirmed from SEM images.
B Optical microscope image, reflected light (sample: pure, synthetic zircon). The white grains marked with arrows are ZrO_2 (baddeleyite). The coloured interference fringes are caused by a thin (< 0.5 µm) layer of unidentified material, assumed to be a remnant of the phase silica. The rest of the silica component is assumed to have evaporated at high temperature.

3.2. Chemical and textural properties of altered zircon

Zircon is generally assumed to be physically and chemically highly stable and resistant. This is indeed true for crystalline to slightly damaged zircon; it is no accident that the oldest known terrestrial material is zircon (4.4 Gyr; Wilde *et al.*, 2001). Self-irradiation due to incorporated actinides, however, damages the structure of zircon, changing the mechanical toughness (*e.g.* Chakoumakos *et al.*, 1991) and solubility (Lumpkin, 2001; Tromans, 2006) significantly. Decreased toughness and heterogeneous swelling open a network of cracks in zoned zircon crystals (Chakoumakos *et al.*, 1987), thus allowing fluids to interact with radiation-damaged internal zones. The reactions driven by fluids leave behind a peculiar signature, observable with a variety of analytical methods. Two studies have been dedicated to alteration features in zircon, one focusing on the chemical and textural changes (Appendix 2, published in Nasdala *et al.*, 2009c) and a second one investigating a special case of alteration where the leaching of radioactive isotopes was surprisingly minimal (Appendix 3, published in Nasdala *et al.*, 2009b).

3.2.1. Deficient electron microprobe totals and related phenomena (Appendix 2)

Altered regions in zircon typically appear very dark in CL and BSE images (Fig. 5), in which they do not obey the "regular" inverse correlation between BSE and CL intensity (*e.g.* Corfu *et al.*, 2003; Nasdala *et al.*, 2006a). These altered areas have often been found to be significantly enriched in non-formula elements as well, but at the same time they show a significant deficiency in analytical totals derived by electron microprobe (*e.g.* Pointer *et al.*, 1988; Smith *et al.*, 1991; Geisler *et al.*, 2003b; see also Nasdala *et al.*, 2009c, and references therein). The article in Appendix 2 (Nasdala *et al.*, 2009c) aimed to find the textural and chemical reasons behind decreased BSE yield, CL emission and EPMA totals (oxide sums).

A selection of samples showing alteration textures were investigated with a variety of analytical tools to explore micro- and nanotextures, elemental (including O) and Pb isotopic compositions, hydrous content and short-range order. Results showed that the deficiency in electron beam analysis sums are not caused by cations missed from routine analysis. Instead, electron microprobe O analysis showed an excess of oxygen, which was assigned to hydrous species. However, adding "water" (with concentrations well in the wt% range) to the oxide sums yielded still deficient analytical totals. Transmission electron microscopy techniques revealed significant nanometre-scale porosity, which was interpreted to reduce both characteristic X-ray and back-scattered electron yield as a result of volume deficiency and interface effects due to porosity.

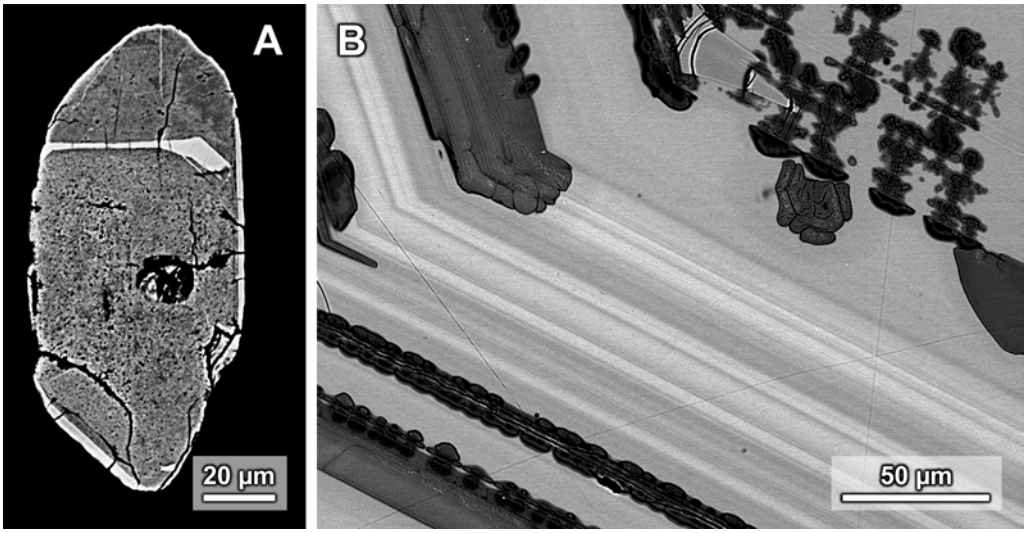

Fig. 5. BSE images showing alteration textures in zircon. **A** Almost entirely altered zircon grain (Ural Mts., Russia; see Willner *et al.*, 2003). Note the strong porosity, which is typical for post-alteration textures. **B** Partial alteration, occurring preferentially along fully damaged primary growth zones (sample: Bancroft, Ontario; see Nasdala *et al.*, 2009b).

3.2.2. Zircon alteration and element mobility: A special case (Appendix 3)

Alteration of zircon by low-temperature hydrothermal fluids remobilises primary zircon in radiation-damaged zones and replaces it with porous zircon with a significantly different chemical character (see above; Nasdala *et al.*, 2009c). Alteration processes are generally assumed to mobilise radioactive and radiogenic isotopes as well, thus severely disturbing the isotope systems used for age determinations. Although one often encounters such processes described as "leaching", it is by no means a rule that only depletion of U, Th or Pb may occur during an alteration event (see, *e.g.*, Utsunomiya *et al.*, 2007, for an example of occasionally extreme enrichment in U and Th) – it depends naturally strongly on the character of the alteration fluid (which mostly remains unknown for natural occurrences). The study in Appendix 3 (Nasdala *et al.*, 2009b) demonstrated that despite major textural differences, the U/Th–Pb isotope systems may yield the same age from radiation-damaged primary areas, altered secondary regions and completely reworked, inclusion-rich parts within the same zircon single crystal.

Zircon samples from Bancroft, Ontario, were investigated in detail using polarised optical microscopy, BSE imaging, electron microprobe chemical analysis and element mapping, and SHRIMP isotope analysis for age determination. Textural analyses have shown single crystals to contain several texture types: a primary, finely zoned region where in fully metamict zones patches of recrystallisation are seen (Fig. 5b) emanating from swelling-induced cracks; large areas completely reworked by alteration, seen as a microscopically porous, polycrystalline area with a very large amount of mineral inclusions *etc.* Chemical mapping and analyses with the electron microprobe revealed a moderate major element mobilisation: Zr and Si are depleted to *ca.* 95% compared to the unaltered areas. Most remarkable is that U is lost only to a similar degree, *i.e.* on average *ca.* 94% of the U is retained in altered patches. In contrast, Pb is lost to a varying degree, causing in cases strong discordance in radiometric ages; however, age data plot very nearly on the same discordia line. The most important implication of these results is that it the mobility of radionuclides may be significantly lower than that predicted by laboratory leaching experiments. Zircon may therefore be a suitable ceramic nuclear waste form, even in its strongly radiation-damaged state. Through a careful engineering of the nuclear waste form(s) and encapsulation materials it might become possible to contain actinides in geological repositories.

3.3. Crystal chemical and spectroscopic characterization of iron-doped zircon (Appendix 5)

The concentration of iron in natural primary zircon is normally very low (Hoskin & Schaltegger, 2003), because di- and trivalent iron is incompatible with the structure. In altered secondary zircon, however, often enriched Fe contents (along with Ca, Al, P *etc.*; see *e.g.* Nasdala *et al.*, 2009b; 2009c) are measured. In natural zircon, however, substitutions, inclusions and textural effects are seen simultaneously, therefore there is no way to establish the influence of a single impurity element. Furthermore, in pink zircon pigments, a widespread application of zircon in the ceramics industry, the pink colouration is caused by Fe doping.

To study the effects of iron on zircon, Fe-doped synthetic zircon crystals were grown in the presence of excess Fe; P was added to aid charge compensation. A special set of samples were doped with iron oxide enriched in the ^{57}Fe isotope to facilitate Mössbauer signal collecting. Mössbauer spectroscopy showed that more than half of Fe is included as a hematite (α-Fe_2O_3) phase; the remaining Fe occupies mostly a sixfold interstitial position, whereas only a minor fraction of Fe replaces Zr. Raman maps revealed an increasing disorder from crystal rims to centres, which was found to correlate well with dopant levels. Chemical data, however, showed a low overall Fe concentration (0.01–0.39 wt%) but also a constant P excess (*ca.* 1:6 Fe to P ratio in calculated atoms per formula units), which

suggested that P incorporation is not the sole charge compensating mechanism. Direct Fe incorporation into the zircon structure was found to be generally low, the majority of Fe being confined to hematite inclusions. Thus, in conclusion, it can be said that wt%-level Fe is not strictly a chemical impurity in secondary zircon, but is the major part is most likely carried by other mineral phases, perhaps of the size below the resolution of routine imaging techniques. Elevated Fe concentrations therefore may be taken as a reliable indicator of secondary alteration.

3.4. Raman spectroscopic studies of external irradiation of zircon

Raman spectroscopy is especially well suited to the study radiation effects with a high spatial resolution. Two studies will be introduced here in which an external source of particles was used to irradiate zircon, and Raman spectroscopy, along with ther techniques, was applied to evaluate the resulting changes in the short-range order in the irradiated volume. In the first study (Nasdala *et al.*, 2009a) the effect of He^{2+} ions on damage in zircon is investigated, in analogy with their natural occurrence in alpha decay. In the last experiment (Váczi & Nasdala, 2008), the influence of the extremely common electron beam microanalysis on zircon damage is studied systematically to explore changes caused by electron doses that occur in everyday analysis conditions. Note that both studies are work in progress and been published as conference presentations, therefore they are dealt here in a somewhat extended length.

3.4.1. Helium ion irradiation: a simulation of the influence of alpha-particles

Alpha particles created in alpha events are highly energetic (3.9–8.8 MeV in the U and Th decay chains) but they are less ineffective than heavy particles, such as recoil ions, in creating permanent structural damage in solids (*ca.* 15% of the bulk damage comes from alpha emission; Wasilewski *et al.*, 1973; Nasdala *et al.*, 2001). Instead, electronic and vibrational interactions dominate through most of their trajectory; direct knock-on damage is concentrated in the last few micrometres (*e.g.* Weber *et al.*, 1998; Nasdala *et al.*, 2006b). In natural zircon alpha-particle and recoil damage occurs simultaneously. Although the two trails are created in opposite directions, the decay events are scattered and trails are oriented randomly; therefore, it is not feasible to separate the effects of the two types of particles in the case of self-irradiation. Artificial, external irradiation by $^4He^{2+}$ ions (which are analogous to alpha particles), accelerated to the appropriate kinetic energy, may be used to simulate and assess the effect of only the alpha-particles on zircon. It has been suggested (Hendriks & Redfield, 2005) that through electronic interactions some of the pre-existing radiation damage may be annealed by alpha particles in apatite. The study outlined here (Nasdala *et al.*, 2009a), published as a presentation at the MAPT 2009 Conference (Edinburgh, Scotland), aimed to test whether alpha-particle irradiation is able to reduce the damage level in self-irradiated zircon, or on the contrary, more damage is created.

Polished surfaces of samples from zero to complete radiation damage were irradiated normal to the surfaces by 8.8 MeV He^{2+} ions at a tandem accelerator (FZD Rossendorf-Dresden, Germany) in a parallel beam at a dose of $10^{16}/cm^2$. Irradiated samples were then prepared to show a cross-section of the area of irradiation parallel to the irradiation direction. Raman line scans were recorded with 1 µm steps to reveal the structural state (short-range order) as a function of the distance from the irradiated surface. With the exception of the fully amorphous sample, radiation damage was increased through the entire flight path of the alpha particles, significantly peaking at the distance that corresponds very well to the stopping ranges in zircon (*ca.* 32 µm in pure, crystalline zircon, but slightly increasing with initial damage, and hence the density of the sample; see Fig. 6a). In the range between 0 and *ca.* 30 µm from the irradiated surface the damage level is very slightly higher than the

"background" (*i.e.*, in non-irradiated zircon), seen as slightly increased Raman band widths. No decrease in damage levels was found in any of the samples. Raman observations are fully consistent with luminescence (CL, PL) imaging of irradiated profiles of moderately damaged samples. Non-irradiated zircon luminescence emission is dominated by a dark blue broad band. The irradiated volume shows an intense yellow, broad-band emission, with the exception of a narrow, dark strip, in which luminescence emission is most probably quenched due to the elevated concentration of defect centres at the distance where most atomic displacements are expected. The same quenching effect is shown on PL images in Figure 6b. These observations confirm that the yellow luminescence band in zircon arises from a low concentration of radiation-induced defect centres (Gaft *et al.*, 2005).

These results apparently contradict conclusions of dual-beam experiments (Devanathan *et al.*, 1998) in which the critical dose rate of heavy-ion irradiation to reach amorphisation was found to increase due to light-ion or electron bombardment. Note, however, that in natural zircon (and other actinide-bearing minerals such as monazite) the dose rate is far from those in irradiation experiments (typically on the order of a few alpha events per minute and mm^3) and genuine dual irradiation of any given volume occurs with a very low probability, since the alpha particle and the recoil ion travel in opposite directions. Therefore dual-beam irradiation experiments may only bear relevance to materials with a very high concentration of alpha emitters (nuclear waste forms, *e.g.* Weber, 1990; Geisler *et al.*, 2005). Alpha-assisted annealing, which was observed for fission trails in apatite (*e.g.* Hendriks & Redfield, 2005), was not confirmed in naturally radiation-damaged zircon in this study.

3.4.2. Electron irradiation: an assessment of the influence of electron microprobe analysis

Electron microprobe analysis is perhaps the most common tool to investigate the chemical composition of zircon. The analyses are typically done with a moderate-energy electron beam (15–20 keV, while 100–300 keV and above is used in TEM) but occasionally with a very high probe current to achieve good signal counting statistics (usually from *ca.* 10 to 200 nA and above in EPMA; in contrast, *ca.* 1 nA or less is typically used in a TEM). Though generally "beam damage" is associated with electron beam irradiation, Nasdala *et al.* (2002, 2003) have shown examples of the recovery of short-range order at the location of

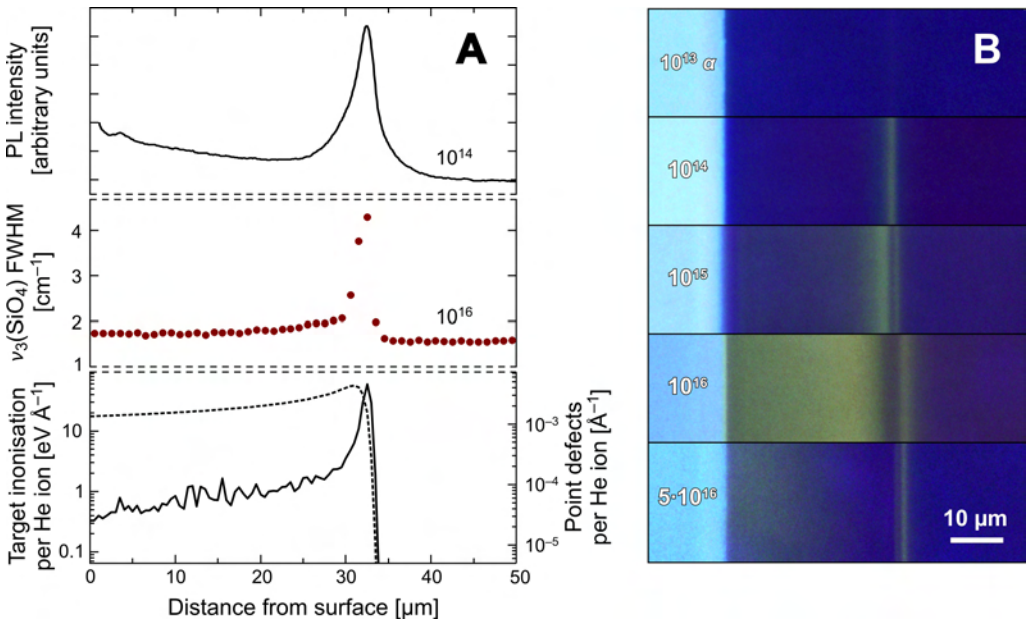

Fig. 6. Damage induced in synthetic zircon by He-ion irradiation. All doses are given in He ions/cm^2.
A Top: PL emission intensity. Middle: Raman band broadening (indicating short-range order). Bottom: ionisation and point defect distribution, predicted by MC simulations, as a function of the distance from the surface.
B Optical microscopy PL images showing the effect of five different irradiation doses. Irradiation direction is from the left, samples were cut perpendicular to the irradiated surface. At low doses, yellow PL is generated, while PL is quenched by strong displacement damage at higher doses, first near the stopping range of He ions (*ca.* 32 µm from the surface; see A).

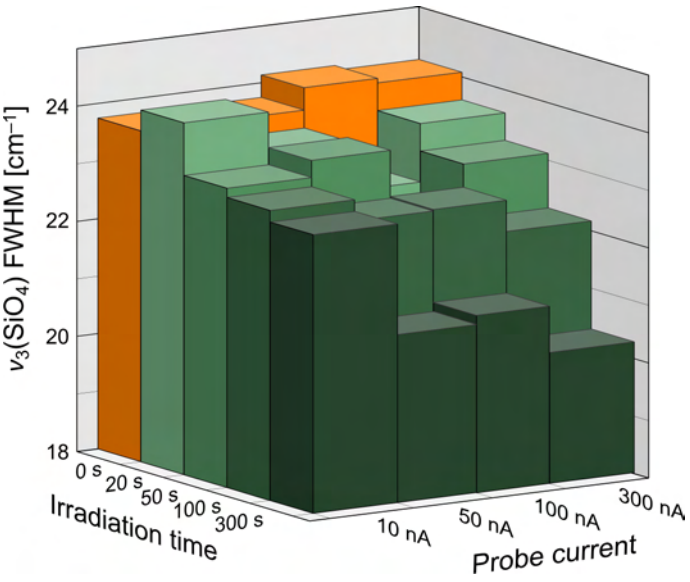

Fig. 7. The effect of electron irradiation dose on the short-range order of zircon. Smaller FWHM indicates better crystallinity. Note that the error in Raman broadening values (vertical axis) is at least 0.5 cm^{-1}, therefore significant changes are only observed at large doses. Sample G168, strong initial damage (2.8–3.0·10^{18} α events/g; for original sample description see Nasdala *et al.*, 2004).

EPMA analysis spots. This study, published as a presentation (Váczi & Nasdala, 2008) at the Georaman '08 Conference (Ghent, Belgium), intended to quantify the systematic change between electron dose (a product of beam current and irradiation time) and the increase of short-range order, based on the change in the $\nu_3(SiO_4)$ zircon Raman band width. The irradiation doses were chosen so that results should be useful to assess the impact of electron microprobe analyses on zircon, especially regarding subsequent structural microanalysis such as Raman measurements.

A series of zircon gemstones and a pure, synthetic $ZrSiO_4$ crystal, spanning the initial radiation damage range between fully crystalline and completely metamict, were irradiated using an electron microprobe operated at 20 kV. The electron beam was fully focused. Irradiation times and probe currents were chosen to be of relevance to practical analytical work; times between 20 s and 300 s and currents between 10 and 200 nA were applied to the samples. The electron irradiation had no observable effect on the two "extreme" samples; no significant Raman parameter changes were recorded in the synthetic (no initial radiation damage) and the fully metamict zircon. Samples with intermediate radiation damage were found to follow a trend of decreasing Raman band width (*i.e.*, a restoration of short-range order) with increasing electron dose (Fig. 7). The trend appears to be not uniform with electron dose; it appears from the data that a high current in a short time has a larger effect than smaller currents in longer times. This study is still in progress; due to the difficulties of precisely relocating irradiation spots and to sample preparation artefacts, the Raman results are not reliable enough to draw precise final conclusions, *e.g.* on whether an "incubation" dose exists or not. In conclusion, care should be taken to avoid strain as an artefact of sample preparation. On the other hand, the results confirm that under a moderate-energy electron beam not only beam damage may but also recrystallisation may occur. In general, structural microanalysis, including *e.g.* Raman and IR spectroscopy, should therefore be done before electron probe chemical analysis to avoid artefacts from modified crystalline order.

4. References

Butterman, W.C. & Foster, W.R. (1967): Zircon stability and the ZrO_2-SiO_2 phase diagram. *American Mineralogist*, **52**: 880–885.

Capitani, G.C., Leroux, H., Doukhan, J.C., Ríos, S., Zhang, M. & Salje, E.K.H. (2000): A TEM investigation of natural metamict zircons: structure and recovery of amorphous domains. *Physics and Chemistry of Minerals*, **27**: 545–556.

Chakoumakos, B.C., Murakami, T., Lumpkin, G.R. & Ewing, R.C. (1987): Alpha-decay–induced fracturing in zircon: The transition from the crystalline to the metamict state. *Science*, **236**: 1556–1559.

Chakoumakos, B.C., Oliver, W.C., Lumpkin, G.R. & Ewing, R.C. (1991): Hardness and elastic modulus of zircon as a function of heavy-particle irradiation dose: I. *In situ* α-decay event damage. *Radiation Effects and Defects in Solids*, **118**: 393–403.

Cherniak, D.J. & Watson, E.B. (2001): Pb diffusion in zircon. *Chemical Geology*, **172**: 5–24.

Cherniak, D.J. & Watson, E.B. (2003): Diffusion in zircon. *In* Hanchar, J.M. & Hoskin, P.W.O. (eds.): *Zircon* /*Reviews in Mineralogy and Geochemistry*, **53**/. Washington, D.C.: Mineralogical Society of America, 113–143.

Colombo, M. & Chrosch, J. (1998a): Annealing of natural metamict zircons. I low degree of radiation damage. *Radiation Physics and Chemistry*, **53**: 555–561.

Colombo, M. & Chrosch, J. (1998b): Annealing of natural metamict zircons. II high degree of radiation damage. *Radiation Physics and Chemistry*, **53**: 563–566.

Corfu, F., Hanchar, J.M., Hoskin, P.W.O. & Kinny, P. (2003): Atlas of zircon textures. *In* Hanchar, J.M. & Hoskin, P.W.O. (eds.): *Zircon* /*Reviews in Mineralogy and Geochemistry*, **53**/. Washington, D.C.: Mineralogical Society of America, 469–500.

Dawson, P., Hargreave, M.M. & Wilkinson, G.R. (1971): The vibrational spectrum of zircon ($ZrSiO_4$). *Journal of Physics C: Solid State Physics*, **4**: 240–256.

Devanathan, R., Sickafus, K.E., Weber, W.J. & Nastasi, M. (1998): Effects of ionizing radiation in ceramics. *Journal of Nuclear Materials*, **253**: 113–119.

Devanathan, R., Corrales, L.R., Weber, W.J., Chartier, A. & Meis, C. (2006): Molecular dynamics simulation of energetic uranium recoil damage in zircon. *Molecular Simulation*, **32**: 1069–1077.

Ewing, R.C., Meldrum, A., Wang, L., Weber, W.J. & Corrales, L.R. (2003): Radiation effects in zircon. *In* Hanchar, J.M. & Hoskin, P.W.O. (eds.): *Zircon* /*Reviews in Mineralogy and Geochemistry*, **53**/. Washington, D.C.: Mineralogical Society of America, 387–425.

Finch, R.J. & Hanchar, J.M. (2003): Structure and chemistry of zircon and zircon-group minerals. *In* Hanchar, J.M. & Hoskin, P.W.O. (eds.): *Zircon* /*Reviews in Mineralogy and Geochemistry*, **53**/. Washington, D.C.: Mineralogical Society of America, 1–25.

Frondel, C. (1953): Hydroxyl substitution in thorite and zircon. *American Mineralogist*, **38**: 1007–1018.

Gaft, M., Reisfeld, R. & Panczer, G. (2005): *Modern Luminescence Spectroscopy of Minerals and Materials.* Berlin: Springer, 356 p.

Geisler, T., Pidgeon, R.T., Van Bronswijk, W. & Pleysier, R. (2001a): Kinetics of thermal recovery and recrystallization of partially metamict zircon: a Raman spectroscopic study. *European Journal of Mineralogy*, **13**: 1163–1176.

Geisler, T., Ulonska, M., Schleicher, H., Pidgeon, R.T. & van Bronswijk, W. (2001b): Leaching and differential recrystallization of metamict zircon under experimental hydrothermal conditions. *Contributions to Mineralogy and Petrology*, **141**: 53–65.

Geisler, T., Pidgeon, R.T., Kurtz, R., van Bronswijk, W. & Schleicher, H. (2003a): Experimental hydrothermal alteration of partially metamict zircon. *American Mineralogist*, **88**: 1496–1513.

Geisler, T., Rashwan, A.A., Rahn, M.K.W., Poller, U., Zwingmann, H., Pidgeon, R.T., Schleicher, H. & Tomaschek, F. (2003b): Low-temperature hydrothermal alteration of natural metamict zircons from the Eastern Desert, Egypt. *Mineralogical Magazine*, **67**: 485–508.

Geisler, T., Burakov, B.E., Zirlin, V., Nikolaeva, L. & Pöml, P. (2005): A Raman spectroscopic study of high-uranium zircon from the Chernobyl “lava”. *European Journal of Mineralogy*, **17**: 883–894.

Hanchar, J.M., Finch, R.J., Hoskin, P.W.O., Watson, E.B., Cherniak, D.J. & Mariano, A.N. (2001): Rare earth elements in synthetic zircon: Part 1. Synthesis, and rare earth element and phosphorus doping. *American Mineralogist*, **86**: 667–680.

Hendriks, B.W.H. & Redfield, T.F. (2005): Apatite fission track and (U-Th)/He data from Fennoscandia: An example of underestimation of fission track annealing in apatite. *Earth and Planetary Science Letters*, **236**: 443–458.

Holland, H.D. & Gottfried, D. (1955): The effect of nuclear radiation on the structure of zircon. *Acta Crystallographica*, **8**: 291–300.

Hoskin, P.W.O. & Rodgers, K.A. (1996): Raman spectral shift in the isomorphous series $(Zr_{1-x}Hf_x)SiO_4$. *European Journal of Solid State and Inorganic Chemistry*, **33**: 1111–1121.

Hoskin, P.W.O. & Schaltegger, U. (2003): The composition of zircon and igneous and metamorphic petrogenesis. *In* Hanchar, J.M. & Hoskin, P.W.O. (eds.): *Zircon /Reviews in Mineralogy and Geochemistry*, **53**/. Washington, D.C.: Mineralogical Society of America, 27–62.

Jiang, N. & Spence, J.C.H. (2009): Radiation damage in zircon by high-energy electron beams. *Journal of Applied Physics*, **105**: 123517.

Kaiser, A., Lobert, M. & Telle, R. (2008): Thermal stability of zircon ($ZrSiO_4$). *Journal of the European Ceramic Society*, **28**: 2199–2211.

Kim, H. & McIntyre, P.C. (2002): Spinodal decomposition in amorphous metal–silicate thin films: Phase diagram analysis and interface effects on kinetics. *Journal of Applied Physics*, **92**: 5094–5102.

Knittle, E. & Williams, Q. (1993): High-pressure Raman spectroscopy of $ZrSiO_4$: Observation of the zircon to scheelite transition at 300 K. *American Mineralogist*, **78**: 245–252.

Kober, B. (1986): Whole-grain evaporation for $^{207}Pb/^{206}Pb$-age-investigations on single zircons using a double-filament thermal ion source. *Contributions to Mineralogy and Petrology*, **93**: 482–490.

Kober, B. (1987): Single-zircon evaporation combined with Pb^+ emitter bedding for $^{207}Pb/^{206}Pb$-age investigations using thermal ion mass spectrometry, and implications to zirconology. *Contributions to Mineralogy and Petrology*, **96**: 63–71.

Krickl, R., Nasdala, L., Götze, J., Grambole, D. & Wirth, R. (2008): Alpha-irradiation effects in SiO_2. *European Journal of Mineralogy*, **20**: 517–522.

Lee, J.K.W. & Tromp, J. (1995): Self-induced fracture generation in zircon. *Journal of Geophysical Research: Solid Earth*, **100**: 17753–17770.

Lian, J., Ríos, S., Boatner, L.A., Wang, L.M. & Ewing, R.C. (2003): Microstructural evolution and nano-crystal formation in Pb^+-implanted $ZrSiO_4$ single crystals. *Journal of Applied Physics*, **94**: 5695–5703.

Lian, J., Wang, L.M., Sun, K. & Ewing, R.C. (2009): In situ TEM of radiation effects in complex ceramics. *Microscopy Research and Technique*, **72**: 165–181.

Lumpkin, G.R. (2001): Alpha-decay damage and aqueous durability of actinide host phases in natural systems. *Journal of Nuclear Materials*, **289**: 136–166.

Markwort, L., Kip, B., Dasilva, E. & Roussel, B. (1995): Raman imaging of heterogeneous polymers: A comparison of global versus point illumination. *Applied Spectroscopy*, **49**: 1411–1430.

Mattinson, J.M. (2005): Zircon U–Pb chemical abrasion ("CA–TIMS") method: Combined annealing and multi-step partial dissolution analysis for improved precision and accuracy of zircon ages. *Chemical Geology*, **220**: 47–66.

Meldrum, A., Boatner, L.A. & Ewing, R.C. (1997): Electron-irradiation-induced nucleation and growth in amorphous $LaPO_4$, $ScPO_4$, and zircon. *Journal of Materials Research*, **12**: 1816–1827.

Meldrum, A., Boatner, L.A., Weber, W.J. & Ewing, R.C. (1998): Radiation damage in zircon and monazite. *Geochimica et Cosmochimica Acta*, **62**: 2509–2520.

Monaghan, S., Greer, J.C. & Elliott, S.D. (2005): Thermal decomposition mechanisms of hafnium and zirconium silicates at the atomic scale. *Journal of Applied Physics*, **97**: 114911.

Mumpton, F.A. & Roy, R. (1961): Hydrothermal stability studies of the zircon–thorite group. *Geochimica et Cosmochimica Acta*, **21**: 217–238.

Murakami, T., Chakoumakos, B.C., Ewing, R.C., Lumpkin, G.R. & Weber, W.J. (1991): Alpha-decay event damage in zircon. *American Mineralogist*, **76**: 1510–1532.

Nasdala, L., Irmer, G. & Wolf, D. (1995): The degree of metamictization in zircon: a Raman spectroscopic study. *European Journal of Mineralogy*, **7**: 471–478.

Nasdala, L., Wenzel, M., Vavra, G., Irmer, G., Wenzel, T. & Kober, B. (2001): Metamictisation of natural zircon: accumulation versus thermal annealing of radioactivity-induced damage. *Contributions to Mineralogy and Petrology*, **141**: 125–144.

Nasdala, L., Lengauer, C.L., Hanchar, J.M., Kronz, A., Wirth, R., Blanc, P., Kennedy, A.K. & Seydoux-Guillaume, A.-M. (2002): Annealing radiation damage and the recovery of cathodoluminescence. *Chemical Geology*, **191**: 121–140.

Nasdala, L., Zhang, M., Kempe, U., Panczer, G., Gaft, M., Andrut, M. & Plötze, M. (2003): Spectroscopic methods applied to zircon. *In* Hanchar, J.M. & Hoskin, P.W.O. (eds.): *Zircon*

/*Reviews in Mineralogy and Geochemistry*, **53**/. Washington, D.C.: Mineralogical Society of America, 427–467.

Nasdala, L., Reiners, P.W., Garver, J.I., Kennedy, A.K., Stern, R.A., Balan, E. & Wirth, R. (2004): Incomplete retention of radiation damage in zircon from Sri Lanka. *American Mineralogist*, **89**: 219–231.

Nasdala, L., Hanchar, J.M., Kronz, A. & Whitehouse, M.J. (2005): Long-term stability of alpha particle damage in natural zircon. *Chemical Geology*, **220**: 83–103.

Nasdala, L., Kronz, A., Hanchar, J.M., Tichomirowa, M., Davis, D.W. & Hofmeister, W. (2006a): Effects of natural radiation damage on back-scattered electron images of single crystals of minerals. *American Mineralogist*, **91**: 1739–1746.

Nasdala, L., Wildner, M., Wirth, R., Groschopf, N., Pal, D.C. & Moller, A. (2006b): Alpha particle haloes in chlorite and cordierite. *Mineralogy and Petrology*, **86**: 1–27.

Nasdala, L., Miletich, R., Ruschel, K. & Váczi, T. (2008): Raman study of radiation-damaged zircon under hydrostatic compression. *Physics and Chemistry of Minerals*, **35**: 597–602.

Nasdala, L., Grambole, D., Váczi, T. & Götze, J. (2009a): Is there alpha-assisted annealing of radiation damage? A helium implantation study of radiation-damaged zircon and monazite. MAPT 2009 (Edinburgh, UK). Book of Abstracts: 167.

Nasdala, L., Hanchar, J.M., Rhede, D., Kennedy, A.K. & Váczi, T. (2009b): Retention of uranium in complexly altered zircon: An example from Bancroft, Ontario. *Chemical Geology*, 10.1016/j.chemgeo.2009.10.004.

Nasdala, L., Kronz, A., Wirth, R., Váczi, T., Pérez-Soba, C., Willner, A. & Kennedy, A.K. (2009c): The phenomenon of deficient electron microprobe totals in radiation-damaged and altered zircon. *Geochimica et Cosmochimica Acta*, **73**: 1637–1650.

Pérez-Soba, C., Villaseca, C., González del Tánago, J. & Nasdala, L. (2007): The composition of zircon in the peraluminous Hercynian granites of the Spanish Central System batholith. *Canadian Mineralogist*, **45**: 509–527.

Pirkle, F.L. & Podmeyer, D.A. (1992): Zircon: origin and uses. *Transactions, Society for Mining, Metallurgy, and Exploration*, **292**: 1872–1880.

Pointer, C.M., Ashworth, J.R. & Ixer, R.A. (1988): The zircon-thorite mineral group in metasomatized granite, Ririwai, Nigeria. 2. Zoning, alteration and exsolution in zircon. *Mineralogy and Petrology*, **39**: 21–37.

Presby, H.M. & Brown, W.L. (1974): Refractive index variations in proton-bombared fused silica. *Applied Physics Letters*, **24**: 511–513.

Putnis, A. (2002): Mineral replacement reactions: from macroscopic observations to microscopic mechanisms. *Mineralogical Magazine*, **66**: 689–708.

Robinson, K., Gibbs, G.V. & Ribbe, P.H. (1971): The structure of zircon: A comparison with garnet. *American Mineralogist*, **56**: 782–790.

Salje, E.K.H., Chrosch, J. & Ewing, R.C. (1999): Is "metamictization" of zircon a phase transition? *American Mineralogist*, **84**: 1107–1116.

Sláma, J., Košler, J., Condon, D.J., Crowley, J.L., Gerdes, A., Hanchar, J.M., Horstwood, M.S.A., Morris, G.A., Nasdala, L., Norberg, N., Schaltegger, U., Schoene, B., Tubrett, M.N. & Whitehouse, M.J. (2008): Plesovice zircon — A new natural reference material for U–Pb and Hf isotopic microanalysis. *Chemical Geology*, **249**: 1–35.

Smith, D.G.W., de St. Jorre, L., Reed, S.J.B. & Long, J.V.P. (1991): Zonally metamictized and other zircons from Thor Lake, Northwest Territories. *Canadian Mineralogist*, **29**: 301–309.

Tabaksblat, R., Meier, R.J. & Kip, B.J. (1992): Confocal Raman microspectroscopy: Theory and application to thin polymer samples. *Applied Spectroscopy*, **46**: 60–68.

Tromans, D. (2006): Solubility of crystalline and metamict zircon: A thermodynamic analysis. *Journal of Nuclear Materials*, **357**: 221–233.

Utsunomiya, S., Valley, J.W., Cavosie, A.J., Wilde, S.A. & Ewing, R.C. (2007): Radiation damage and alteration of zircon from a 3.3 Ga porphyritic granite from the Jack Hills, Western Australia. *Chemical Geology*, **236**: 92–111.

Váczi, T. & Nasdala, L. (2008): Effects of moderate-energy electron irradiation on zircon. Georaman 2008 (Ghent, Belgium). Book of Abstracts: 124.

Váczi, T., Nasdala, L., Wirth, R., Mehofer, M., Libowitzky, E. & Häger, T. (2009): On the breakdown of zircon upon "dry" thermal annealing. *Mineralogy and Petrology*, **97**: 129–138.

Váczi, T., Nasdala, L., Hanchar, J.M., Kronz, A., Götze, J., Dyar, M.D. & Wiedenbeck, M. (submitted): Iron incorporation in zircon. *European Journal of Mineralogy*,

van Westrenen, W., Frank, M.R., Hanchar, J.M., Fei, Y.W., Finch, R.J. & Zha, C.-S. (2004): In situ determination of the compressibility of synthetic pure zircon ($ZrSiO_4$) and the onset of the zircon-reidite phase transition. *American Mineralogist*, **89**: 197–203.

Wang, L.M. & Ewing, R.C. (1992): Detailed in situ study of ion beam-induced amorphization of zircon. *Nuclear Instruments and Methods in Physics Research Section B: Beam Interactions with Materials and Atoms*, **65**: 324–329.

Wang, W.Y., Scarratt, K., Emmett, J.L., Breeding, C.M. & Douthit, T.R. (2006): The effects of heat treatment on zircon inclusions in Madagascar sapphires. *Gems & Gemology*, **42**: 134–150.

Wanthanachaisaeng, B., Häger, T., Hofmeister, W. & Nasdala, L. (2006): Raman- und fluoreszenzspektroskopische Eigenschaften von Zirkon-Einschlüssen in chrom-haltigen Korunden aus Ilakaka und deren Veränderung durch Hitzebehandlung. *Zeitschrift der Deutschen Gemmologischen Gesellschaft*, **55**: 123–136.

Wasilewski, P.J., Senftle, F.E., Vaz, J.E., Thorpe, A.N. & Alexander, C.C. (1973): A study of the natural α-recoil damage in zircon by infrared spectra. *Radiation Effects and Defects in Solids*, **17**: 191–199.

Weber, W.J. (1990): Radiation-induced defects and amorphization in zircon. *Journal of Materials Research*, **5**: 2687–2697.

Weber, W.J., Ewing, R.C. & Wang, L.M. (1994): The radiation-induced crystalline-to-amorphous transition in zircon. *Journal of Materials Research*, **9**: 688–698.

Weber, W.J., Ewing, R.C., Catlow, C.R.A., de la Rubia, T.D., Hobbs, L.W., Kinoshita, C., Matzke, H., Motta, A.T., Nastasi, M., Salje, E.K.H., Vance, E.R. & Zinkle, S.J. (1998): Radiation effects in crystalline ceramics for the immobilization of high-level nuclear waste and plutonium. *Journal of Materials Research*, **13**: 1434–1484.

Wilde, S.A., Valley, J.W., Peck, W.H. & Graham, C.M. (2001): Evidence from detrital zircons for the existence of continental crust and oceans on the Earth 4.4 Gyr ago. *Nature*, **409**: 175–178.

Williams, K.P.J., Pitt, G.D., Batchelder, D.N. & Kip, B.J. (1994): Confocal raman microspectroscopy using a stigmatic spectrograph and CCD detector. *Applied Spectroscopy*, **48**: 232–235.

Willner, A.P., Sindern, S., Metzger, R., Ermolaeva, T., Kramm, U., Puchkov, V. & Kronz, A. (2003): Typology and single grain U/Pb ages of detrital zircons from Proterozoic sandstones in the SW Urals (Russia): early time marks at the eastern margin of Baltica. *Precambrian Research*, **124**: 1–20.

Zhang, M., Salje, E.K.H., Farnan, I., Graeme-Barber, A., Daniel, P., Ewing, R.C., Clark, A.M. & Leroux, H. (2000): Metamictization of zircon: Raman spectroscopic study. *Journal of Physics: Condensed Matter*, **12**: 1915–1925.

Acknowledgements

I wish to express my sincere gratefulness to my supervisor, Lutz Nasdala, for supervising my research activity that has led to the compilation of this PhD thesis. In the past (roughly) three and a half years for all the support he gave me through the doctoral period, including education, experimental experience, travels and so on. He has shown me a good example both professionally and personally; thank you, Lutz.

At the Institute of Mineralogy and Crystallography, University of Vienna, I have found a fine working atmosphere, which is in the first place attributable to the colleagues working here. I had the first contact with them as the technical editor of Volume 6 of the EMU Notes in Mineralogy. Now I wish to explicitly acknowledge the experimental assistance of Eugen Libowitzky, Michael Götzinger, Anton Beran, Herta Effenberger and Gerald Giesler.

The research behind this dissertation has been diverse and truly international. I wish to thank the contributors to my results and the coauthors of the papers I have been involved in, with a perhaps incomplete list of names. I am grateful for their input to Allen Kennedy (Perth), Richard Wirth (Potsdam), Andreas Kronz (Göttingen), John Hanchar (St. John's), Jens Götze (Freiberg), Darby Dyar (South Hadley), Michael Wiedenbeck (Potsdam), Reinhard Kaindl (Innsbruck), Nora Groschopf and Tobias Häger (Mainz), Manfred Wildner, Mathias Mehofer and Theodoros Ntaflos (Vienna). Samples have, naturally, been an obviously indispensable part of this work. Here is the place, therefore, to acknowledge the supply of samples for John Hanchar, Wolfgang Hofmeister, Cecilia Pérez-Soba, Arne Willner, Jan Košler and Raymond Jonckheere. I also thank Andreas Wagner the preparation of excellent sample mounts.

This is also the place to give credit for the funding of the research, travel and subsistence costs. I thank in the first place the Institute of Mineralogy and Crystallography and in particular its past head, Ekkehart Tillmanns, for the generous support in those times not covered by projects. My PhD position was established in the frame of the Marie Curie Chair of Excellence in /for Mineral Spectroscopy (MINSPEC), and partial funding was provided by the European Commission through contract MEXC-CT-2005-024878. Another financial source was the Austrian Science Fund (FWF) grant no. P20028-N10. Visits to external laboratories were partly made possible by the support of the Research Infrastructures Transnational Access (RITA) programme (contract no. 025646).

Apart from the purely scientific points, I wish to show genuine appreciation for my private background, in the first place for the patience, encouragement and understanding of my girlfriend, Izabella Farkas. I also feel thankful to my mother for all I received from her – her support through the major part of my life made it possible for me to reach this point. Here I also wish to show my appreciation to my earlier professors in Budapest, especially Tamás Weiszburg and István Dódony, for providing me with the sound background during my education as a geologist, and for the ongoing good relationship. And finally, I wish to mention Katja Ruschel, to thank her for her friendliness and selfless support.

Appendix 1

Nasdala, L., Miletich, R., Ruschel, K. & Váczi, T. (2008): Raman study of radiation-damaged zircon under hydrostatic compression. *Physics and Chemistry of Minerals*, **35/10:** 597–602.

Phys Chem Minerals (2008) 35:597–602
DOI 10.1007/s00269-008-0251-5

ORIGINAL PAPER

Raman study of radiation-damaged zircon under hydrostatic compression

Lutz Nasdala · Ronald Miletich · Katja Ruschel · Tamás Váczi

Received: 25 April 2008 / Accepted: 19 June 2008 / Published online: 21 August 2008

Abstract Pressure-induced changes of Raman band parameters of four natural, gem-quality zircon samples with different degrees of self-irradiation damage, and synthetic $ZrSiO_4$ without radiation damage, have been studied under hydrostatic compression in a diamond anvil cell up to $\sim$10 GPa. Radiation-damaged zircon shows similar up-shifts of internal SiO_4 stretching modes at elevated pressures as non-damaged $ZrSiO_4$. Only minor changes of band-widths were observed in all cases. This makes it possible to estimate the degree of radiation damage from the width of the $\nu_3(SiO_4)$ band of zircon inclusions in situ, almost independent from potential "fossilized pressures" or compressive strain acting on the inclusions. An application is the non-destructive analysis of gemstones such as corundum or spinel: broadened Raman bands are a reliable indicator of self-irradiation damage in zircon inclusions, whose presence allows one to exclude artificial color enhancement by high-temperature treatment of the specimen.

Keywords Zircon · Radiation damage · Diamond anvil cell · Raman spectroscopy

L. Nasdala (✉) · K. Ruschel · T. Váczi
Institut für Mineralogie und Kristallographie, Universität Wien, Althanstr. 14, 1090 Wien, Austria
e-mail: lutz.nasdala@univie.ac.at

R. Miletich
Mineralogisches Institut, Ruprecht-Karls-Universität Heidelberg, Im Neuenheimer Feld 236, 69120 Heidelberg, Germany

Introduction

The accumulation of self-irradiation damage in zircon ($ZrSiO_4$) leads to dramatic changes of physical properties and chemical resistance of this mineral and may finally lead to an amorphous "metamict" form (e.g., Ewing et al. 2003). The damage originates from the radioactive decay (i.e., alpha-decay events) of U and Th substituting on the Zr^{4+} sites within the lattice, and their instable daughter nuclei in the respective decay chains. The degree of radiation damage that is present in a certain sample, however, does not necessarily correlate with the self-irradiation dose. It has been shown that radiation damage is the result of the two competing processes damage accumulation and damage annealing, controlled by the sample's thermal history (Meldrum et al. 1999).

Nasdala et al. (1995) have introduced Raman spectroscopy as a method to estimate quantitatively the degree of radiation damage in zircon. They showed that Raman spectra of mildly to strongly radiation-damaged (but not yet amorphized) zircon show the same pattern of Raman bands as crystalline zircon. Bands, however, clearly shift towards lower wavenumbers and broaden, which reflects the loss of short-range order and the general expansion of the lattice. The FWHM (full width at half band-maximum) of the internal $\nu_3(SiO_4)$ mode at $\sim$1,000 cm^{-1} was found to increase most sensitively with increasing radiation damage. It increases from $<$2 cm^{-1} for well-crystallized (i.e., undamaged) to well above 30 cm^{-1} for strongly radiation-damaged zircon. This parameter was used in many recent studies to estimate the degree of metamictization of unknown zircon samples. The Raman-based estimation of radiation damage provides the opportunity to do non-destructive in situ analyses with resolution on a micron-scale, opening up new opportunities for studying

the structural state of single zones and areas within zircon grains, and their internal heterogeneity. Applications were presented, for instance, by Wopenka et al. (1996), Hoskin and Black (2000), Zhang et al. (2000), Balan et al. (2001), and Pidgeon et al. (2007).

The objective of the present paper is to study the Raman spectral changes of radiation-damaged zircon (or, more precisely, zircon-structured $ZrSiO_4$) at elevated pressure. Such data have only been provided for crystalline zircon thus far by Knittle and Williams (1993), who found that $ZrSiO_4$ transforms from the zircon-type to a scheelite-type high-pressure polymorph at $\sim$37 GPa. Pressures applied in the present study have remained well below this transition. Note that the present study deals with effects of hydrostatic compression on the spectral behavior of zircon with accumulated self-irradiation damage. It is therefore not closely related to recent papers addressing the question how pressure affects the formation of local material changes, i.e., the process of damage accumulation due to relativistic heavy ions under pressure (e.g., Glasmacher et al. 2006; Lang et al. 2005, 2008). In contrast, we have focused on the following questions: (1) which spectral changes are observed for existing radiation damage in zircon on pressure changes within the hydrostatic regime; (2) as to which degree trends of spectral changes of significantly radiation-damaged zircon differ from those of non-damaged $ZrSiO_4$; and finally (3) whether or not the presence of pressure affects the quantification of radiation damage using the FWHM of the $\nu_3(SiO_4)$ Raman mode.

Samples and experimental

We have studied small chips of four zircon gemstones (ages 522–571 Ma) originating from the Sri Lankan Highland Complex, and synthetic (un-doped) $ZrSiO_4$. The latter was grown using the Li–Mo flux technique described by Hanchar et al. (2001). Chemical and isotopic composition and structural state of the four natural samples, namely M144, BR231, OR1, and G168, have been described in detail elsewhere (Nasdala et al. 2004). They cover the range from mildly (M144; 436 ppm U) to strongly radiation-damaged (G168; 1,499 ppm U). For analytical characterization of the synthetic (i.e., very-well crystallized) $ZrSiO_4$ see Nasdala et al. (2002b).

High-pressure experiments up to $\sim$10 GPa were performed in three runs using an "ETH-type" diamond anvil cell (DAC) that has been described in detail by Miletich et al. (2000). For all three individual loadings 0.09 ct type Ia low-fluorescence diamond anvils with 0.6 mm culets were placed on standard Be backing plates with 15° opening angles for the optical ports. The pre-indented steel gaskets had thicknesses of 85–95 μm, and the diameter of the mechanically-drilled circular pressure chamber was in the range 205–250 μm. The cell was loaded with one or two un-oriented crystal fragments (longest dimensions 90–150 μm). Cryogenically loaded argon was used as pressure-transmitting medium. For the determination of pressure inside the DAC, several small ruby spheres (sizes ca. 5–10 μm) were loaded together with zircon fragments. Pressures were calculated from the spectral position of the laser-induced R_1 emission line ($^2E \rightarrow {}^4A_2$ transition; Nelson and Sturge 1965) of Cr^{3+} centers incorporated in Al_2O_3. The R_1 emission lies at 14,405 cm^{-1} (which corresponds to $\lambda = 694.2$ nm) at ambient conditions and is shifted to lower wavenumbers (i.e., higher wavelengths) at elevated pressures. Calibrations have been provided, for instance, by Piermarini et al. (1975) and Mao et al. (1986). Measurements were done at least 30 min after manual pressure increase or decrease, to reach equilibrium conditions of pressure setting in the DAC. Pressures were derived from the wavelength shift relative to the respective measurement at 1 bar after complete pressure release, using the empirical calibration parameters given by Mao et al. (1986) for hydrostatic conditions.

Raman spectra were obtained by means of a Renishaw RM1000 spectrometer equipped with Leica DMLM optical microscope, a grating with 1,200 grooves per mm, and a Peltier-cooled charge-coupled device (CCD) detector. Spectra were excited with the 785 nm emission line of a NIR (near infrared) diode laser. The laser power at the sample was <3 mW, which is well below the threshold for any heating effects that hypothetically could be caused by local absorption of the laser light. A 20× ULWD (ultra-long working distance) objective (numerical aperture 0.40, free working distance $\sim$11 mm) was used. With this objective, the lateral resolution (with the system operated in the quasi-confocal mode) is estimated at about 20–30 μm, which was powerful enough for our needs. The spectrometer was calibrated using neon lamp emissions (cf. Lide 2003), in particular those at 14219.87 cm^{-1} (703.24 nm), 14431.12 cm^{-1} (692.95 nm), and 14887.5 cm^{-1} (671.7 nm), and the Rayleigh line. All spectra were obtained in the "continuous extended scan" mode, with accumulation times of 10 s for the Rayleigh and neon lamp lines, 30 s for the ruby R lines, and between 60 s (synthetic $ZrSiO_4$) and 900 s (OR1, G168) for zircon Raman spectra. The wavenumber accuracy was better than 0.5 cm^{-1}, and the spectral resolution was determined at $\sim$2.5 cm^{-1}.

Fitting was done assuming Lorentzian–Gaussian band shapes (except for the Rayleigh line, for which a simple Gaussian shape was assumed). Measured FWHMs were corrected for the experimental band broadening (i.e., apparatus function, spectral width of laser emission), and real FWHMs were calculated according to the procedure of

Verma et al. (1995). Estimated uncertainties of corrected FWHMs of the zircon $\nu_3(SiO_4)$ Raman band were between ± 0.4 cm^{-1} (synthetic $ZrSiO_4$) and ± 1.2 cm^{-1} (G168). Uncertainties of determined pressures are assessed to be below ± 0.1 GPa.

Results and discussion

Representative zircon Raman spectra obtained with 785 nm excitation are presented in Fig. 1. Near infrared (NIR) excitation was preferred for two reasons. First, the spectral resolution of a dispersive spectrometer is better at longer wavelengths. This results in bands being defined by more data points, which improves the reliability of fit results especially for narrow bands. Second, with visible excitation, zircon Raman bands are likely to be affected by simultaneously excited laser-induced luminescence emissions. In test measurements with He–Ne 632.8 nm excitation it turned out that the (comparably weak) Raman spectrum of zircon was fully obscured by Cr^{3+} sidebands. Note that in the emission spectrum of Cr^{3+} in corundum, the main R_1 and R_2 lines (emissions of single Cr^{3+} ions) are accompanied by N_1 and N_2 lines (emissions of pairs of closely neighbored Cr^{3+} ions, at 704.1 and 700.9 nm; Powell 1967) and extended sidebands (main emissions modulated by vibrations which have strong intensity in the range 645–740 nm; Rothamel et al. 1983). Even though sidebands are much less intense than R lines, they are still several orders of magnitude higher in intensity than Raman bands. Test measurements with Ar^+ excitation (488 and 514.5 nm) showed significant problems with luminescence phenomena in the case of natural zircon samples. These emissions are assigned to rare earth element (Gaft et al. 2000; Nasdala and Hanchar 2005) and unknown broad-band emission centers in the zircon structure (Gaft et al. 2002).

It should be mentioned that hypothetical problems to excite the red ruby luminescence with the NIR laser did not occur. Direct (i.e., single-photon) excitation of the R_1 emission (photon energy ~ 1.79 eV) was of course impossible, because of the too low photon energy of 785 nm laser light (~ 1.46 eV). Nevertheless, the R lines were excited, and obtained, with sufficient intensity. This may possibly be assigned to a two-photon excitation process.

Natural zircon shows in general comparably weak luminescence in the NIR. However, in spite of the fact that 785 nm excitation was used, the (low-intensity) Raman spectra of all four natural samples were notably affected by luminescence, especially in the range below 834 nm (corresponding to Raman shifts smaller than 750 cm^{-1}; Fig. 1). Nevertheless, the two main Raman bands of zircon at about 1,000 cm^{-1} could be obtained in all cases. These bands are assigned to symmetric stretching (ν_1; A_{1g} mode at ~ 974 cm^{-1}) and antisymmetric stretching (ν_3; B_{1g} mode at $\sim 1{,}008$ cm^{-1}) of SiO_4 tetrahedra in the zircon structure (Dawson et al. 1971; Syme et al. 1977; Mazhenov et al. 1979). Reliable background correction was possible in spite of the significant background intensity, because of the nearly linear (slightly concave) background shape in our spectra (Fig. 1). In contrast, correction for background luminescence consisting of a multitude of narrow emissions (as for instance occurring when Ar^+ 514.5 nm excitation is used; Nasdala and Hanchar 2005) would have introduced clearly more uncertainty. In Fig. 1, background correction and band fitting results are demonstrated for the example of the 5.1 GPa spectrum of zircon OR1.

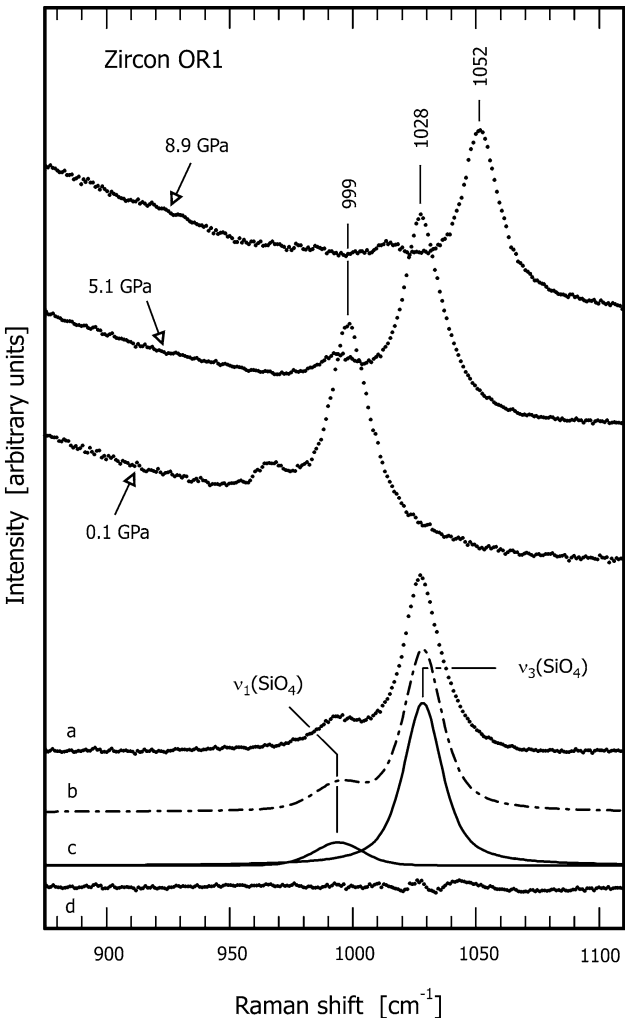

Fig. 1 Raman spectra (785 nm excitation) of zircon OR1 from Sri Lanka, obtained at different pressures. To demonstrate band deconvolution, background-corrected spectrum (**a**), fit result (**b**), fitted single bands (**c**), and difference plot (**d**) are shown below for the example of the 5.1 GPa spectrum

Calculated difference graphs indicated that obtained Raman bands were not affected by significant band asymmetry. This observation is important insofar as it supports quasi-hydrostatic conditions as expected for the pressure medium (argon) used. In contrast, lattices affected by strain due to deviatoric stress under non-hydrostatic conditions typically yield notably asymmetric Raman bands (heterogeneous band broadening; see for example Figs. 1 and 3 in Sharma et al. 1985, Fig. 2b in Nasdala et al. 2002a), which was not observed in the present study over the whole range of experimentally achieved pressures.

Results are shown in Fig. 2. As expected, bands of SiO_4 stretching modes were found to shift towards higher relative wavenumbers (i.e., higher Raman shifts) with increasing pressure. Only for synthetic $ZrSiO_4$ Raman bands in the spectral range below 750 cm^{-1} could be measured (see above). Here, we found that SiO_4 bending and most external modes (including the translational E_g band at 225 cm^{-1}) are up-shifted with pressure, whereas the E_g band at 202 cm^{-1} shows a marked down-shift (to 196 cm^{-1} at 9.0 GPa). All band shifts seemed to occur nearly linearly with pressure, i.e., there was no any clear indication of a hypothetical phase transformation. For the main $\nu_3(SiO_4)$ zircon band, pressure-induced upshifts ($d\tilde{\nu}/dP$) of 5.4–5.9 cm^{-1} GPa^{-1} were calculated for the five samples. These values are slightly higher than the vibrational mode shift of 4.8 ± 0.2 cm^{-1} GPa^{-1} determined by Knittle and Williams (1993).

More importantly, we found that the FWHM of the $\nu_3(SiO_4)$ zircon band does not change significantly with pressure. There is an indication for slight FWHM increase in the case of non- or mildly radiation-damaged zircon (i.e., synthetic $ZrSiO_4$, perhaps also M144), whereas the FWHM seems to decrease at elevated pressures in the case of strongly radiation-damaged samples (G168, OR1). Note that different trends for pressure increase and pressure release were not observed; samples yielded the same Raman parameters within analytical uncertainties before and after having been subjected to high pressures. This is in apparent contrast to the high-pressure study of Knittle and Williams (1993), who detected notable band broadening of zircon after their experiments. However, they applied much higher pressures up to 37 GPa, which seem to have caused some permanent structural damage. Further, our observations do not seem to be consistent with results of a recent study of Trachenko et al. (2007), who reported a final ~5% volume reduction of radiation-amorphized zircon after being compressed to 9 GPa and subsequent pressure release, and that a phase transformation had occurred in the 4.5–9 GPa range. The apparently different observations, however, may be due to the different materials, as Trachenko et al. (2007) studied fully amorphized $ZrSiO_4$, whereas our samples showed much lower levels of radiation damage.

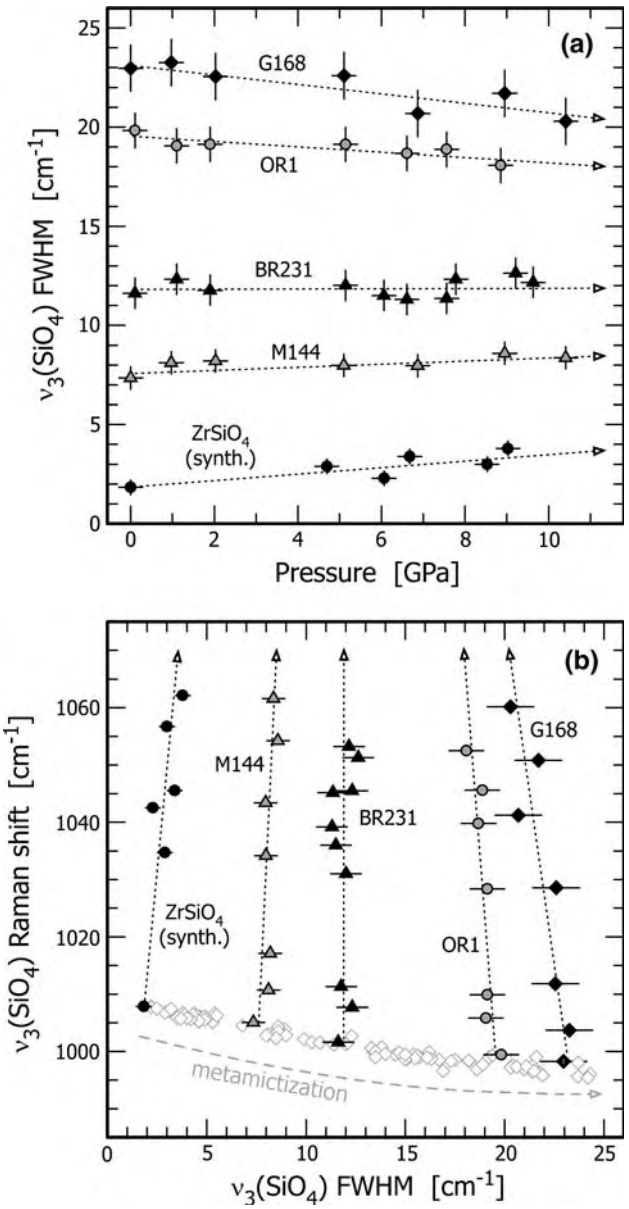

Fig. 2 Raman spectral changes of zircon as induced by pressure: **a** Plot of the width of the $\nu_3(SiO_4)$ Raman band against pressure, **b** Plot of the spectral position of this band against width. Trends of changes with pressure (*dotted lines are visual guides*) deviate significantly from the trend of spectral changes as caused by the accumulation of radiation damage (*gray square symbols and dashed arrow*)

The slight band broadening observed from synthetic $ZrSiO_4$ might perhaps be assigned to a potential effect of quasi-hydrostaticity as originating from the solid argon medium for pressures above 0.9 GPa. However, the reason of the slight FWHM decrease of G168 and OR1 still remains unclear. One possible explanation might be given by considering the different molar volumes and differential compressibilities of the radiation-damaged domains in comparison to the non-damaged host lattice. Assuming the amorphous domains to exhibit a large molar volume and a

smaller bulk modulus for volume compression, the volume strain at the interface between radiation-damaged areas and the host lattice must get reduced on increasing pressures due to smaller volume differences at higher pressures. Accordingly, the FWHM of any spectroscopic signal that is sensitive to strain must get reduced. Increasing non-hydrostaticity at quasi-hydrostatic conditions and this sort of volume–strain reduction at increasing pressure appear to be two competitive effects for the development of the FWHMs related to the radiation damage in zircon. Any consideration of pressure-induced recovery of the radiation damage appears unlikely, in view of the fact that FWHMs decreased non-permanently and recovered to initial values after pressure release. Reliable interpretation of the observed slight FWHM changes with pressure will require further studies. Such studies should also attempt to address the question as to which degree compressive strain acting on included zircon grains (most likely up to a few GPa, or below) might have affected their self-irradiation and, with that, the long-term processes of damage generation and recovery.

All FWHM changes of natural zircon samples, however, are mainly within errors. This is also demonstrated in Fig. 2b: accumulation of alpha-event damage results in substantial FWHM increase, accompanied by rather moderate down-shift of this band, whereas pressure increase results in considerably different trends of spectral changes. These observations suggest that the FWHM of the $\nu_3(SiO_4)$ Raman band is indicative of the degree of self-irradiation but insignificantly affected by pressure acting on the zircon.

This result has important implications. It has been speculated (Wang et al. 2006; Wanthanachaisaeng et al. 2006) as to which degree the radiation damage present in zircon inclusions in high-pressure metamorphic minerals can be evaluated based on FWHMs determined from in situ Raman measurements, or whether elevated pressure acting on inclusions needs to be considered as potential cause of further FWHM changes. The latter suspicion was based on the well-known fact that heterogeneous pressure release of high-pressure host-inclusion couples upon sample uplift may result in significant compressive strain (also referred to as "fossilized pressure" or "overpressure") acting on the inclusion, which may be as high as 2–3 GPa (Parkinson and Katayama 1999; Sobolev et al. 2000; Glinnemann et al. 2003). Our results suggest that such pressures have very minor effect on the widths of internal SiO_4 Raman modes. This makes it possible to estimate the degree of radiation damage from the FWHM of the $\nu_3(SiO_4)$ zircon band, almost independent from whether or not analyzed inclusions are affected by pressure. It is clear, however, that such estimates of the radiation damage of zircon inclusions will be affected with slightly higher uncertainty compared to analogous estimates for unstressed bulk samples. The only major restriction is that such estimates should not be made if strongly asymmetric Raman bands, or even overlapping pairs of bands, are observed (see above). The latter would be indicative for lattice strain due to strongly non-hydrostatic stress conditions, perhaps along with some strain gradient within the analyzed material volume, which is likely to result in apparently too broad bands. In contrast, broadened symmetric Raman bands are a reliable indicator of accumulated radiation damage in zircon.

This result will, for instance, allow gemmologists to use zircon inclusions in evaluating specimens with regard to the common practice of heat treatment to enhance color and clarity. It is well known that radiation damage in zircon is annealed after heat-treatment at 1,000–1,200°C partly or completely, depending on the degree of damage and the duration of the treatment (Zhang et al. 2000; Nasdala et al. 2002b). The detection of radiation damage in zircon inclusions, indicated by strong band broadening, therefore allows one to exclude any heat treatment above this temperature range.

Acknowledgments Zircon samples were kindly made available by J. M. Hanchar (synthetic $ZrSiO_4$), W. Hofmeister (M144), and A. K. Kennedy (BR231, OR1, G168). Thoughtful comments of M. Gaft and an anonymous reviewer are gratefully acknowledged. Partial funding of this research was provided by the European Commission, contract no. MEXC-CT-2005-024878, and the FWF Austrian Science Fund, grant P20028-N10.

References

Balan E, Neuville DR, Trocellier P, Fritsch E, Muller J-P, Calas G (2001) Metamictization and chemical durability of detrital zircon. Am Mineral 86:1025–1033

Dawson P, Hargreave MM, Wilkinson GF (1971) The vibrational spectrum of zircon ($ZrSiO_4$). J Phys C Solid State Phys 4:240–256. doi:10.1088/0022-3719/4/2/014

Ewing RC, Meldrum A, Wang LM, Weber WJ, Corrales LR (2003) Radiation effects in zircon. In: Hanchar JM, Hoskin PWO (eds) Zircon. Reviews in mineralogy and geochemistry, vol 41. Mineralogical Society of America, Washington DC, pp 387–425

Gaft M, Panczer G, Reisfeld R, Shinno I (2000) Laser-induced luminescence of rare-earth elements in natural zircon. J Alloys Com 300–301:267–274

Gaft M, Shinno I, Panczer G, Reisfeld R (2002) Laser-induced time-resolved spectroscopy of visible broad luminescence bands in zircon. Mineral Petrol 76:235–246. doi:10.1007/s007100200043

Glasmacher UA, Lang M, Keppler H, Langenhorst F, Neumann R, Schardt D, Trautmann C, Wagner GA (2006) Phase transitions in solids stimulated by simultaneous exposure to high pressure and relativistic heavy ions. Phys Rev Lett 96:195701-1–195071-4

Glinnemann J, Kusaka K, Harris JW (2003) Oriented graphite single-crystal inclusions in diamond. Z Kristallogr 218:733–739. doi:10.1524/zkri.218.11.733.20302

Hanchar JM, Finch RJ, Hoskin PWO, Watson EB, Cherniak DJ, Mariano AN (2001) Rare earth elements in synthetic zircon: part 1. Synthesis, and rare earth element and phosphorus doping. Am Mineral 86:667–680

Hoskin PWO, Black LP (2000) Metamorphic zircon formation by solid-state recrystallization of protolith igneous zircon. J Metamorph Geol 18:423–439. doi:10.1046/j.1525-1314.2000.00266.x

Knittle E, Williams Q (1993) High-pressure Raman spectroscopy of $ZrSiO_4$: observation of the zircon to scheelite transition at 300 K. Am Mineral 78:245–252

Lang M, Glasmacher UA, Neumann R, Schardt D, Trautmann C, Wagner GA (2005) Energy loss of 50-GeV uranium ions in natural diamond. Appl Phys A 80:691–694. doi:10.1007/s00339-004-3104-1

Lang M, Zhang F, Lian J, Trautmann C, Neumann R, Ewing RC (2008) Irradiation-induced stabilization of zircon ($ZrSiO_4$) at high pressure. Earth Planet Sci Lett 269:291–295. doi:10.1016/j.epsl.2008.02.027

Lide DR (2003) CRC handbook of chemistry and physics, 84th edn. CRC Press, Boca Raton

Mao HK, Xu J, Bell PM (1986) Calibration of the ruby pressure gauge to 800 kbar under quasi-hydrostatic conditions. J Geophys Res 91:4673–4676. doi:10.1029/JB091iB05p04673

Mazhenov NA, Murgorodskij AP, Lazarev AN (1979) Resonance-splitting of inner vibrational frequencies of heavy anions in zircon ($ZrSiO_4$) crystals. Inorg Mater 15:495–503 in Russian

Meldrum A, Zinkle SJ, Boatner LA, Ewing RC (1999) Amorphization, recrystallization, and phase decomposition in the ABO_4 orthosilicates. Phys Rev B 59:3981–3992. doi:10.1103/PhysRevB.59.3981

Miletich R, Allan DR, Kuhs WF (2000) High-pressure single-crystal techniques. In: Hazen RM, Downs RT (eds) High-temperature and high-pressure crystal chemistry. Reviews in mineralogy and geochemistry, vol 41. Mineralogical Society of America, Washington DC, pp 445–519

Nasdala L, Hanchar JM (2005) Comment on: application of Raman spectroscopy to distinguish metamorphic and igneous zircon (Xian et al., Anal Lett (2004) vol. 37, p. 119). Anal Lett 38:727–734

Nasdala L, Irmer G, Wolf D (1995) The degree of metamictization in zircons: a Raman spectroscopic study. Eur J Mineral 7:471–478

Nasdala L, Irmer G, Jonckheere R (2002a) Radiation damage ages: practical concept or impractical vision?—reply to two comments on "Metamictisation of natural zircon: Accumulation versus thermal annealing of radioactivity-induced damage", and further discussion. Contrib Mineral Petrol 143:758–765

Nasdala L, Lengauer CL, Hanchar JM, Kronz A, Wirth R, Blanc P et al (2002b) Annealing radiation damage and the recovery of cathodoluminescence. Chem Geol 191:121–140. doi:10.1016/S0009-2541(02)00152-3

Nasdala L, Reiners PW, Garver JI, Kennedy AK, Stern RA, Balan E et al (2004) Incomplete retention of radiation damage in zircon from Sri Lanka. Am Mineral 89:219–231

Nelson DF, Sturge MD (1965) Relation between absorption and emission in the region of the R lines of ruby. Phys Rev 137:A1117–A1130. doi:10.1103/PhysRev.137.A1117

Parkinson CD, Katayama I (1999) Present-day ultrahigh-pressure conditions of coesite inclusions in zircon and garnet: evidence from laser Raman microspectroscopy. Geology 27:979–982. doi:10.1130/0091-7613(1999)027≤0979:PDUPCO≥2.3.CO;2

Pidgeon RT, Nemchin AA, van Bronswijk W, Geisler T, Meyer C, Compston W et al (2007) Complex history of a zircon aggregate from lunar breccia 73235. Geochim Cosmochim Acta 71:1370–1381. doi:10.1016/j.gca.2006.11.021

Piermarini GJ, Block S, Barnett JD, Forman RA (1975) Calibration of the pressure dependence of the R_1 ruby fluorescence line to 195 kbar. J Appl Phys 46:2774–2780. doi:10.1063/1.321957

Powell RC (1967) Fluorescence studies of energy transfer between single and pair Cr^{3+} systems in Al_2O_3. Phys Rev 155:296–308. doi:10.1103/PhysRev.155.296

Rothamel U, Heber J, Grill W (1983) Vibronic sidebands in ruby. J Phys B Condens Matter 50:297–304. doi:10.1007/BF01470041

Sharma SK, Mao HK, Bell PM, Xu JA (1985) Measurement of stress in diamond anvils with micro-Raman spectroscopy. J Raman Spectrosc 16:350–352. doi:10.1002/jrs.1250160513

Sobolev NV, Fursenko BA, Goryainov SV, Shu JF, Hemley RJ, Mao HK et al (2000) Fossilized high pressure from the Earth's deep interior: the coesite-in-diamond barometer. Proc Natl Acad Sci USA 97:11875–11879. doi:10.1073/pnas.220408697

Syme RWG, Lockwood DJ, Kerr J (1977) Raman spectrum of synthetic zircon ($ZrSiO_4$) and thorite ($ThSiO_4$). J Phys C Solid State Phys 10:1335–1348. doi:10.1088/0022-3719/10/8/036

Trachenko K, Brazhkin VV, Tsiok OB, Dove MT, Salje EKH (2007) Pressure-induced structural transformation in radiation-amorphized zircon. Phys Rev Lett 98:135502-1–135502-4

Verma P, Abbi SC, Jain KP (1995) Raman-scattering probe of anharmonic effects in GaAs. Phys Rev B 51:16660–16667. doi:10.1103/PhysRevB.51.16660

Wang W, Scarratt K, Emmett J, Breeding C, Douthit T (2006) The effects of heat treatment on zircon inclusions in Madagascar sapphires. Gems Gemol 42:134–150

Wanthanachaisaeng B, Häger T, Hofmeister W, Nasdala L (2006) Raman- und fluoreszenz-spektroskopische Eigenschaften von Zirkon-Einschlüssen in chrom-haltigen Korunden aus Ilakaka und deren Veränderung durch Hitzebehandlung. Gemmologie 55:119–132

Wopenka B, Jolliff BL, Zinner E, Kremser DT (1996) Trace element zoning and incipient metamictization in a lunar zircon: application of three microprobe techniques. Am Mineral 81:902–912

Zhang M, Salje EKH, Capitani GC, Leroux H, Clark AM, Schlüter J et al (2000) Annealing of α-decay damage in zircon: a Raman spectroscopic study. J Phys Condens Matter 12:3131–3148. doi:10.1088/0953-8984/12/13/321

Appendix 2

Nasdala, L., Kronz, A., Wirth, R., Váczi, T., Pérez-Soba, C., Willner, A. & Kennedy, A.K. (2009): The phenomenon of deficient electron microprobe totals in radiation-damaged and altered zircon.
Geochimica et Cosmochimica Acta, **73/6:** 1637–1650.

Available online at www.sciencedirect.com
ScienceDirect
Geochimica et Cosmochimica Acta 73 (2009) 1637–1650
Geochimica et Cosmochimica Acta
www.elsevier.com/locate/gca

The phenomenon of deficient electron microprobe totals in radiation-damaged and altered zircon

Lutz Nasdala [a,*], Andreas Kronz [b], Richard Wirth [c], Tamás Váczi [a], Cecilia Pérez-Soba [d], Arne Willner [e], Allen K. Kennedy [f]

[a] *Institut für Mineralogie und Kristallographie, Universität Wien, Austria*
[b] *Geowissenschaftliches Zentrum, Georg-August-Universität Göttingen, Germany*
[c] *Helmholtz-Zentrum Potsdam, Deutsches GeoForschungsZentrum, Potsdam, Germany*
[d] *Departamento de Petrología y Geoquímica, Universidad Complutense, Madrid, Spain*
[e] *Institut für Geologie, Mineralogie und Geophysik, Ruhr-Universität Bochum, Germany*
[f] *Department of Applied Physics, Curtin University of Technology, Perth, WA, Australia*

Received 29 January 2008; accepted in revised form 12 December 2008; available online 24 December 2008

Abstract

The phenomenon of deficient electron microprobe analyses, with sums of analyzed constituents often below 95 wt%, is assigned to the analysis of altered, porous minerals. With the example of three zircon populations we show that low totals are related to textural features (i.e., numerous pores of tens to hundreds of nanometers size) as well as to the chemical composition (i.e., water content well within the wt% range, which may affect partial sample degradation under the electron beam). The formation of the spongy texture is explained by the alteration of a previously radiation-damaged and, thus, volume-expanded material in a fluid-driven replacement reaction. The smaller volume of the reaction product (crystalline, non volume-expanded zircon) accounts for the formation of numerous voids and pores, which are perfect candidates for the incorporation of water. The alteration has also resulted in uptake of non-formula elements such as Al, P, Ca, Fe, Y, and REEs whereas Si and Zr are depleted. In one case, strong uptake of non-radiogenic Pb in altered zircon was observed. Because porous, low-total zircon has formed in secondary alteration process, its occurrence can be considered as an indicator of a secondary alteration history of the host rock. Low-total zircon is easily recognized by very low electron back-scatter intensities, which are closely related to the two main causes of the analytical shortfall (i.e., water content and porosity) and often lowered furthermore by the presence of light non-formula elements (especially P and Fe) up to the wt% range.

1. INTRODUCTION

It has commonly been reported that electron microprobe analyses of radiation-damaged accessory minerals may yield analytical totals that are significantly below 100 wt%, in some cases even well below 90 wt% (e.g., Medenbach, 1976; Speer, 1982; Törnroos, 1985; Pointer et al., 1988a; Smith et al., 1991; Förster, 1998; Mathieu et al., 2001). Such deficient totals were, for instance, observed for minerals of the zircon-thorite orthosilicate group (zircon, $ZrSiO_4$; coffinite, $USiO_4$; thorite, $ThSiO_4$) and orthophosphates ($CePO_4$–YPO_4). However, the majority of such analyses have been reported for zircon.

Causes of the deficient microprobe results are still under debate. Low analytical totals have mostly been ascribed to elevated concentrations of molecular water and/or hydroxyl groups (e.g., Törnroos, 1985; Smith et al., 1991; Geisler et al., 2003a). Correspondingly, the variation of analytical sums from 100 wt% was sometimes assigned to a hypothetical "H_2O^*" (e.g., Johan and Johan, 2005; Utsunomiya et al., 2007). This, however, appears to be somewhat questionable, as the assignment is based on an assumption

* Corresponding author. Fax: +43 1 4277 9532.
E-mail address: lutz.nasdala@univie.ac.at (L. Nasdala).

0016-7037/$ - see front matter © 2008 Elsevier Ltd. All rights reserved.
doi:10.1016/j.gca.2008.12.010

without analytical verification. Also, calculated H_2O^* values of as high as 18.4 wt% (Johan and Johan, 2005) would imply that the water content of that particular zircon sample has exceeded 50 mol%, which appears unlikely. Rubin et al. (1989) suggested that hydrous species may contribute to low totals not only because they are not analyzed in the electron microprobe but also by causing mineral degradation under the electron beam. Breiter et al. (2006) concluded that low totals cannot solely be explained by the presence of water but might also be due to fluorine and other elements not analyzed. Other interpretations include the presence of sub-μm-sized voids (Pointer et al., 1988b) and structural vacancies (Kempe et al., 2000). Pérez-Soba et al. (2007) proposed that the presence of notable quantities of divalent (such as Ca, Fe) and trivalent cations (such as rare earth elements) in low-total zircon may be accompanied, and charge-compensated, by oxygen defects, which also contribute to analytical deficiencies.

Interestingly, there is an accompanying phenomenon: Low totals were always detected in interior regions of zircon crystals that appeared notably darker in back-scattered electron (BSE) images than neighbouring regions of the same crystal (Peterman et al., 1986; Pointer et al., 1988b; Smith et al., 1991; Kempe et al., 2000; Willner et al., 2003). As above, the causes of the anomalously low BSE intensity have remained controversial. In the present study, we have investigated three zircon samples with deficient electron microprobe totals. Apart from chemical analyses and imaging by electron microprobe, the structural and micro-textural state of samples was studied using transmission electron microscopy (TEM) and micro-spectroscopic techniques. With this present study we tried to address both the low totals and the "unusual" BSE intensities. We aim to contribute to the understanding of the physical causes of the deficient totals and unusually low BSE intensities as well as the formation of zircon samples exhibiting these phenomena.

2. SAMPLES AND PREPARATION

We have investigated three populations of zircon grains that frequently have low analytical totals. The first sample consists of late Archaean (age ~2.65 Ga) zircon crystals (>500 μm fraction) from a late monzogranite (Sample No. W64), which has intruded tonalitic gneisses at the southern rim of the Jack Hills in the northern Yilgarn Craton, Western Australia (for geological setting and geochronology see Pidgeon and Wilde, 1998). A second population of zircon grains (80–120 μm fraction) was separated from an upper Riphean (Sample No. 32) and a middle Riphean sandstone (Sample No. 40), located about 100 km southwest of the city of Beloretsk (southern Ural; for more details see Willner et al., 2003). These authors reported notably discordant $^{207}Pb/^{206}Pb$ zircon ages compatible with crystallization in the age range 1.8–2.3 Ga. The third group of zircon crystals (Sample No. 87165; <250 μm fraction) comes from a Hercynian, coarse-grained leucogranite of the La Pedriza pluton in the Spanish Central System batholith, located about 50 km north–northwest of the city of Madrid (Pérez-Soba et al., 2007). Pérez-Soba (1992) reported a Rb-Sr isochron age of 307 ± 3 Ma for the La Pedriza pluton.

For comparison, "regular" zircon crystals (i.e., those with "normal" BSE intensities and analytical totals close to 100 wt%) were also subjected to electron microprobe imaging. These samples included primary zoned, unaltered zircon crystals from a granite in the Jack Hills, Western Australia (Sample No. W34, courtesy of R.T. Pidgeon; for details and age see Pidgeon, 1992), zircon grains from a monzonite near the city of Freital, Meissen massif, Saxony, Germany (Sample No. Frei 10, courtesy of T. Wenzel; for details see Wenzel et al., 1997; Nasdala et al., 1999), zircon grains from a charnockite-granite near the village of Kliprand, Namaqualand, South Africa (Sample No. Nam12, courtesy of A. Möller; for geological setting see Robb et al., 1999), and zircon crystals from a leucogranite north of the village of Dannemora, Adirondack Mountains, New York State (Sample No. JHADK996, courtesy of J.M. Hanchar; for rock description see McLelland et al., 2001).

Zircon grains were embedded in araldite epoxy, ground to about half of their thicknesses to expose their internal textures, and polished. In the case of the Jack Hills zircon crystals, which are considerably larger in size than individual grains from the other localities, doubly polished thin sections (30 μm thickness) attached to a glass slide were produced. Mounts were coated with carbon prior to electron microprobe imaging and analysis. For TEM analysis, site-specific TEM foils (sizes ~10 μm, final thicknesses ~0.1 μm) were cut out of the above sample mounts using a FEI FIB200 (for details of the focused ion beam technique see Wirth, 2004). For Sensitive High mass-Resolution Ion MicroProbe (SHRIMP) analysis of the isotopic composition, flat, polished sample mounts containing unknowns and the CZ3 reference zircon (Pidgeon et al., 1994) were prepared and coated with gold. For transmission infrared absorption analyses of La Pedriza zircon crystals, doubly polished plates (thickness 30 μm) parallel to the crystallographic *c*-axis were produced from single crystals and attached to an aluminium sample holder with a rectangular hole (40–180 μm size). Raman analyses were done on the electron microprobe and ion microprobe mounts after repolishing. However, analyses were placed at least ~10 μm away from the EMPA and SHRIMP spots, respectively, to avoid biased results due to potential structural changes caused by the electron or ion beam.

3. EXPERIMENTAL TECHNIQUES

Analysis of the chemical composition, and back-scattered electron (BSE), secondary electrons (SE), and cathodoluminescence (CL) imaging to visualize internal textures of crystals, were done using a JEOL 8900 RL electron probe microanalyser (EPMA). The BSE and CL images were obtained at 20 kV and 20 nA. Chemical analyses were done with the EPMA operated at 20 kV and a beam current of 80 nA. The electron beam was either focused to a ~2 μm spot, or defocused (15 μm spot diameter). The calibrant materials included synthetic $ZrSiO_4$ (for Zr, Si), $HfSiO_4$ (for Hf), MgO (for Mg), Al_2O_3 (for Al), Y-Al garnet (for Y), REE-CAS glasses (for REE; rare earth elements), $ThSiO_4$ (for Th), and UO_2 (for U); and natural apatite (for P), wollastonite (for Ca), rhodonite (for Mn), and

hematite (for Fe). Counting times were varied between 15 s (peak) and 2 × 5 s (lower and upper background) for the K_α line of Si, and 300 s (peak) and 2 × 150 s (backgrounds) for the M_α lines of U and Th. Data were reduced using the CITZAF routine in the JEOL software, which is based on the $\Phi(\rho Z)$ correction method (Armstrong, 1991, 1995).

Oxygen was, as it is usual in silicate mineral analysis with the electron microprobe, calculated by stoichiometry. However, to check whether this has caused uncertainties (e.g., due to different oxidation states of the cations or the presence of water), it was appropriate to actually analyze oxygen. A number of samples were analyzed again including wavelength-dispersive X-ray analysis of oxygen. Oxygen measurements were performed using a W-Si multilayer detector (LDE1) with 2d-spacing of 60 Å (see Armstrong, 1988; Rybka and Wolf, 1995). Operating conditions were 20 kV and 20 nA beam current measured at the Faraday cup. Synthetic $ZrSiO_4$ was used as the oxygen calibrant. Calibrants and samples were simultaneously coated with carbon (note that due to the high mass-absorption coefficient of carbon on O-K_α X-rays, uniform coating thickness of reference and sample is crucial for reliable oxygen measurements in the EMPA). Counting times for O-K_α were 30 s (peak) and 2 × 15 s (lower and upper background). Multiple measurements ($n = 12$) of the synthetic $ZrSiO_4$ yielded 1σ uncertainties of 0.011 (O), 0.004 (Si), and 0.008 (Zr) per formula unit (based on a total of six ions per formula unit).

Analyses of U and Th concentrations and the Pb isotopic composition were made on a SHRIMP II at Curtin University of Technology, Perth. This system is operated by a consortium consisting of Curtin University, the University of Western Australia, and the Geological Survey of Western Australia. A primary, mass-filtered $(O_2)^-$ beam (~1 nA) was focused to a ~10 μm spot to sputter the sample surface. Data for each spot were collected in sets of eight scans through the mass range of Zr_2O^+, $^{204}Pb^+$, background, $^{206}Pb^+$, $^{207}Pb^+$, $^{208}Pb^+$, $^{238}U^+$, $^{248}ThO^+$, and $^{254}UO^+$. For more experimental details see De Laeter and Kennedy (1998). Data were calibrated versus the CZ3 reference zircon (Pidgeon et al., 1994). The correction for common Pb was made from the observed ^{204}Pb count rate.

Transmission electron microscopy was performed at Helmholtz–Zentrum Potsdam, using a FEI Tecnai G^2 F20 X-Twin system operated at a voltage of 200 kV. The beam current was 0.5 nA. The TEM analytical work included energy-dispersive chemical analyses, electron diffraction, electron energy loss spectroscopy (EELS), and bright field, high angle annular dark field (HAADF), and high-resolution electron microscopy (HREM) imaging.

Infrared (IR) absorption spectroscopy (transmission mode) was done with a Bruker Tensor 27 Fourier-transform infrared (FTIR) system equipped with Hyperion microscope. Spectra were recorded in the transmission mode, in the range 600–7000 cm^{-1}. The spectral resolution was 2 cm^{-1}. Pairs of spectra were obtained with the *E* vector of the infrared light oriented parallel and perpendicular to the crystallographic *c*-axis. Raman spectra were obtained in quasi back-scattering geometry using an edge-filter based Renishaw RM1000 system equipped with Leica DMLM optical microscope. The Leica 50× objective was used, and the system was operated in quasi-confocal mode; resulting in a lateral resolution of ~4–5 μm. The spectral resolution was determined at 2.2 cm^{-1}. Spectra were excited with the 632.8 nm emission of a He–Ne laser (~8 mW at the sample surface).

4. GENERAL CHARACTERIZATION OF LOW-TOTAL ZIRCON

4.1. Chemical composition

A range of images of zircon crystals showing their internal textures is presented in Fig. 1a–g. Results of electron microprobe analyses are listed in Tables 1–3. All samples yielded, at least in some of their interior regions, analytical totals that were significantly deficient, i.e., in the range 91–97 wt%. In samples W64 (Jack Hills) and 32/40 (Ural) these interior regions are rather small whereas zircon crystals from sample 87165 (La Pedriza) were commonly found to be entirely affected by the phenomenon of low totals. Low analytical totals were always detected in micro-areas characterized by very low BSE contrast (Fig. 1a–g); this observation will be discussed in more detail below.

In general, all samples are rich in actinides and contain comparably high levels of non-formula elements. Low-total areas in all samples contain higher levels of light elements (i.e., especially P and Fe, also Al, Ca; Table 1) as well as Y and some of the REEs, compared to neighbouring, un-altered areas of the same crystals. In contrast, heavy non-formula elements including Hf, Th, and U did not show such general trend. For instance, U and Th were found to be higher (Ural) and lower (Jack Hills), respectively, in the altered, low-BSE areas than in neighbouring unaltered areas. The main elements Si and Zr are considerably depleted in low-total areas.

Results presented in Table 1 are tainted with the important uncertainty that deficient totals are oxide sums which are not based on oxide analysis but merely cation analysis, with oxygen being calculated according to the concentration and valence of the cations. In order to get more reliable information, some samples were analyzed including the wavelength-dispersive analysis of oxygen (Table 2). Analogous to the routine electron microprobe analysis, oxygen was calculated from the observed cations (equivalent O in Table 2). These values were generally lower than measured O concentrations, with differences (excess O in Table 2) up to as high as 7.8 wt%. We assign the excess oxygen, at least for a significant part, to water (see below); excess oxygen values were therefore transformed to hypothetical water (H_2O^*) concentrations (Table 2). The calculated excess O (Fig. 2) and H_2O^* values (Table 2) show inverse correlation with Zr (and substitutes) and Si (and substitutes), respectively. This seems to support earlier hypotheses according to which low-total zircon was assumed to be notably hydrous. However, calculated analytical totals considering H_2O^*, for altered, low-BSE zircon, are still slightly (sample 87165) to strongly deficient (sample W64). We interpret the still deficient totals to indicate that water alone may be insufficient to explain the analytical shortfall.

One potential reason for further deficiencies is seen in the fact that the impact of the electron beam is likely to cause dewatering and local disintegration of hydrous, low-total zircon. Aiming to check for such effects, analyses of crystal W64-11 were done with different energy densities of the electron beam but under otherwise uniform conditions (Table 2). After defocusing the electron beam to a 15 μm spot diameter, considerably higher O concentrations (and hence higher calculated H_2O^* values) but still deficient totals were detected in low-BSE zircon areas. These obser-

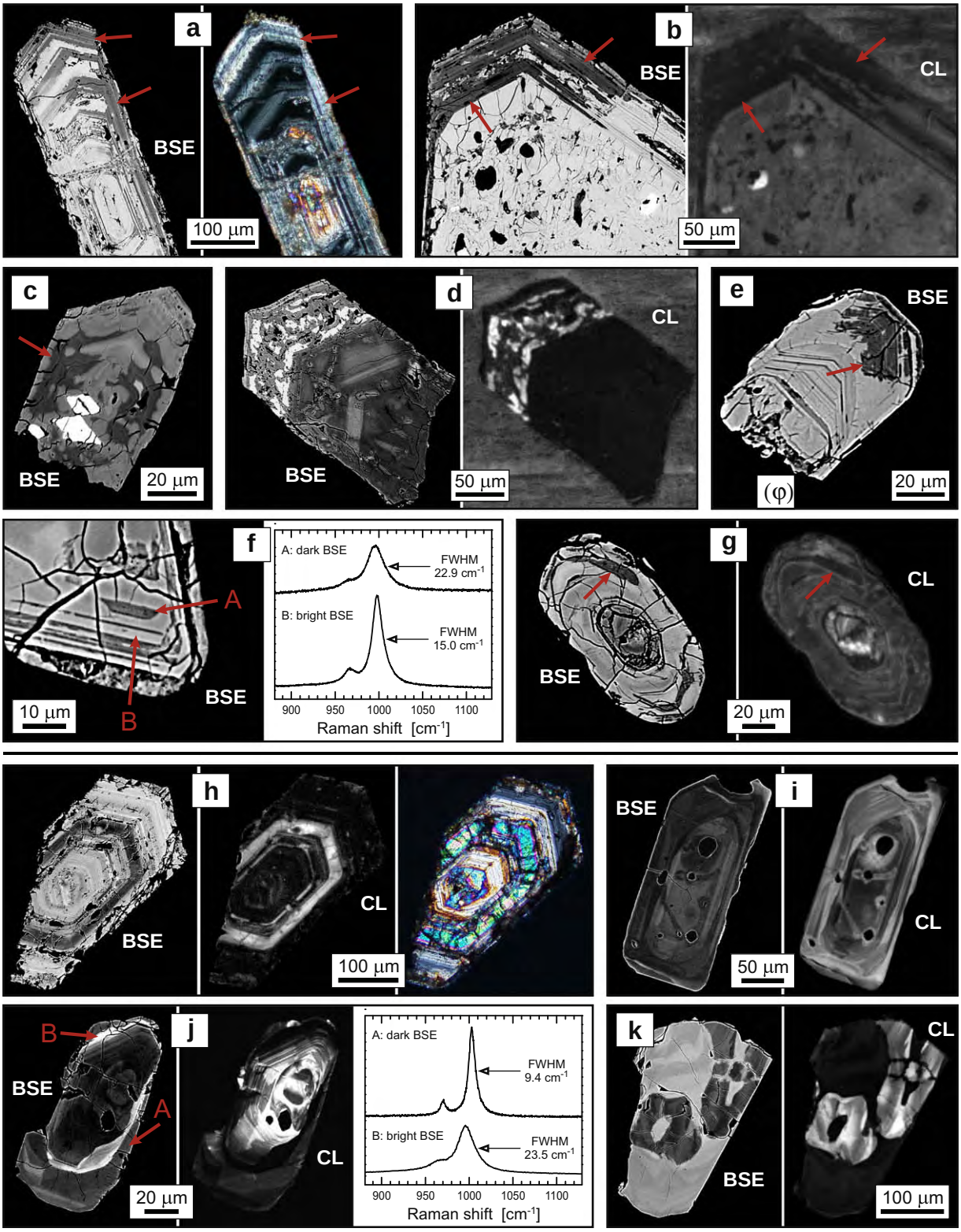

vations are explained by the consideration that the sample may have experienced local dewatering when analyzed regularly with a fully focused beam.

4.2. Pb isotope composition

In SHRIMP analyses of the Pb isotopic composition of zircon crystals from sample 87165 (La Pedriza) we found that bright-BSE areas are virtually free of non-radiogenic (i.e., common) Pb whereas porous, low-BSE areas contain significantly more common lead, with f206 values up to ~10% (Table 3, Fig. 3). This is consistent with previous observations that zircon virtually excludes Pb in primary magmatic or metamorphic growth. The majority of Pb in zircon is normally implanted, resulting from the decay of unstable parent nuclei in the U and Th chains. In contrast, common Pb is mostly in the ppb range (e.g., Krogh, 1993; Wiedenbeck et al., 1995). We determined common Pb concentrations of 100–250 ppm for porous, low-BSE areas in crystals from sample 87165 (Table 3).

Natural zircon with such high, and even higher, concentrations of common Pb have been studied before. All of these samples were found to be affected by secondary alteration processes (for instance, see Corfu, 1987; Mathieu et al., 2001) whereas, to the best of our knowledge, enhanced common Pb has never been observed in primary, unaltered zircon. From experiments to synthesize Pb-bearing zircon, Watson et al. (1997) concluded that P may charge-balance Pb^{2+} in zircon. This seems to be supported by our results, as enhanced common Pb is associated with high P concentrations (Table 3). However, variation of the P content in the La Pedriza zircon is rather moderate, in view of the extensive variations of common Pb, whereas the Ural samples did not contain notable quantities of common Pb (Willner et al., 2003) but occasional very high P (Table 1). This suggests that the presence of P (or, alternatively, H^+; Watson et al., 1997) can be associated with, but is not sufficient to allow for incorporation of Pb into zircon. Our results and previous results indicate that the enhanced occurrence of common Pb is limited to zircon affected by secondary, fluid-driven alteration. This is perhaps explained by the strong trend that more Pb is incorporated in a wet than a dry environment, and normally low abundances of Pb in natural environments from which primary zircon grows whereas altering fluids are likely to bring more Pb into the system. This effect is in addition probably inversely correlated with temperature (Watson et al., 1997).

4.3. The incorporation of hydrous species

To check our and previous assumptions that low-total zircon is hydrated, analysis of hydrous species was first done by EELS spectra obtained in the TEM. A shoulder near ~528 eV at the oxygen K-edge (Fig. 4a) is characteristic of OH/H_2O (Wirth, 1997), which points to hydration of samples. However, both the assignment to either hydroxyl or molecular water and the quantification of the hydrous species from the EELS band integral are still problematic (Wirth, 1997). Therefore we applied IR absorption spectroscopy as a complimentary technique. Due to the rather limited spatial resolution of IR when compared to EELS, infrared spectroscopy can only be used if samples show the phenomenon of deficient totals over relatively large areas (i.e., several tens of μm across). This is the case for some crystals from sample no. 87165 (Fig. 1d).

Spectra (Fig. 4b) show the intense, asymmetric O–H band without notable directional dependence that is typical of strongly radiation-damaged zircon (Caruba et al., 1985; Aines and Rossman, 1986; Nasdala et al., 2001b; Zhang et al., 2002). The assignment of this band, i.e., discriminating between either $(OH)^-$ groups or H_2O molecules, is still controversial. The integrated area of the O–H band (or more exactly, of the stretching fundamentals of hydroxyl groups and/or water molecules) in IR absorption spectra can be used to quantify the concentration of the hydrous species in unknown crystals. Using the equations of Libowitzky and Rossman (1996, 1997), remarkably uniform "water" concentrations in the range 5.0-6.8 wt% were determined for six La Pedriza zircon crystals. The accuracy of these IR-based "water" values, however, is tainted with uncertainty: Nasdala et al. (2001b) found that in the case of radiation-damaged zircon, "water" concentrations determined from IR band intensities may differ appreciably from those determined by thermogravimetry (weight loss on heating) and moisture evolution analysis. The above "water" concentrations are hence only considered to indicate "semi-quantitatively" that hydrous species in the wt% range are present.

Fig. 1. (overleaf) Compilation of images, photomicrographs, and Raman spectra (stacked) of zircon crystals yielding low totals (a–g) and "regular" zircon crystals (h–k). (a) BSE image and cross-polarized light photograph of a zoned zircon crystal from the Jack Hills granite. Low-total regions (red arrows) show higher birefringence. (b) BSE and CL image of a large zircon from the Jack Hills. Low-total areas are marked with arrows. (c) BSE image of a heterogeneous zircon crystal from the La Pedriza granite, Spain (cf. Pérez-Soba et al., 2007). Areas yielding low totals (arrow) are particularly lowly intense in BSE; large euhedral xenotime inclusions appear bright. (d) BSE and CL image of another zircon from the La Pedriza pluton with numerous xenotime inclusions. Low totals were measured in all areas of this zircon. (e) Zircon grain from a sandstone from the south-western Urals (cf. Willner et al., 2003) with a large alteration patch that yielded low totals (arrow). (f) BSE image and Raman spectra of another zircon from the SW Urals. Small patches yielding low totals (A) are darker in the BSE and more radiation damaged than the "regular" host (B). (g) BSE and CL image of a zircon grain from the SW Urals. Small interior regions yielding low totals (arrows) are low in BSE and CL. (h) BSE, CL, and cross-polarized light image of a zoned zircon crystal from the Jack Hills granite, Western Australia. The crystalline zone (bright interference colours) has the darkest BSE and bright CL. (i) BSE and CL image of a zircon grain from a monzonite in the Meissen massif, Germany. (j) BSE and CL image and two Raman spectra of a zircon grain from a charnockite-granite, Namaqualand, R.S.A. Areas that are bright in the BSE image (B) are strongly radiation-damaged whereas less damaged areas (A) are rather moderately damaged. (k) BSE and CL image of a zircon from the Adirondack Mountains, New York state. USA note that in all four cases (h–k) BSE and CL images show inverse intensities.

Table 1
Analytical results for zircon samples: BSE, electron microprobe data including calculated alpha doses, and Raman data.

Area/spot	No.[a]	BSE[b]	Electron microprobe results (wt%)																	α dose ($\times 10^{18}$/g)	FWHM[c] (cm^{-1})
			Al_2O_3	SiO_2	P_2O_5	CaO	FeO	Y_2O_3	ZrO_2	Tb_2O_3	Dy_2O_3	Ho_2O_3	Er_2O_3	Tm_2O_3	Yb_2O_3	Lu_2O_3	HfO_2	ThO_2	UO_2	Total		
Sample W64: Jack Hills. Western Australia (Archaean)																					
W64–10a	5	dk.	0.24	30.3	0.19	0.95	0.20	0.39	60.6	(bdl)	0.22	(bdl)	0.27	(bdl)	0.07	(bdl)	1.34	0.21	0.78	95.9	85	(>30)
W64–10b	5	reg.	0.19	31.9	0.12	0.76	0.25	0.38	62.5	(bdl)	0.05	(bdl)	0.20	(bdl)	0.07	(bdl)	1.31	0.31	0.92	99.1	102	(>30)
W64–6a	5	dk.	0.81	28.3	0.86	0.62	7.24	3.47	47.2	(bdl)	0.19	(bdl)	0.36	(bdl)	0.27	(bdl)	1.67	0.07	0.34	91.7	37	(>30)
W64–6b	4	reg.	0.13	32.0	0.10	0.82	0.35	0.36	62.3	(bdl)	0.05	(bdl)	0.19	(bdl)	0.08	(bdl)	1.73	0.08	0.87	99.2	92	(>30)
Samples 32 and 40: Southwest Urals (Riphean)																					
32–3–3a	2	dk.	0.52	25.9	1.93	0.57	0.51	2.53	62.6	0.07	0.43	(bdl)	0.20	(bdl)	0.21	0.07	1.31	0.03	0.15	97.0	11	22.5–25.0
32–3–3b	2	reg.	(bdl)	32.3	0.18	(bdl)	(bdl)	0.10	67.2	(bdl)	(bdl)	(bdl)	(bdl)	(bdl)	(bdl)	(bdl)	1.50	(bdl)	0.05	101.4	3.7	14.4–15.5
32–3–9a	6	dk.	0.60	28.4	2.44	0.64	0.51	2.41	58.8	0.05	0.42	(bdl)	0.23	(bdl)	0.25	(bdl)	1.63	0.03	0.14	96.6	10	24.0–27.5
32–3–9b	6	reg.	(bdl)	32.8	0.13	(bdl)	(bdl)	0.11	66.4	(bdl)	(bdl)	(bdl)	(bdl)	(bdl)	(bdl)	(bdl)	1.57	(bdl)	0.03	101.2	2.3	21.1–22.0
40–10–3a	2	dk.	0.83	30.0	1.30	0.42	0.56	1.73	59.5	(bdl)	0.28	0.11	0.15	(bdl)	0.17	(bdl)	1.15	0.17	0.14	96.6	8.7	26.9
40–10–3b	2	reg.	(bdl)	33.2	0.16	(bdl)	0.05	0.25	66.0	(bdl)	(bdl)	(bdl)	0.09	(bdl)	0.08	(bdl)	1.36	(bdl)	0.10	101.3	5.1	18.7
40–8–2a	3	dk.	0.56	30.0	0.82	0.36	0.36	1.38	60.6	(bdl)	0.21	(bdl)	0.15	(bdl)	0.15	(bdl)	1.28	0.15	0.15	96.2	9.0	22.2–24.0
40–8–2b	3	reg.	0.21	32.5	0.15	0.10	0.12	0.39	65.6	(bdl)	0.06	(bdl)	0.07	(bdl)	0.06	(bdl)	1.37	0.07	0.07	100.9	4.2	12.5–13.3
Sample 87165: La Pedriza. Spain (Hercynian)																					
87165–1a	3	dk.	0.75	27.3	1.54	1.43	1.03	2.19	54.4	(bdl)	0.29	(bdl)	0.27	(bdl)	0.51	0.09	2.22	0.27	1.72	94.1	16	(>30)
87165–1b	3	dk.	0.04	30.1	0.97	0.21	0.65	0.96	58.7	(bdl)	0.23	(bdl)	0.16	(bdl)	0.44	0.09	3.90	0.09	0.78	97.3	7.2	(>30)
87165–10a	3	dk.	0.49	27.4	1.96	1.19	0.50	2.52	56.0	(bdl)	0.34	(bdl)	0.36	(bdl)	0.58	0.11	2.07	0.35	1.80	95.7	17	(>30)
87165–10b	3	dk.	(bdl)	29.2	1.11	0.41	0.51	1.57	57.2	(bdl)	0.37	(bdl)	0.32	0.06	0.66	0.14	4.00	0.14	1.05	96.8	9.8	(>30)
Average detection limit[*]			0.04	0.08	0.06	0.03	0.06	0.09	0.13	0.04	0.04	0.10	0.05	0.06	0.06	0.06	0.04	0.03	0.03			

bdl = not detected, or average below the detection limit quoted in the bottom row.

[a] Number of single analyses per interior region.

[b] BSE: reg. = regular high intensity, med. = medium, dk. = dark (i.e., unusually low intensity).

[c] Full width at half maximum of the $\nu_3(SiO_4)$ Raman band of zircon.

[*] Average detection limit (wt% oxide, 2σ error by counting statistics of the background signal).

Table 2
Electron microprobe analyses of selected zircon samples including oxygen analysis.

Area/spot	Spot[a] (μm)	No.[b]	BSE[c]	Measured electron microprobe data (wt%)													Calculated values (wt%)[d]			
				O	Al	Si	P	Ca	Fe	Y	Zr	Yb	Hf	Th	U	Total	O equ.	O exc.	H_2O^*	Total
Sample W64: Jack Hills. Western Australia																				
W64–11a	2	3	reg.	35.6		0.11	15.0	0.04	0.71	0.38	0.35	45.0	0.11	1.63	0.09	1.02	100.1	34.0	1.6	1.8	100.3
W64–11a	15	3	reg.	35.4		0.04	15.0	0.03	0.44	0.28	0.21	45.8	0.07	1.77	0.04	0.56	99.7	34.0	1.5	1.6	99.9
W64–11b	2	3	dk.	35.1		0.39	13.3	0.39	0.46	3.73	2.96	34.5	0.27	1.68	0.25	0.31	93.3	30.6	4.5	5.0	93.9
W64–11b	15	3	dk.	38.1		0.55	13.1	0.43	0.46	3.15	3.31	34.0	0.33	1.57	0.19	0.42	95.6	30.3	7.8	8.8	96.6
Sample 87165: La Pedriza. Spain																				
87165–12a	2	2	dk.	36.5		0.31	13.1	0.62	0.94	0.36	1.82	40.2	0.48	1.87	0.24	1.60	98.0	31.7	4.8	5.4	98.6
87165–12b	2	2	reg.	36.9	(bdl)		13.7	0.61	0.22	0.33	1.58	40.8	0.54	3.50	0.18	0.96	99.3	32.1	4.8	5.3	99.9
Synthetic reference																				
$ZrSiO_4$	2	12	–	35.0	(bdl)		15.3	(bdl)	(bdl)	(bdl)	(bdl)	49.7	(bdl)	(bdl)	(bdl)	(bdl)	100.1	34.9	0.1	0.1	100.1
Average detection limit[*]				0.11		0.01	0.02	0.01	0.01	0.01	0.03	0.06	0.03	0.02	0.01	0.01					

bdl = not detected, or average below the detection limit quoted in the bottom row.
[a] Diameter of the electron beam focal spot.
[b] Number of single analyses.
[c] BSE: reg. = regular intensity, dk. = dark (i.e., unusually low intensity).
[d] O equ. = "equivalent" oxygen content calculated according to the content and valence of cations (Fe assumed to be Fe^{2+}, U assumed to be U^{4+}), O exc. = "excess" oxygen (measured O minus O equ.), H_2O^* = hypothetical water content calculated from O exc., Total = analytical sum assigning the excess oxygen to H_2O.
[*] Average detection limit (wt%, 2σ error by counting statistics of the background signal).

Hydrous species with concentrations of several wt%, or even higher, has, to the best of our knowledge, never been observed for unaltered zircon, which typically contains up to a few tenths of wt% H_2O (e.g., Woodhead et al., 1991; Nasdala et al., 2001b). Altered zircon, in contrast, is obviously able to store much higher amounts of water. Our IR spectra did not allow us to distinguish unambiguously between hydroxyl groups and water molecules. The near IR range above 4000 cm^{-1} (where potential combination modes involving OH and/or H_2O vibrations are expected) was difficult to interpret, perhaps due to the simultaneous detection of electronic absorption bands in this range (compare Nasdala et al., 2001b; Zhang et al., 2002). Even though there is no clear analytical evidence, we assign the "water" in altered, hydrous zircon to molecular H_2O, rather than to $(OH)^-$ groups, for two reasons. First, Mumpton and Roy (1961) found that analyses of hydrated zircon plot in the SiO_2–ZrO_2–H_2O triangle generally near the $ZrSiO_4$–H_2O line, but not along the $ZrSiO_4$–$Zr(OH)_4$ line (the latter should be the case if hydroxyl groups were the dominant hydrous species). Second, zircon analyses with "water" content as high as 14 wt% (Smith et al., 1991) and 16 wt% (Coleman and Erd, 1961) have been reported. If these amounts of "water" was present as hydroxyl groups, these zircon samples must have contained about 40 mol% $Zr(OH)_4$ (disregarding the presence of a hypothetical silicon hydrate). This is most unlikely and inconsistent with the other analytical values reported by above authors.

4.4. Structural state and sub-μm texture

To quantify the (theoretical) self-irradiation dose, time-integrated alpha fluences were calculated using the equation of Murakami et al. (1991). Calculated values (Table 1) are $>2 \times 10^{18}$ alpha events per gram, a value that is sufficient to cause significant damage of the crystal structure: Note that $\sim 10^{19}$ alpha-events per gram are sufficient to transform tetragonal $ZrSiO_4$ into an amorphous state (Zhang et al., 2000; Nasdala et al., 2002).

It is, however, well known that self-irradiation since the time of crystal growth on the one hand, and the presently observed degree of structural damage on the other hand, do not correlate in many cases (Meldrum et al., 1998; Nasdala et al., 2001a). This is due to that fact that the accumulation of structural radiation damage is strongly controlled by temperature and hence by the post-growth thermal history of the sample. To quantify the present radiation damage, Raman micro-spectroscopy was employed (Nasdala et al., 1995). For this, we evaluated the FWHM (full width at half maximum) of the internal $\nu_3(SiO_4)$ vibrational mode (Table 1). This parameter increases from <2 cm^{-1} for crystalline zircon to >30 cm^{-1} in the case of severely radiation-damaged zircon. Our samples are generally characterized by moderate to strong radiation damage (FWHMs generally >12 cm^{-1}; Table 1). Zircon crystals from samples W64 (Jack Hills) and 87165 (La Pedriza) yielded spectra in which the Raman signal of the remnant crystalline fraction was extremely broadened (estimated FWHM >30 cm^{-1}); reliable band fitting was impossible due to very low band intensities in these cases. Such extensive Raman band broadening points to elevated radiation damage, with amorphous fractions well above 90 vol% (Nasdala et al., 2003). Strong radiation damage is also indicated by the very low birefringence of these samples (Holland and Gottfried, 1955; note the grey interference colours in Fig. 1a) and the strong broadening and virtual lack of any orientational dependence of O–H bands in the IR spectra (Fig. 4b). In spite of generally high degrees of present damage, most

Table 3
Chemical analyses of zircon crystals from La Pedriza (sample 87165) including Pb isotope analysis.

Area/ spot	BSE[a]	Electron microprobe results (wt%):																		SHRIMP results:				
	No.[b]	MgO	Al_2O_3	SiO_2	P_2O_5	CaO	MnO	FeO	Y_2O_3	ZrO_2	Dy_2O_3	Ho_2O_3	Er_2O_3	Tm_2O_3	Yb_2O_3	Lu_2O_3	HfO_2	ThO_2	UO_2	Total	Pb_{tot} (ppm)	Pb_{com} (ppm)	f 206^c	U (wt%)	Th (wt%)
87165–3a	dk.	4	0.15	(bdl)	28.3	1.43	1.26	0.19	1.29	2.02	56.0	0.26	(bdl)	0.23	(bdl)	0.46	0.11	1.84	0.25	1.24	95.0	893	248	9.76	1.30	0.20
87165–3b	reg.	1	(bdl)	(bdl)	31.1	1.74	(bdl)	(bdl)	(bdl)	2.08	61.9	0.17	(bdl)	0.32	(bdl)	0.50	0.11	1.95	0.14	0.94	101.0	836	1	0.02	1.46	0.25
87165–3c	reg.	1	(bdl)	(bdl)	31.0	1.81	(bdl)	(bdl)	(bdl)	2.39	61.2	0.21	(bdl)	0.27	(bdl)	0.53	0.15	1.86	0.27	1.32	101.2	834	0	0.00	1.52	0.27
87165–7a	dk.	4	0.20	0.11	28.2	1.25	1.14	0.32	1.22	1.74	55.6	0.28	(bdl)	0.22	(bdl)	0.52	0.11	2.57	0.21	1.77	95.5	820	213	8.97	1.34	0.20
87165–7b	dk.	3	0.11	(bdl)	28.4	1.45	1.09	0.28	1.00	1.72	56.6	0.23	(bdl)	0.22	(bdl)	0.46	0.10	2.20	0.21	1.36	95.4	476	103	7.18	1.04	0.36
87165–9a	dk.	2	0.17	(bdl)	29.1	0.95	0.72	0.15	1.34	1.60	57.6	0.18	(bdl)	0.13	(bdl)	0.34	0.08	1.71	0.29	1.26	95.7	807	132	5.22	1.21	0.23
87165–9b	reg.	1	(bdl)	(bdl)	32.9	(bdl)	(bdl)	(bdl)	0.06	0.29	65.8	(bdl)	(bdl)	0.05	(bdl)	(bdl)	0.09	1.56	0.03	0.11	100.9	40	1	0.80	0.08	0.04
Av. detection limit*:			0.04	0.04	0.07	0.06	0.04	0.03	0.06	0.09	0.13	0.04	0.10	0.05	0.06	0.06	0.06	0.04	0.03	0.03						

bdl = not detected, or average below the detection limit quoted in the bottom row.
Pb_{tot} = total Pb, Pb_{com} = common (i.e., non-radiogenic) Pb.
[a] BSE: reg. = regular intensity, dk. = dark (i.e., unusually low intensity).
[b] Number of single electron microprobe analyses per interior region.
[c] f206 = common 206Pb/total ^{206}Pb, calculated from the observed ^{204}Pb.
* Average electron microprobe detection limit (wt% oxide, 2σ error by counting statistics of the background signal).

samples are still notably less metamict than would be expected from their calculated self-irradiation doses. For instance, Jack Hills and La Pedriza zircon crystals should be fully amorphous if all of the predicted radiation damage was present (see very high alpha doses in Table 1); this was not observed. This observation points to a recrystallization or thermal annealing event in the post-growth history of samples.

Elevated levels of metamictization, but not complete amorphization, was also observed in the TEM. Electron diffraction patterns of all samples appeared at least somewhat blurred, in some cases even with a polycrystalline appearance (Fig. 5a), which also points to a secondary recrystallization process. More importantly, bright field and HAADF images of zircon samples showed a spongy texture, with numerous pores being several hundred nanometres or smaller in size (Figs. 5b and c). This sub-μm-scale texture corresponds to what had already been proposed by Pointer et al. (1988b), namely, the occurrence of a significant volume fraction of sub-μm-sized voids in low-total zircon.

It is well known that in the electron microprobe analysis of porous materials, in comparison to fully dense analogs, there is always a significant deficit of emitted X-rays. This deficit leads to apparent deficiencies of analysis sums when routine EPMA correction procedures are employed (Lakis et al., 1992). Tretyakov et al. (1998) assigned the X-ray emission deficit to charge trapping effects caused by the insulating character of the material. Sorbier et al. (2000) found that porous, in contrast to dense Al_2O_3 yielded deficient analytical totals, and assigned this to a combination of charge trapping and geometrical effects of the porosity. Sorbier et al. (2004) proposed that surface roughness and energy loss at interfaces inside porous samples may also contribute to the analytical shortfall. The porosity of our samples is therefore interpreted as the main cause of the observed analytical shortfall. In addition, the numerous pores are considered to be perfect candidates for the incorporation of water. We have discussed above that the high water contents of several wt% of the low-total zircon, calculated indirectly from oxygen measurements (Table 2) and estimated from IR absorption intensities, contribute also to the analytical shortfall of these zircon crystals.

5. UNUSUALLY LOW BSE OF THE LOW-TOTAL ZIRCON

It is well known (e.g., see Corfu et al., 2003; and references therein) that most natural zircon crystals are characterized by inversely correlated BSE and CL intensities, i.e., micro-areas that are brightest in BSE are normally particularly low in CL, and vice versa. Four examples of the "normal" inverse behaviour of BSE and CL in zircon are shown in Fig. 1h–k. Note that micro-areas with elevated levels of accumulated self-irradiation damage, which can easily be recognized from their lowered interference colours (Fig. 1h) or broadening of vibrational bands (Fig. 1j), always yield enhanced BSE intensity and lowered CL when compared to neighbouring, less radiation-damaged areas.

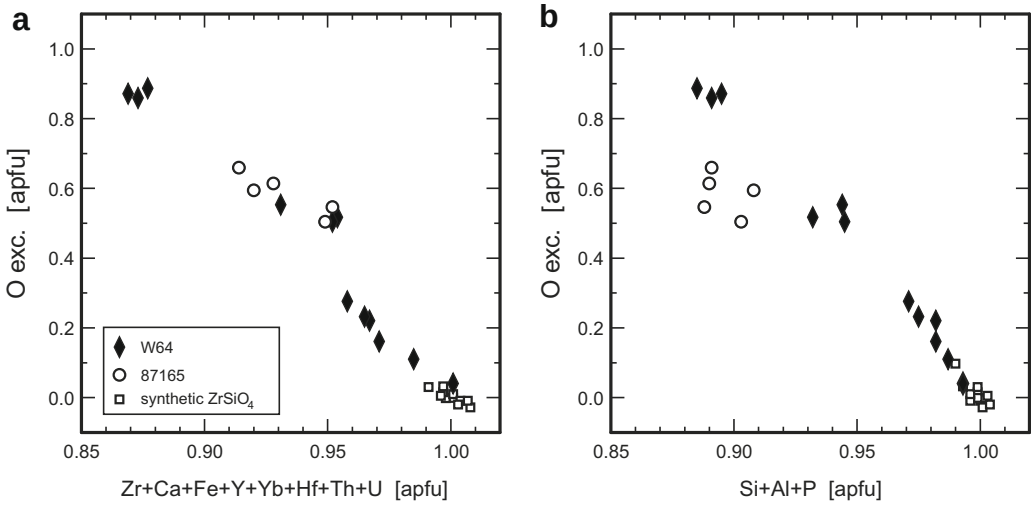

Fig. 2. Excess oxygen (difference between measured *O*, and calculated *O* equivalent to contents and valences of cations), plotted versus sums of intermediately sized (a) and small (b) cations per formula unit (cf. data presented in Table 2). Excess oxygen, which is mainly assigned to the incorporation of water, correlates inversely with cation deficiencies.

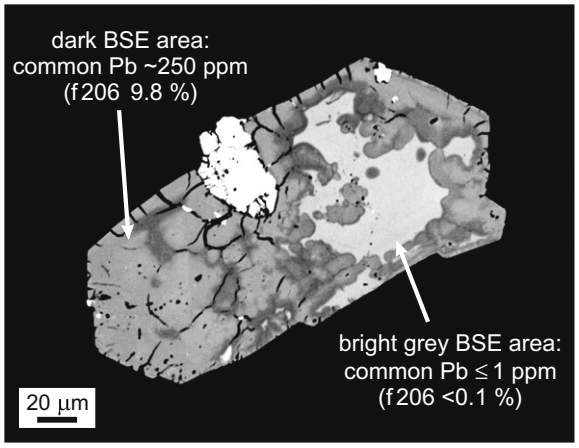

Fig. 3. Heavily altered, generally U-rich zircon grain from La Pedriza (crystal 87165–3; BSE image) with large xenotime inclusion (bright). Note that altered, micro-porous areas (dark grey BSE) are enriched in common Pb whereas the bright gray BSE area (centre) is virtually free of non-radiogenic lead (f206 = common ^{206}Pb/total ^{206}Pb, calculated from the observed ^{204}Pb).

The inverse behaviour of BSE and CL is explained by the consideration that chemical variations (i.e., $\bar{Z}$ contrast; Hall and Lloyd, 1981) have only minor effects on the BSE of regular zircon (Nasdala et al., 2006) whereas both BSE and CL of zircon are strongly affected by radiation damage. The CL decreases upon self-irradiation of zircon (for instance caused by the enhancement of non-radiative transitions in the disturbed electronic band structure) and can easily be recovered through annealing (Nasdala et al., 2002). The BSE intensity, in contrast, increases upon damage accumulation. Structural disorder results in an increase of the fraction of back-scattered electrons and their remnant energy, which is commonly referred to as electron channelling contrast (see for instance Mitchell and Day,

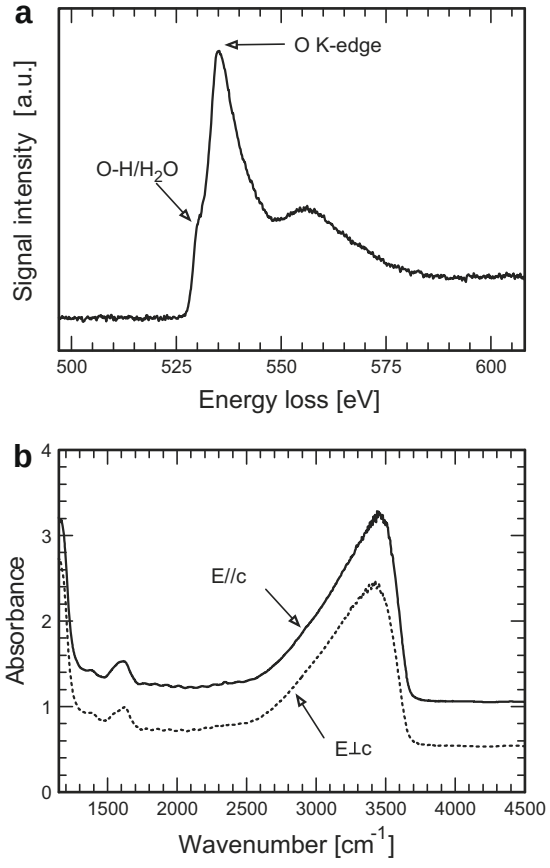

Fig. 4. (a) Electron energy loss spectrum of a low-total area in a zircon from the Jack Hills, Western Australia. The oxygen K edge shows a shoulder at ~529 eV, which indicates the presence (of rather moderate amounts) of hydroxyl or water (compare Wirth, 1997). (b) Oriented IR absorption spectra of a low-total zircon from the La Pedriza pluton, Spain, show large amounts (estimated 6.6 wt%) of hydrous species. Spectra are shown with vertical offset for more clarity.

1998). The strong correlation of zircon BSE intensity with the degree of accumulated radiation damage, without notable $\bar{Z}$ contrast, has been demonstrated in an annealing study (Nasdala et al., 2006). The efficiency of structural damage in increasing the back-scattering of electrons was recently reconfirmed by ion implantation experiments (Nasdala et al., 2007).

Zircon crystals affected by the phenomenon of low totals, however, generally deviate from the "normal" inverse correlation of BSE and CL intensities (see pairs of images in Figs. 1b and g; see also Kempe et al., 2000). Deficient electron microprobe totals were obtained in micro-areas that showed very low BSE *and* CL intensity. Low-total zircon areas are virtually non-luminescent. In some CL images these areas appear even darker than the surrounding, lowly luminescent araldite epoxy (see Figs. 1b and d). Their generally low CL intensities are explained by (i) moderate to strong levels of radiation damage (compare Nasdala et al., 2002) and (ii) the presence of notable quantities of hydrous species in the low-total areas, which is known to lower the CL emission of solids (e.g., Gutzov and Peneva, 1995). In contrast, observed very low BSE intensity of low-total areas appear to be in apparent contrast to the moderate to strong radiation damage of these areas (compare Raman FWHMs in Table 1). See, for instance, zircon #40-8-2 (Fig. 1f): Even though the low-total area (marked "A") is significantly more radiation damaged than the unaltered host zircon, which should normally have resulted in brighter BSE, the BSE of this area is much lower than that of the surrounding zircon (marked "B" in Fig. 1f).

The low BSE intensity of low-total areas is first assigned to $\bar{Z}$ contrast (Hall and Lloyd, 1981; see also Smith et al., 1991; Geisler et al., 2003b): Our samples show much stronger chemical variations and hence stronger $\bar{Z}$ variations than "regular" zircon. However, the BSE of the low-total areas was often described as "anomalously" low (see Kempe et al., 2000; and references therein). Pointer et al. (1988b) argued that the BSE of low-total areas in zircon crystals from Ririwai, Nigeria, was much too dark to be explained by their chemical composition alone. These authors explained the dark BSE by the presence of sub-microscopic voids. They argued that because large voids and textural holes appear dark in BSE images, numerous small voids in surficial regions of an imaged sample are also likely to lower the detected BSE. Our results therefore suggest that the very low BSE of the low-total zircon is due to a combination of reasons, involving chemical composition (i.e., lower $\bar{Z}$) and textural features (i.e., porosity).

These effects on zircon BSE also allow us to understand the non-uniform appearance of electron microprobe spots

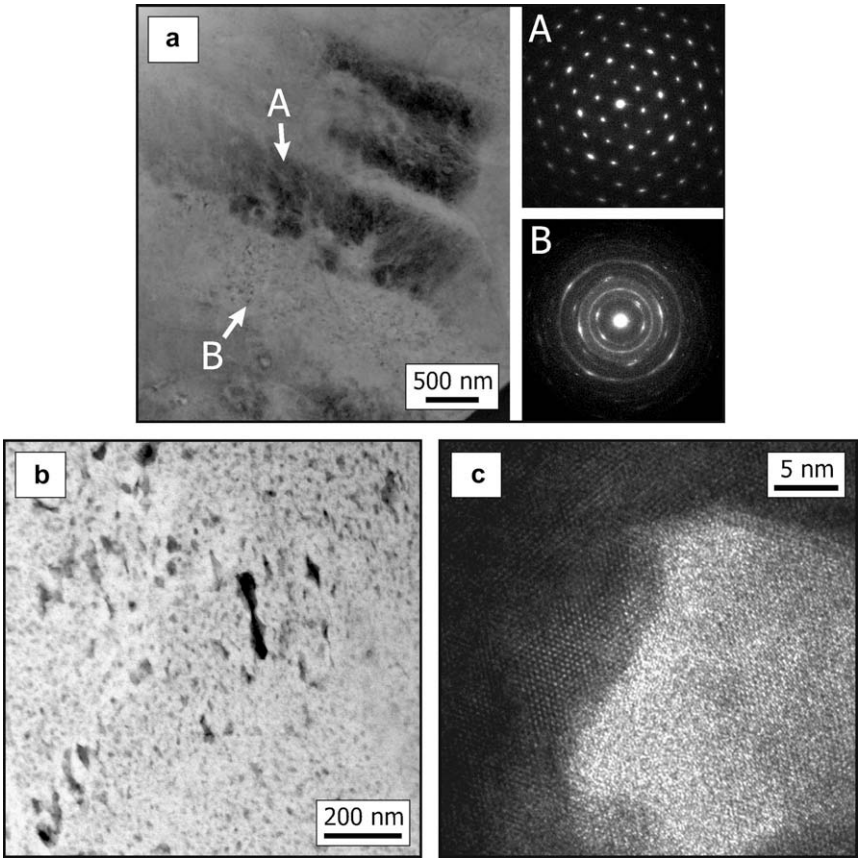

Fig. 5. Transmission electron microscopy images of low-total interior regions. (a) Bright field image of a zircon from the Jack Hills, with two corresponding electron diffraction patterns. Two darker areas (A) are moderately distorted single-crystals, which are embedded in a brighter, polycrystalline (crystal size in the nanometer-range) matrix with pronounced porous texture (B). (b) HAADF image obtained from a detrital zircon from the SW Urals, showing numerous sub-micrometer sized pores. (c) HREM image of one pore.

in BSE images. In the case of "regular" zircon, electron microprobe analysis points are normally visible as slightly darkened spots in BSE images. This is explained by the enhanced electron back-scattering of radiation-damaged solids and the fact that the energy impact of the electron beam during the analysis causes partial structural recovery (Nasdala et al., 2003). In BSE images of low-total zircon, in contrast, microprobe spots are notably brighter than their surrounding area (for instance, see Fig. 2c in Smith et al, 1991). This may perhaps be assigned to dewatering ($\bar{Z}$ increase) resulting from the electron microprobe analysis.

6. FORMATION OF LOW-TOTAL ZIRCON BY FLUID-DRIVEN ALTERATION

All samples showed the phenomenon of deficient analytical totals in interior regions that are interpreted as being affected by secondary alteration. Our assignment is based on the textural position of low-total areas (see areas marked with red arrows in Figs. 1a–g) and the results of chemical analyses (Tables 1–3). Also, low-total areas contain inclusions of minerals that are typically formed during zircon alteration. For instance, large xenotime inclusions in the La Pedriza zircon (Fig. 1c and d) might be an alteration product, although Pérez-Soba et al. (2007) interpreted them as co-crystallised with zircon in a late-magmatic environment. Low-total areas are enriched in (predominantly light) non-formula elements (such as P, Al, Y, Fe; also Ca, Yb, somme of the REEs; Tables 1–3) that are typically incorporated in secondary alteration processes rather than during primary zircon growth (e.g., Geisler et al., 2003a; see Table 1). This may either be due to elevated incorporation of non-formula elements into zircon in a low-temperature, hydrothermal overprint, or the presence of unrecognised, sub-micron sized additional phases. The latter is perhaps indicated by correlating Y and P concentrations in sample 87165 (pointing to xenotime inclusions; Tables 1–3) and the unusually high Fe content of area W64-6a (pointing to a Fe-phase; Table 1).

All of our observations seem to concur very well with previous observations, as low totals were always reported from altered zircon (e.g., Pointer et al., 1988b; Smith et al., 1991). Irber et al. (1997) and Pérez-Soba et al. (2007) stated that zircon samples yielding deficient analytical totals are typically characterized by non-stoichiometric composition. These authors interpreted this as the result of secondary alteration that was likely accompanied by hydration. In contrast, the phenomenon of deficient analytical totals has, to the best of our knowledge, never been observed in primary, unaltered zircon. The conclusion that the formation of low-total zircon must be related to a secondary, fluid-driven alteration process is further supported by the observation of deficient microprobe totals after the experimental hydrothermal alteration of zircon (Geisler et al, 2003b).

All of the low-total areas found in the present study appeared porous at high magnification, which is an indicator of a fluid-driven replacement reaction (compare Putnis, 2002; Putnis et al., 2007) rather than a diffusional alteration process. This assignment is also supported by the observation of sharp boundaries between unaltered and altered areas (Fig. 1e–g), which mark the locations where the chemical alteration along a slowly progressing reaction front had stopped. In contrast, a diffusive ion exchange process should have resulted in rather diffuse boundaries of alteration patches. However, no fluid inclusions were found under the optical microscope. Putnis (2002) stated that even if a mineral phase with a higher molar volume than that of its starting material is formed in a fluid-driven replacement reaction, the newly formed phase is always porous. An example is the replacement of leucite by analcime (with the latter having a larger molar volume; Putnis et al., 2007). This indicates that such replacement processes are likely to have a negative mass balance, i.e., there is some loss of material taken away by the transporting fluid. In our case, radiation-damaged (and hence volume expanded; Holland and Gottfried, 1955) zircon is replaced by newly formed and thus non-expanded zircon. It is likely that the somewhat negative mass balance of the replacement reaction, along with the smaller volume of the newly formed zircon, results in a particularly clear volume decrease. This finally results in the formation of a texture with particularly high porosity.

The numerous pores perfectly support the incorporation of water. This could either already occur during the replacement reaction; the ingression of the transporting fluid might then result in a slow-down of the reaction. Water incorporation could also have occurred at a significantly later stage, after self-irradiation and heterogeneous expansion has taken place again.

7. CONCLUSIONS

Deficient analytical totals of zircon were always found in altered samples that show extensive porosity. Numerous sub-μm-sized voids in the analyzed material affect the EMPA analyses, for instance by increasing the penetration of the primary electron beam into the sample, increasing the absorption of generated X-ray quanta, and charging effects. In addition, water seems to have a significant additional effect. In contrast to primary, un-altered zircon, porous altered zircon formed in a fluid-driven replacement reaction may be virtually "wet", with water concentrations well in the wt% range. This water obviously contributes to the significant analytical shortfall for two reasons. First, hydrous zircon is likely to dehydrate and disintegrate under the electron beam. Second, water remains mainly non-analyzed in the electron microprobe. The latter is potentially true for other elements non-analyzed in the electron microprobe, such as Li and F.

The very low BSE intensity of the low-total zircon is closely related to the analytical shortfall; it is assigned to a combination of textural effects and chemical composition. First, the presence of numerous sub-micrometer sized voids (Fig. 5; note that not necessarily all of them are being "filled" with water) lowers the electron back-scattering. Second, the incorporation of light elemental species (especially hydrous species, P, and Fe) on the order of several wt% results in a clear $\bar{Z}$ decrease.

The formation of low-total zircon (and most probably also of other actinide-bearing, accessory minerals yielding deficient totals) is related to the metamictization process. However, low totals cannot solely be assigned to radiation damage alone. Accumulation of self-irradiation damage does not result in low totals; even heavily damaged (i.e., nearly amorphized) but unaltered zircon yielded "normal" analytical totals close to 100 wt% (e.g., Murakami et al., 1991; Zhang et al., 2000; Nasdala et al., 2002). The formation of zircon yielding deficient totals and very low BSE requires alteration of previously radiation-damaged zircon in a fluid-driven replacement reaction that results in volume loss and thus the formation of a spongy, perhaps hydrated material, and subsequent hydration. The observation of deficient electron microprobe totals, accompanied by very low BSE intensities resulting in a deviation from the regular inverse correlation of BSE and CL, in unknown zircon crystals may therefore be considered an indicator for a secondary alteration history.

ACKNOWLEDGMENTS

We are most grateful to J.M. Hanchar for providing synthetic zircon, hafnon, thorite, and uranium oxide crystals as electron microprobe reference materials. Natural zircon samples were kindly made available by J. M. Hanchar, A. Möller, R.T. Pidgeon, and T. Wenzel. Thanks are due to A. Wagner, D. Dettmar, and K. Paech for sample preparation, and to A. Beran and E. Libowitzky for experimental assistance. Constructive reviews by M. Williams, J.M. Hanchar, and an anonymous expert, and comments by handling editor Y. Amelin, are gratefully acknowledged. Partial funding for this research was provided by the European Commission trough contract no. MEXC-CT-2005-024878 and by the Austrian Science Fund (FWF) through grant P20028-N10.

REFERENCES

Aines R. D. and Rossman G. R. (1986) Relationships between radiation damage and trace water in zircon, quartz, and topaz. *Am. Mineral.* **71**, 1186–1193.

Armstrong, J. T., 1988. Accurate quantitative analysis of oxygen and nitrogen with a W/Si multilayer crystal. In *Microbeam Analysis* (ed. D.E. Newbury). pp. 301–304.

Armstrong J. T. (1991) Quantitative elemental analysis of individual microparticles with electron beam instruments. In *Electron Probe Quantitation* (eds. K. F. J. Heinrich and D. E. Newbury). Plenum Press, New York, London, pp. 261–315.

Armstrong J. T. (1995) CITZAF: a package of correction programs for the quantitative electron microbeam X-ray analysis of thick polished materials, thin films, and particles. *Microbeam Anal.* **4**, 177–200.

Breiter, K., Förster, H. -J., Škoda, R., 2006. Extreme P-, Bi-, Nb-, Sc-, U- and F-rich zircon from fractionated perphosphorous granites: the peraluminous Podlesí granite system. Czech Republic. *Lithos* **88**, 15–34.

Caruba R., Baumer A., Ganteaume M. and Iacconi P. (1985) An experimental study of hydroxyl groups and water in synthetic and natural zircons: a model of the metamict state. *Am. Mineral.* **70**, 1224–1231.

Coleman R. G. and Erd R. C. (1961) Hydrozircon from the Wind River formation, Wyoming. *J. Res. U.S. Geol. Surv.* **256**, 297–300.

Corfu F. (1987) Inverse age stratification in the archaean crust of the superior province: Evidence for infra- and subcrustal accretion from high resolution U-Pb zircon and monazite ages. *Precambrian Res.* **36**, 259–275.

Corfu, F., Hanchar, J. M., Hoskin, P. W. O., Kinny, P., 2003. Atlas of zircon textures. In *Zircon* (eds. J.M. Hanchar and P.W.O Hoskin). *Rev. Mineral. Geochem. 53, Mineral. Soc. Am.*, Washington, DC., pp. 469–500.

De Laeter J. R. and Kennedy A. K. (1998) A double focussing mass spectrometer for geochronology. *Int. J. Mass Spectrom. Ion Process* **178**, 43–50.

Förster H.-J. (1998) The chemical composition of REE-Y-Th-U-rich accessory minerals in peraluminous granites of the Erzgebirge-Fichtelgebirge region, Germany, Part I: The monazite-(Ce)-brabantite solid solution series. *Am. Mineral.* **83**, 259–272.

Geisler T., Rashwan A. A., Rahn M. K. W., Poller U., Zwingmann H., Pidgeon R. T., Schleicher H. and Tomaschek F. (2003a) Low-temperature hydrothermal alteration of natural metamict zircon from the Eastern Desert, Egypt. *Mineral. Mag.* **67**, 485–508.

Geisler T., Schleicher H., Kurtz R., van Bronswijk W. and Schleicher H. (2003b) Experimental hydrothermal alteration of partially metamict zircon. *Am. Mineral.* **88**, 1496–1513.

Gutzov S. and Peneva S. K. (1995) Structure and properties of hydrous zirconium oxide. *Bulgarian Chem. Commun.* **28**, 744–751.

Hall M. G. and Lloyd G. E. (1981) The SEM examination of geological samples with a semiconductor back-scattered electron detector. *Am. Mineral.* **66**, 362–368.

Holland H. D. and Gottfried D. (1955) The effect of nuclear radiation on the structure of zircon. *Acta Cryst.* **8**, 291–300.

Irber W., Förster H. J., Hecht L., Möller P. and Morteani G. (1997) Experimental, geochemical, mineralogical and O-isotope constraints on the late-magmatic history of the Fichtelgebirge granites (Germany). *Geol. Rundsch.* **86**(Suppl.), S110–S124.

Johan Z. and Johan V. (2005) Accessory minerals of the Cínovec (Zinnwald) granite cupola, Czech Republic: indicators of petrogenetic evolution. *Mineral Petrol* **83**, 113–150.

Kempe U., Gruner T., Nasdala L. and Wolf D. (2000) Relevance of cathodoluminescence for the interpretation of U-Pb zircon ages, with an example of an application to a study of zircons from the Saxonian Granulite Complex, Germany. In *Cathodoluminescence in Geosciences* (eds. M. Pagel, V. Barbin, P. Blanc and D. Ohnenstetter). Springer, Berlin, Heidelberg, New York, pp. 415–455.

Krogh T. E. (1993) High precision U-Pb ages for granulite metamorphism and deformation in the Archean Kapuskasing structural zone, Ontario: implications for structure and development of the lower crust. *Earth Plan. Sci. Lett.* **119**, 1–18.

Lakis, R., Lyman, C., Goldstein, J., 1992. Electron-probe microanalysis of porous materials. In *50th Ann. Meeting of the Electron Microscopy Society of America Proceedings*, pp. 1660–1661.

Libowitzky E. and Rossman G. R. (1996) Principles of quantitative absorbance measurements in anisotropic crystals. *Phys. Chem. Minerals* **23**, 319–327.

Libowitzky E. and Rossman G. R. (1997) An IR absorption calibration for water in minerals. *Am. Mineral.* **82**, 1111–1115.

Mathieu R., Zetterström L., Cuney M., Gauthier-Lafaye F. and Hidaka H. (2001) Alteration of monazite and zircon and lead migration as geochemical tracers of fluid paleocirculations around the Oklo–Okélobondo and Bangombé natural nuclear reaction zones (Franceville basin, Gabon). *Chem. Geol.* **171**, 147–171.

McLelland J., Morrison J., Selleck B., Cunningham B., Olson C. and Schmidt K. (2001) Hydrothermal alteration of late- to post-tectonic Lyon Mountain granitic gneiss, Adirondack Highlands, New York: origin of quartz-sillimanite segregations, quartz-albite lithologies, and associated Kiruna-type low-Ti Fe-oxide deposits. *J. Metamorph. Geol.* **19**, 1–19.

Medenbach, O., 1976. Geochemie der Elemente in Zirkon und ihre räumliche Verteilung. – Eine Untersuchung mit der EMS. Doctoral thesis, Univ. Heidelberg.

Meldrum A., Boatner L. A., Weber W. J. and Ewing R. C. (1998) Radiation damage in zircon and monazite. *Geochim. Cosmochim. Acta.* **62**, 2509–2520.

Mitchell D. R. G. and Day R. A. (1998) Electron channelling contrast imaging of defect structures in neutron irradiated aluminium. *Scripta Mater.* **39**, 923–930.

Mumpton F. A. and Roy R. (1961) Hydrothermal stability studies of the zircon-thorite group. *Geochim. Cosmochim. Acta* **21**, 217–238.

Murakami T., Chakoumakos B. C., Ewing R. C., Lumpkin G. R. and Weber W. J. (1991) Alpha-decay event damage in zircon. *Am. Mineral.* **76**, 1510–1532.

Nasdala L., Irmer G. and Wolf D. (1995) The degree of metamictization in zircon: a Raman spectroscopic study. *Eur. J. Mineral.* **7**, 471–478.

Nasdala L., Wenzel T., Pidgeon R. T. and Kronz A. (1999) Internal structures and dating of complex zircons from Meissen Massif monzonites, Saxony. *Chem. Geol.* **156**, 331–341.

Nasdala L., Wenzel M., Vavra G., Irmer G., Wenzel T. and Kober B. (2001a) Metamictisation of natural zircon: accumulation versus thermal annealing of radioactivity-induced damage. *Contrib. Mineral. Petrol.* **141**, 125–144.

Nasdala L., Beran A., Libowitzky E. and Wolf D. (2001b) The incorporation of hydroxyl groups and molecular water in natural zircon ($ZrSiO_4$). *Am. J. Sci.* **301**, 831–857.

Nasdala L., Lengauer C. L., Hanchar J. M., Kronz A., Wirth R., Blanc P., Kennedy A. K. and Seydoux-Guillaume A.-M. (2002) Annealing radiation damage and the recovery of cathodoluminescence. *Chem. Geol.* **191**, 121–140.

Nasdala, L., Zhang, M., Kempe, U., Panczer, G., Gaft, M., Andrut, M., and Plötze, M., 2003. Spectroscopic methods applied to zircon. In *Zircon* (eds. J.M. Hanchar and P.W.O Hoskin). *Rev. Mineral. Geochem. 53, Mineral. Soc. Am.*, Washington, DC., pp. 427–467.

Nasdala L., Kronz A., Hanchar J. M., Tichomirowa M., Davis D. D. and Hofmeister W. (2006) Effects of natural radiation damage on back-scattered electron images of single-crystals of minerals. *Am. Mineral.* **91**, 1738–1746.

Nasdala L., Grambole D., Kronz A. and Trullenque G. (2007) Effects of irradiation damage on the back-scattering of electrons: silicon-implanted silicon. *Am. Mineral.* **92**, 1768–1771.

Pérez-Soba, C., 1992. Petrología y geoquímica del macizo granítico de La Pedriza, Sistema Central Español. Ph.D. thesis, Univ. Complutense, Madrid.

Pérez-Soba C., Villaseca C., Gonzáles del Tánago J. and Nasdala L. (2007) The composition of zircon in the peraluminous Hercynian granites of the Spanish Central System batholith. *Can. Mineral.* **45**, 509–527.

Peterman Z. E., Zartman R. E. and Sims P. K. (1986) A protracted Archean history in the Watersmeet gneiss dome, northern Michigan. *U.S. Geol. Surv. Bull.* **1622**, 51–64.

Pidgeon R. T. (1992) Recrystallization of oscillatory zoned zircon: some geochronological and petrological implications. *Contrib. Mineral. Petrol.* **110**, 463–472.

Pidgeon R. T. and Wilde S. A. (1998) The interpretation of complex zircon U-Pb systems in Archaean granitoids and gneisses from the Jack Hills, Narryer Gneiss Terrane, Western Australia. *Precambrian Res.* **91**, 309–332.

Pidgeon, R. T., Furfaro, D., Kennedy, A. K., Nemchin, A. A., van Bronswjk, W., 1994. Calibration of zircon standards for the Curtin SHRIMP II. In *Eighth Intl. Conf. on Geochronology, Cosmochronology and Isotope Geology, Berkeley, USA, Abstracts Volume. U.S. Geol. Surv. Circ.* 1107, p. 251.

Pointer C. M., Ashworth J. R. and Ixer R. A. (1988a) The zircon-thorite mineral group in metasomatized granite, Ririwai, Nigeria. 1. Geochemistry and metastable solid solution of thorite and coffinite. *Mineral. Petrol.* **38**, 245–262.

Pointer C. M., Ashworth J. R. and Ixer R. A. (1988b) The zircon-thorite mineral group in metasomatized granite, Ririwai, Nigeria. 2. Zoning, alteration and exsolution in zircon. *Mineral. Petrol.* **39**, 21–37.

Putnis A. (2002) Mineral replacement reactions: from macroscopic observations to microscopic mechanisms. *Mineral. Mag.* **66**, 689–708.

Putnis C., Geisler T., Schmid-Beurmann P., Stephan T. and Giampaolo C. (2007) An experimental study of the replacement of leucite by analcime. *Am. Mineral.* **92**, 19–26.

Robb L. J., Armstrong R. A. and Waters D. J. (1999) The history of granulite-facies metamorphism and crustal growth from single zircon U-Pb geochronology: Namaqualand, South Africa. *J. Petrol.* **40**, 1747–1770.

Rubin J. N., Henry C. D. and Price J. G. (1989) Hydrothermal zircons and zircon overgrowths, Sierra Blanca Peaks, Texas. *Am. Mineral.* **74**, 865–869.

Rybka R. and Wolf R. C. (1995) Application of layered synthetic microstructure crystals to WDX microanalysis of ultra-light elements. In *X-ray Spectrometry in Electron Beam Instruments* (eds. D. Wiliams, J. Goldstein and D. E. J. Newbury). Plenum Press, New York, London, pp. 287–303.

Smith D. G. W., de St. Jorre L., Reed S. J. B. and Long J. V. P. (1991) Zonally metamictized and other zircons from Thor Lake, Northwest Territories. *Can. Mineral.* **29**, 301–309.

Sorbier L., Rosenberg E., Merlet C. and Llovet X. (2000) EPMA of porous media: a Monte Carlo approach. *Microchim. Acta* **132**, 198–199.

Sorbier L., Rosenberg E. and Merlet C. (2004) Microanalysis of porous materials. *Microscopy and Microanalysis* **10**, 745–752.

Speer, J. A., 1982. Zircon. In *Orthosilicates*, (ed. P.H. Ribbe). Rev. Mineral. 5, Mineral. Soc. Am., Washington, D.C., pp. 67–112.

Törnroos R. (1985) Metamict zircon from Mozambique. *Bull. Geol. Soc. Finland* **57**, 181–195.

Tretyakov V. V., Romanov S. G., Fokin A. V. and Alperovich V. I. (1998) EPMA of the composition of opal-based nanostructured materials. *Microchim. Acta Suppl.* **15**, 211–217.

Utsunomiya S., Valley J. W., Cavosie A. J., Wilde S. A. and Ewing R. C. (2007) Radiation damage and alteration of zircon from a 3.3 Ga porphyritic granite from the Jack Hills, Western Australia. *Chem. Geol.* **236**, 92–111.

Watson E. B., Cherniak D. J., Hanchar J. M., Harrison T. M. and Wark D. A. (1997) The incorporation of Pb into zircon. *Chem. Geol.* **141**, 19–31.

Wenzel T., Mertz D. F., Oberhänsli R., Becker T. and Renne P. R. (1997) Age, geodynamic setting, and mantle enrichment processes of a K-rich intrusion from the Meissen Massif (Northern Bohemian Massif) and implications for related occurrences from the Mid-European Hercynian. *Geol. Rundsch.* **86**, 556–570.

Wiedenbeck M., Allé P., Corfu F., Griffin W. L., Meier M., Oberli F., von Quadt A., Roddick J. C. and Spiegel W. (1995) Three natural zircon standards for U–Th–Pb, Lu–Hf, trace element and REE analyses. *Geostandard. Newslett.* **19**, 1–23.

Willner A., Sindern S., Metzger R., Ermolaeva T., Kramm . U., Puchkov V. and Kronz A. (2003) Typology and single grain U/Pb ages of detrital zircons from Proterozoic sandstones in the SW Urals (Russia): early time marks in the eastern margin of Baltica. *Precambrian Res.* **124**, 1–20.

Wirth R. (1997) Water in minerals detectable by electron energy-loss spectroscopy EELS. *Phys. Chem. Minerals* **24**, 561–568.

Wirth R. (2004) Focused Ion Beam (FIB): a novel technology for advanced application of micro- and nanoanalysis in geosciences and applied mineralogy. *Eur. J. Mineral.* **16**, 863–876.

Woodhead J. A., Rossman G. R. and Thomas A. P. (1991) Hydrous species in zircon. *Am. Mineral.* **76**, 1533–1546.

Zhang M., Salje E. K. H., Farnan I., Graeme-Barber A., Daniel P., Ewing R. C., Clark A. M. and Lennox H. (2000) Metamictization of zircon: Raman spectroscopic study. *J. Phys. Condens. Matter* **12**, 1915–1925.

Zhang M., Salje E. K. H. and Ewing R. C. (2002) Infrared spectra of Si–O overtones, hydrous species, and U ions in metamict zircon: radiation damage and recrystallization. *J. Phys. Condens. Matter* **14**, 3333–3352.

Associate editor: Yuri Amelin

Appendix 3

Nasdala, L., Hanchar, J.M., Rhede, D., Kennedy, A.K. & Váczi, T. (2009): Retention of uranium in complexly altered zircon: An example from Bancroft, Ontario.
Chemical Geology, DOI: 10.1016/j.chemgeo.2009.10.004.

Chemical Geology xxx (2009) xxx–xxx

Contents lists available at ScienceDirect

Chemical Geology

journal homepage: www.elsevier.com/locate/chemgeo

Retention of uranium in complexly altered zircon: An example from Bancroft, Ontario ☆

Lutz Nasdala [a,*], John M. Hanchar [b], Dieter Rhede [c], Allen K. Kennedy [d], Tamás Váczi [a]

[a] Institut für Mineralogie und Kristallographie, Universität Wien, A-1090 Wien, Austria
[b] Department of Earth Sciences, Memorial University of Newfoundland, St. John's, Canada NL A1B 3X5
[c] Sektion 4.2, Anorganische und Isotopengeochemie, Helmholtz-Zentrum Potsdam, Deutsches GeoForschungsZentrum GFZ, D-14473 Potsdam, Germany
[d] Department of Imaging and Applied Physics, Curtin University of Technology, Perth, WA 6102, Australia

ARTICLE INFO

Article history:
Received 12 June 2009
Received in revised form 25 September 2009
Accepted 2 October 2009
Available online xxxx

Editor: B. Bourdon

Keywords:
Zircon
Radiation damage
Uranium retention

ABSTRACT

Mesoproterozoic (~1050 Ma; Stenian) zircon crystals from the Saranac Prospect, Bancroft, Ontario, contain up to ~1 wt.% U and ~0.15 wt.% Th and, correspondingly, they are for the most part extensively radiation-damaged (calculated total α-doses $2.3-35.3\times10^{18}$/g). The crystals show textures of complex, intense chemical alteration that is attributed to multiple, low-*T* replacement events along fluid-controlled reaction fronts. Centers of crystals appear totally replaced; the primary zoning is virtually erased and the material has high porosity and numerous inclusions. Interior regions surrounding the central reworked areas still exhibit primary igneous-type zoning; in those regions the alteration emanates from fractures and then follows the more radiation-damaged growth zones. Altered areas are typically recognized by their high porosity, low BSE intensity, and deficient analytical totals. Those regions often have lost a significant fraction of their radiogenic Pb. They are in general somewhat depleted in Zr, Si, and U, and are notably enriched in Ca and Fe. Element maps reveal elevated concentrations of Al and Y within filled fractures. Our observations indicate that the fluid-driven ion exchange is mainly controlled by the accessibility of micro-areas with elevated levels of radiation damage to transporting fluids via "fast pathways". Most importantly, there is apparent Zr—Si—U equilibrium between initially existing and newly formed zircon. The retention of U after the chemical replacement (94 ± 14% relative to the original U content in the respective zones) does not significantly fall below the retention of two major cations Zr (95 ± 4%) and Si (95 ± 2%). In spite of the partially extreme hydrothermal alteration overprinting, the original U zoning in the crystals is well preserved. These observations suggest that preferential chemical leaching of U from zircon is clearly not a general feature of this mineral. This in turn seems to question the general validity of hydrothermal experiments to low-T, fluid-driven alteration of zircon in geological environments. The observed apparent immobility of U may affect the interpretation of U—Pb discordance in zircon, and the performance assessment of this mineral as potential waste form for actinides.

1. Introduction

Zircon ($ZrSiO_4$; $I4_1/amd$) is a common accessory phase in many rocks. This mineral is remarkably resistant against dissolution or chemical alteration over a wide range of geological environments and *P*—*T* conditions. Zircon normally incorporates, apart from Hf, low levels of non-formula elements. In particular, Pb is typically excluded in primary growth (Krogh, 1993) whereas radiogenic Pb, produced and "implanted" by radioactive decay of trace amounts of U and Th, is retained over billions of years as a result of the extremely low volume diffusion rate of Pb in zircon (Cherniak and Watson, 2001, 2003). Because of these extraordinary properties, zircon has been historically the mineral of choice for U—Th—Pb geochronology (e.g., Davis et al., 2003; and references therein).

The intrinsic physical properties and the chemical resistance of zircon, however, are dramatically affected by the accumulation of structural radiation damage, which is primarily produced by heavy recoil nuclei, and to a much lesser extent by the alpha particles ejected during the decay process, in alpha-decay events (Ewing, 1994; Weber et al., 1994, 1998; Nasdala et al., 2001). In the past two decades, zircon has also been proposed as a potential repository mineral for the long-term disposal of spent nuclear fuel and dismantled nuclear weapons (Ewing, 1999, 2001; Lumpkin, 2006). The performance assessment of zircon, and other U- and Th-bearing accessory minerals, as future host ceramic material for the long-term storage and isolation of heavy radionuclides therefore requires knowledge of irradiation effects, the accompanying changes of physical properties, and the response of

☆ This paper is dedicated to Dr. Thomas E. Krogh (1936–2008), who made several outstanding contributions throughout his career to the radiometric dating of zircon, in particular through the development of new analytical techniques. Thomas Krogh had collected the sample that was studied in this contribution.

* Corresponding author.
E-mail address: lutz.nasdala@univie.ac.at (L. Nasdala).

0009-2541/$ – see front matter © 2009 Elsevier B.V. All rights reserved.
doi:10.1016/j.chemgeo.2009.10.004

variably radiation-damaged solids to changes of *P* and *T*. Research addressing these, and related questions, can be subdivided into three major groups: (i) studies of radiation effects and alteration processes in well-characterized natural samples, including their behavior in annealing and hydrothermal experiments; (ii) analogous studies of synthetic ceramic compounds doped with short-lived alpha emitters (e.g., ^{238}Pu, ^{237}Np, etc.), or samples that were irradiation-damaged through ion implantation in the laboratory; and (iii) theoretical *ab initio* studies and predictions such as molecular dynamics calculations (e.g., Ewing, 2001; Ewing et al., 2003).

The present study belongs to the first group. Thorough evaluation of natural alteration processes and their resulting effects add to the knowledge on the chemical and physical stability of variably radiation-damaged accessory minerals in a low-*T* hydrothermal environment over extended geologic periods of time. It is well known that the behavior of zircon under such conditions may vary appreciably. First, this is controlled to a large extent by the amount of accumulated radiation damage, which in turn is directly related to the initial U and Th contents, and the respective distribution of those elements within the zircon structure. However, even though the dissolution kinetics of zircon is enhanced as radiation damage accumulates in the crystal structure, radiation damage itself does not cause elemental losses but merely increases their probability (Davis and Krogh, 2000). The second major control of the chemical and physical stability of zircon is the thermal and potentially the chemical and physical alteration history; in the latter case especially the geochemical environment in which the zircon resided. Even the treatment of zircon with high purity water may result in the notable loss of both Pb and U (Hansen and Friderichsen, 1989). In contrast, secondary Pb loss was insignificant in zircon that spent geologic periods immersed in connate water at moderately elevated *T* (Gentry et al., 1982); conditions expected in a nuclear repository. Caruba et al. (1974) summarized that zircon has a wide stability in acidic solutions whereas the chemical stability is notably lowered in alkaline environments. Also, hydrothermal experiments yielded variable results. Pidgeon et al. (1966) and Shukolyukov et al. (1994) observed that hydrothermal treatment of zircon resulted in notable Pb loss but insignificant U loss. Sinha et al. (1992) obtained similar results (e.g., strong Pb loss and moderate U loss); however, only upon hydrothermal treatment of zircon with 2% HNO_3 solution whereas Pb and U were almost equally depleted after treatment in a 2 M NaCl solution. Preferential U loss from zircon was also reported by Prasad and Naidu (1971), Tole (1985), Mattinson (1994, 2005), and Geisler et al. (2002, 2003b). Rizvanova et al. (2000) observed that U gain and large Pb losses (connected with zircon decomposition) resulted from experiments in which the zircon crystals were subjected to a 1 M NaOH solution. In contrast, treatment in 1 M NaCl solution was found to result in Pb and especially U loss by these authors. These diverse results may suggest that in undertaking such hydrothermal experiments, more care should be taken to select experimental conditions (especially the compositions of the fluids doing the alteration) that are relevant to natural environments. In the present study, we report results in the changes of the elemental and U–Pb isotopic compositions of a natural, highly radiation-damaged zircon sample that has undergone extreme chemical and physical alteration.

2. Materials and methods

The zircon sample investigated in this study, consisting of six large zircon single-crystals, was obtained from the late Dr. Thomas E. Krogh in 1997. The crystals came from the Saranac Prospect (also referred to as Saranac Property in some reports; see Satterly (1957), Bancroft District, Ontario, Canada. They originate from a thorite–zircon-rich albite leucogranite, a granite pegmatite, or associated skarn rocks enriched in zircon and thorite (Satterly, 1957).

Microprobe mounts were produced by cutting crystals along the crystallographic *c*-axis and embedding them (together with ion microprobe calibration standards) in araldite epoxy. Crystals were then ground and polished to their centers, to reveal internal textures of the crystals. For optical microscopy, doubly-polished thin sections attached to a glass slide, with thicknesses of ~30 μm, were prepared. Prior to electron microprobe and ion microprobe analysis, sample mounts were coated with carbon or gold, respectively.

Internal textures were inspected under an optical microscope, in plane-polarized and cross-polarized transmitted light. This technique was also used to determine the birefringence, whose decrease is a reliable estimate of the accumulated radiation damage (Morgan and Auer, 1941; Sahama, 1981; Chakoumakos et al., 1987). The degree of structural damage was also estimated from the broadening of the $\nu_3(SiO_4)$ Raman band (Nasdala et al., 1995). Raman spectra were obtained by means of a confocal Horiba Jobin Yvon LabRam HR800 spectrometer with 632.8 nm He–Ne excitation. More experimental details are reported elsewhere (Nasdala et al., 2005). Band fitting and determination of the full width at half-maximum (FWHM) were done assuming Lorentzian–Gaussian band shapes. The mathematical correction of FWHMs for the experimental broadening (i.e., apparatus function) has been discussed in detail by Nasdala et al. (2001).

Back-scattered electron (BSE) images, and wavelength-dispersive X-ray analyses of the chemical composition, including element distribution maps, were obtained with a JEOL JXA-8500F electron probe micro-analyzer (EPMA) equipped with a thermal field emission electron gun. For individual spot analyses, the accelerating voltage was set to 15 kV and the beam current used was 20 nA. The electron beam was focused to a <0.1 μm spot. Calibration standards used were well-characterized natural and synthetic materials including zircon (Si, Zr), corundum (Al), hematite (Fe), vanadinite (Pb), phosphates (P, Y, Yb), HfO_2 (Hf), and metals (U, Th). The CITZAF routine in the JEOL software, which is based on the $\Phi(\rho Z)$ method (Armstrong, 1995), was used for data processing. Element distribution maps, consisting of 250×200 pixels with inter-distances of 0.2–0.5 μm, were obtained with an accelerating voltage of 6–15 kV, a beam current of 10–40 nA, and a dwell time of 1–1.5 s/pixel. For more details see Keller et al. (2008).

Analyses of the U–Th–Pb isotopic composition were done using a SHRIMP II at Curtin University of Technology, Perth. The zircon surface was sputtered with a primary, mass-filtered $(O_2)^-$ beam with ~1 nA current, focused to a ~10 μm spot. The mass resolution, $M/\Delta M$, was better than 5000. For more experimental details see De Laeter and Kennedy (1998). To avoid mixed results due to the ion beam having straddled both unaltered and altered volumes, analysis spots were located carefully within the different regions, and only regions that appeared either fully unaltered or completely altered on a scale of at least 20–30 μm were analyzed in the SHRIMP. Results were calibrated against M257, a 561.3 Ma old reference zircon (Nasdala et al., 2008). Common Pb was assumed to have a Broken Hill Pb composition and was corrected for using the ^{204}Pb method (Compston et al., 1984). Data reduction was done using the ^{238}U decay constant of Jaffey et al. (1971; 1.55125×10^{-10}) and the revised ^{235}U decay constant of Schoene et al. (2006; 9.8569×10^{-10}). The Excel-based program Squid (Ludwig, 2002) was used for data processing. Data were plotted using the Isoplot program (Ludwig, 2003).

3. Results and discussion

3.1. Textural patterns of secondary alteration

Transmitted light photomicrographs of typical zircon crystals from the Saranac Prospect are shown in Figs. 1 and 2a and b, and representative BSE images are presented in Figs. 2c–f and 3. The zircon crystals range in size from several millimeters to approximately 1 cm, are dark brown in color, and have well-formed, euhedral prismatic shapes. In some of the grains, large inclusions of K-feldspar and/or α-quartz are present (e.g., left crystal in Fig. 1a).

Please cite this article as: Nasdala, L., et al., Retention of uranium in complexly altered zircon: An example from Bancroft, Ontario, Chemical Geology (2009), doi:10.1016/j.chemgeo.2009.10.004

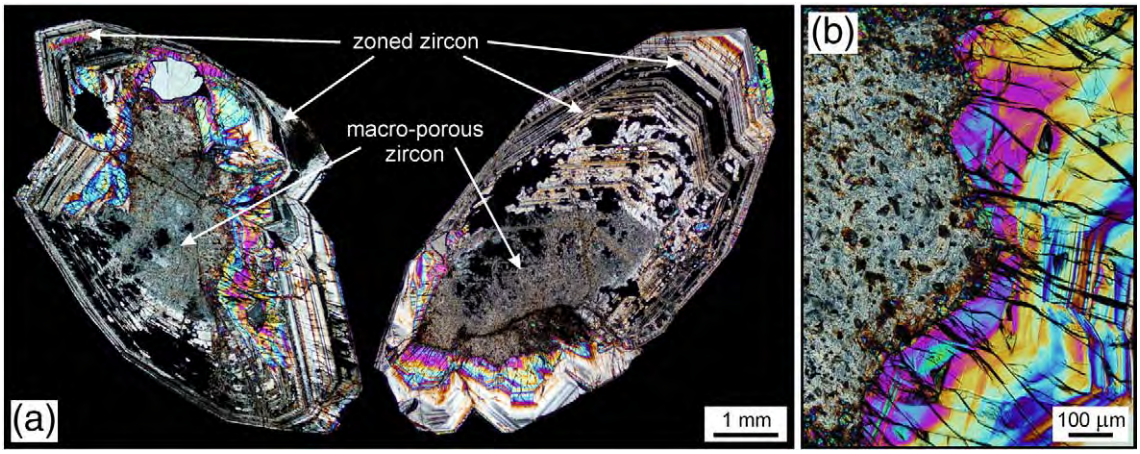

Fig. 1. Photomicrograph (transmitted, cross-polarized light) of two large, heterogeneous zircon crystals from the Saranac Prospect prepared as 30 µm thin section (a), and close-up of the sharp boundary between the macro-porous and zoned interior regions (b).

The zircon crystals show complex internal textures, consisting of two main textural varieties (Fig. 1). First, a large majority of the interiors of the zircon crystals show growth zoning (often referred to as oscillatory zoning) that is characteristic of primary zircon growth in an igneous (Connelly, 2000; Hoskin, 2000; Corfu et al., 2003) or metasomatic environment (Smith et al., 1991). Second, there are extended regions, mostly close to the centers of crystals, in which the primary zoning for the most part has been obliterated. These regions show rather chaotic textural patterns and are rich in inclusions and both sub-micrometer sized and macroscopic pore spaces; the latter up to a few tens of micrometers in size (Fig. 3). We will refer to the two textural types as "zoned" and "macro-porous". Zoned and macro-porous zircon regions were observed, though with moderate variations of their volume fractions (estimated ranges are 30–70 vol.% each), in all six crystals studied.

The zoned regions in the zircon crystals are highly fractured, with a radial pattern (Fig. 2a–c) that we assign to differential volume expansion of neighboring zones with differing degrees of radiation damage (Peterman et al., 1986; Chakoumakos et al., 1987; Lee and Tromp, 1995; Nasdala et al., 1999; Sláma et al., 2008). There is no indication of hydraulic fracturing in these zircon crystals (cf. Rimša et al., 2007).

The zoned zircon is extensively altered, indicated by a significant volume fraction of areas with notably lower BSE intensities (Fig. 2c–f). The boundary of the altered patches to their neighboring high-BSE areas is always sharp, reflecting a two-dimensional, fluid-driven alteration reaction front (cf. Geisler et al., 2003b; Labotka et al., 2004; Putnis et al., 2007; Pöml et al., 2007). In contrast, a gradual or transitional change in the BSE intensity would indicate a diffusional alteration reaction process; this is not observed. The altered, low-BSE micro-areas are located along fractures (Fig. 2c–e) or along the growth zoning (Fig. 2c, e, f).

The macro-porous zircon is characterized predominantly by very low BSE intensities (Fig. 3). Both the very low BSE intensities along with extensive porosity (e.g., Nasdala et al., 2009), and the apparent obliteration of the primary growth zoning, suggest that the macro-porous zircon has experienced extreme alteration, most probably through a fluid-driven replacement reaction process. The altered nature of the macro-porous zircon is indicated as well by the presence of numerous inclusions of phases that are typically not present in primary zircon (cf. Corfu et al., 2003; Johan and Johan, 2005; Breiter et al., 2006). The macro-porous zircon is especially rich in inclusions of high-BSE phases such as uranium oxide, uranium and thorium silicates, lead sulfide, and an unidentified yttrium silicate phase. Less abundant low-BSE inclusions include SiO_2, K-feldspar, and rarely apatite.

There is often a sharp, well-defined boundary between the two textural types (Fig. 1b), however, in some cases a gradual transition may also be observed. The sharp boundary follows in some cases the growth zoning whereas in other cases it does not. These observations seem to exclude that the zoned zircon overgrew the macro-porous zircon; rather the two textural types seem to represent different alteration products of the same primary zircon material.

3.2. Chemical changes during alteration

Electron microprobe analyses of the chemical composition of the zircon crystals studied are presented in Table 1. Analytical results vary appreciably, with a conspicuous correlation between the BSE intensity and the EPMA results.

Within the zoned zircon, most low-BSE areas have deficient analytical totals in the 94–98 wt.% oxide range. These areas are notably depleted in SiO_2 and ZrO_2 whereas there are elevated levels of non-formula chemical elements including CaO (up to 3.1 wt.%), FeO (up to 0.7 wt.%), and in some cases Al_2O_3. High-BSE areas, in contrast, yielded rather "regular" stoichiometric SiO_2 and ZrO_2 values, almost no Ca, Fe, and Al, and much less deficient analytical totals (typically, 98–100 wt.%). The non-formula constituents HfO_2, UO_2, and Y_2O_3 were detected in all areas, and they do not show any direct correlation with the BSE intensity. The strong variations of these elements among the eleven growth zones (labeled A–K in Table 1), however, suggest primary compositional zoning. All other non-formula elements were mostly close to, or below, the detection limit.

Similar results were obtained from the macro-porous zircon, though with a weaker correlation with the BSE intensity. The depletions in SiO_2 and ZrO_2 correlate with deficiencies in analytical totals and the BSE intensity. Higher-BSE regions have analytical totals between 97–98 wt.%, and low-BSE regions between 92–97 wt.%, (Table 1). Similar to the zoned zircon, CaO (1.7–3.8 wt.%) and FeO (0.4–0.8 wt.%) are clearly enriched in low-BSE areas of the macro-porous zircon but mostly not detected in high-BSE areas. As noted above, all other non-formula elements do not correlate with the BSE intensity.

Note that deficient analysis sums do not necessarily suggest the presence of a hydrous phase; even though the analytical shortfall of zircon EPMA analyses was sometimes assigned to a hypothetical "H_2O^*" (e.g., Johan and Johan, 2005; Utsunomiya et al., 2007). Deficient totals, obtained for non-hydrous, porous solids (Lakis et al., 1992; Sorbier et al., 2004), are explained by charge trapping, pore geometry variation, and losses of X-ray quanta at interfaces. In the case of hydrothermally altered zircon, porosity (Figs. 2f and 3) is especially common because of radiation-damaged and hence volume-expanded zircon being replaced

Please cite this article as: Nasdala, L., et al., Retention of uranium in complexly altered zircon: An example from Bancroft, Ontario, Chemical Geology (2009), doi:10.1016/j.chemgeo.2009.10.004

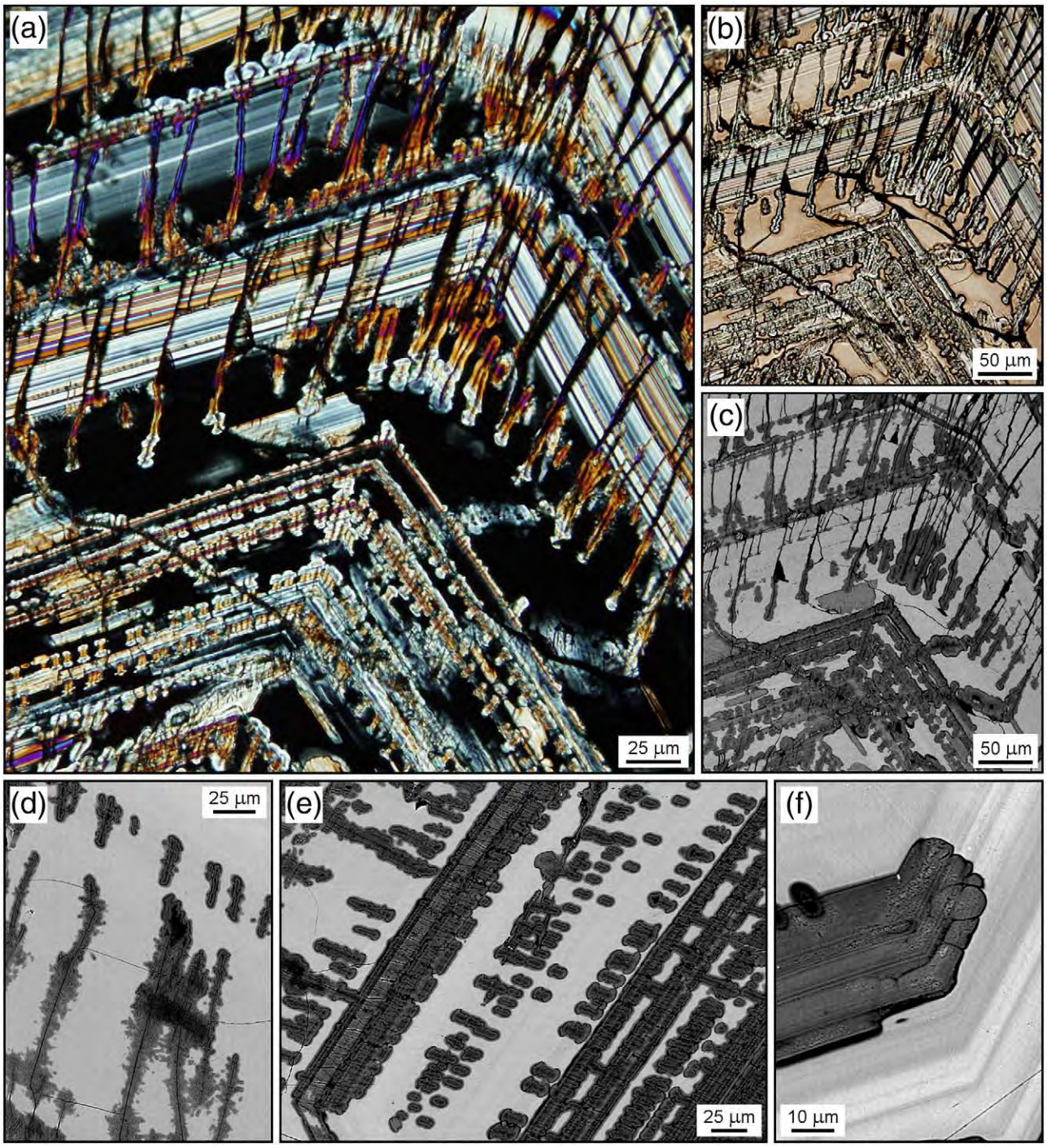

Fig. 2. Images of the zoned zircon. Series of cross-polarized (a) and plane-polarized (b) transmitted light photomicrographs and BSE image (c) of a partially altered region. Altered micro-areas that emanate from fractures have a finger-like appearance, are virtually de-colored, and show enhanced birefringence and darker BSE intensity compared to neighboring areas of the same growth zones. (d) BSE image showing alteration emanating from large fractures. (e) BSE image of an intensely altered area. Alteration had followed the primary growth zoning. (f) Close-up showing that the primary zoning is still preserved in the altered material (dark BSE), which is characterized by sub-micrometer range porosity (center of image).

by crystalline zircon (Nasdala et al., 2009). Deficient totals, and the accompanying effect of very low BSE intensities in such areas (Figs. 2 and 3; cf. Pointer et al., 1988; Smith et al., 1991; Nasdala et al., 2009) are, therefore, strong indicators of secondary alteration.

Non-formula elements such as Ca, Al, and Fe (in contrast to Hf and the actinides U and Th) are normally excluded during primary zircon growth whereas they are typically observed in chemically altered zircon (Törnroos, 1985; Smith et al., 1991; Geisler et al., 2003a; Pérez-Soba et al., 2007). Those results are confirmed by EPMA analyses, which yielded elevated Ca and Fe concentrations only in the altered, low-BSE micro-areas adjacent to the primary zoned zircon regions. Phosphorous, however, which is also a common constituent in altered zircon (e.g., Mathieu et al., 2001; Tomaschek et al., 2003; Utsunomiya et al., 2007; Van Lichtervelde et al., 2009), was not detected in any of the six Saranac Prospect zircon crystals that were investigated. The results of this present study are similar to those of Krogh and Davis (1973, 1975) who found altered zircon to be depleted in Zr and Si, and enriched in Ca, Fe, and Al.

To study elemental changes upon alteration in more detail, high-resolution EPMA X-ray element mapping was done (Fig. 4). Distribution

Please cite this article as: Nasdala, L., et al., Retention of uranium in complexly altered zircon: An example from Bancroft, Ontario, Chemical Geology (2009), doi:10.1016/j.chemgeo.2009.10.004

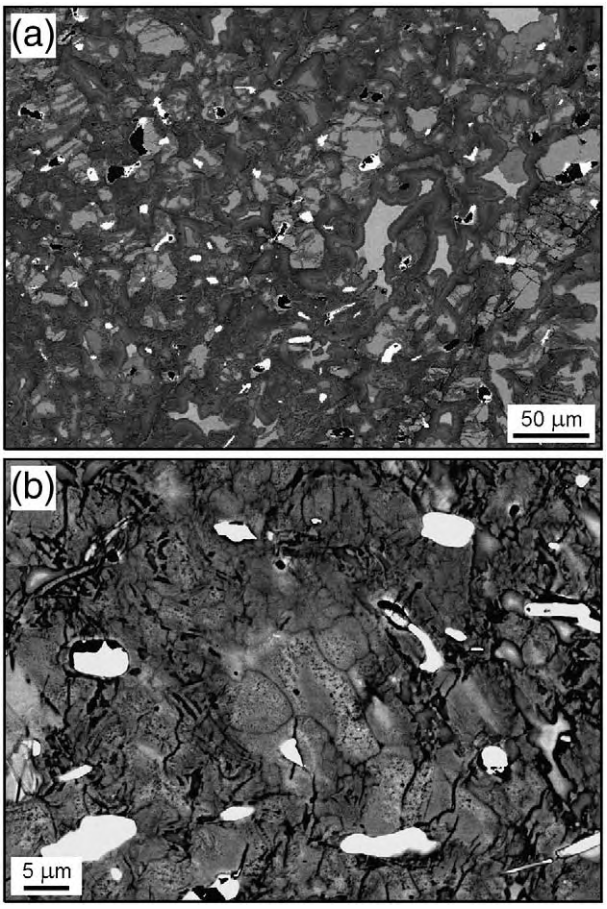

Fig. 3. Two BSE images of the macro-porous zircon. (a) A large volume fraction of the zircon shows dark BSE and is characterized by rather chaotic textures. This material is rich in inclusions with high average atomic number (bright) and pores (black) with sizes up to several tens of micrometers. (b) Close-up showing additional sub-micrometer porosity (center of image).

patterns vary appreciably between elements; they can be assigned to three principal groups: (i) Concentrations (or, more exactly, detected EPMA count rates) of Zr (Fig. 4a, b), Si (not shown), Hf (not shown), and U (Fig. 4a, b) are mainly determined by the strong primary chemical zoning. Alteration patterns (i.e., the comparably smaller concentration variations internal to unaltered and altered micro-areas) are recognized if only the upper portions of the count rate scales are used to generate color-coded distribution maps of these elements (e.g., Zr concentration distributions in Fig. 4a and b; compare count rate ranges given in the caption). The primary zoning is, though on a very low level and hence more noisy, also seen in the Y patterns (Fig. 4a); (ii) The distribution patterns of Ca (Fig. 4b, c) and Fe (not shown) are consistent with the BSE intensities and hence the locations of the alteration. These two elements always yield high counts in altered dark BSE, and low counts in high-BSE areas whereas they did not show detectable variations among primary growth zone regions; (iii) Yttrium (Fig. 4a) and Al (Fig. 4c) show their highest concentrations in, or near, major fractures within the altered areas, with much lower count rates in the bulk of the altered areas. This suggests that non-formula elements were not homogeneously incorporated. Rather Y and Al might be assigned to the youngest fracture fillings, possibly representing a late stage of the ion-exchange processes.

3.3. Effects of alteration on the U—Pb and Th—Pb isotopic systems

SHRIMP U—Th—Pb analysis results are listed in Table 2, along with birefringence, Raman band broadening, and BSE intensity data characterizing the analyzed micro-areas. Homogeneous high-BSE areas within the macro-porous zircon were too small for SHRIMP analysis, so only low-BSE areas within the macro-porous zircon were analyzed with the SHRIMP.

Almost one-half of the measured spots yielded highly discordant data in the U—Pb isotopic system (Table 2). Again, there is a clear correlation with the observed BSE intensities, and hence the alteration distribution within crystals; all low-BSE areas are normally discordant, plotting below the Concordia in Fig. 5. A number of analyses in the zoned zircon yielded slight (mostly within the analytical uncertainty of measurements) reverse discordance; which may be either real or an analytical artifact. The SHRIMP analyses of high-uranium minerals such as zircon, monazite, or xenotime, often yield reversely discordant data with an apparent excess of Pb relative to U, especially in radiation-damaged regions in those minerals. This could be attributed to U loss (for instance due to ^{234}U ejection from porous zircon; Romer, 2003) or, less likely, to Pb gain (Williams et al., 1984). Alternatively, zircon decomposition into oxides may result in reversely discordant U—Pb data during SHRIMP analyses. This analytical artifact is produced by enhanced sputtering of Pb, which is preferentially incorporated into SiO_2 relative to U, which is preferentially incorporated in ZrO_2 (cf. McLaren et al. (1994). Williams and Hergt (2000) have identified a matrix affect on SHRIMP analyses where reverse discordance is correlated with U content in zircon with >2000 ppm U. However, reversely discordant SHRIMP data is obviously not a general feature of U-rich zircon: Nasdala et al. (2002) obtained generally concordant U—Pb SHRIMP data for a highly metamict (amorphous), but unaltered, Sri Lankan gem zircon containing ~5500 ppm of uranium.

It is most remarkable that the U—Pb data obtained within the zoned and the macro-porous zircon show the same general trend; all seem to plot near a discordia line that intersects the Concordia at 1053 ± 11 and 266 ± 38 Ma [mean square weighted deviation (MSWD) = 9.2]. Separate evaluation of measurements within the two textural types yielded intercepts at 1050 ± 12 and 251 ± 60 Ma (MSWD = 8.0) for the zoned and intercepts at 1058 ± 31 and 290 ± 62 Ma (MSWD = 8.0) for the macro-porous zircon, which are identical within error. The relevance of the calculated lower intercept age of 266 ± 38 Ma, however, should not be overestimated. We do not know whether the U—Pb disturbance is due to episodic Pb loss in the Permian to Early Mesozoic, or rather gradual young Pb leaching, or even multiple leaching events over a short time period after the initial closure of the U–Pb system (cf. Ashwal et al., 1999). There is no clear indication of recent Pb loss, as would be expected as a result of extensive incipient weathering (e.g., Compston et al., 1986; Black, 1987).

The nearly concordant Late Mesoproterozoic (Stenian) upper intercept age of 1050 ± 12 Ma of unaltered, light-BSE areas within the zoned zircon is likely to date primary zircon growth in an igneous environment, rather than complete U—Pb resetting. Given the slow diffusivity of Pb and U in crystalline zircon (i.e., volume diffusion) that does not have fast diffusion pathways, it is most unlikely that zircon with primary igneous zoning experienced complete U—Pb resetting at ~1050 Ma ago. The identical upper intercept age calculated within errors for the macro-porous zircon (1058 ± 31 Ma) is analogously assigned to the primary zircon growth. As discussed above, the boundary between macro-porous and zoned zircon is not always sharp but there may be a rather gradual transition (Fig. 1a). This seems to exclude the possibility that the macro-porous zircon represents inherited cores that were reset at the time of the igneous formation of the zoned zircon.

However, the age of when primary zircon was transformed into macro-porous zircon remains unclear. The assignment of this event appears most problematic; it can be accomplished in two ways, both of which involve a number of open questions. First, the transformation could also be assigned to the upper intercept age. This would indicate that the first alteration had occurred relatively shortly after primary growth, and that primary and alteration ages are similar and cannot

Please cite this article as: Nasdala, L., et al., Retention of uranium in complexly altered zircon: An example from Bancroft, Ontario, Chemical Geology (2009), doi:10.1016/j.chemgeo.2009.10.004

Table 1
Results of EPMA chemical analyses (wt.%).

Analysis no.	Zone[a]	BSE intensity	Al_2O_3	SiO_2	CaO	FeO	Y_2O_3	ZrO_2	Yb_2O_3	HfO_2	PbO	ThO_2	UO_2	Total
Analyses in zoned interior regions:														
1	A	High	(bdl)	33.6	(bdl)	(bdl)	(bdl)	65.1	(bdl)	0.79	0.02	0.03	0.20	100.2
2	A	High	(bdl)	33.6	(bdl)	(bdl)	0.13	65.0	(bdl)	1.24	0.03	0.02	0.22	100.6
3	B	High	(bdl)	33.4	(bdl)	(bdl)	0.16	64.9	(bdl)	0.88	0.04	0.03	0.35	100.2
4	B	High	(bdl)	32.2	(bdl)	(bdl)	0.21	65.4	(bdl)	0.99	0.08	0.02	0.39	99.9
5	B	Low	0.09	30.4	2.89	0.58	0.14	60.6	(bdl)	1.23	(bdl)	(bdl)	0.32	96.6
6	C	High	(bdl)	32.0	(bdl)	(bdl)	0.15	64.8	(bdl)	0.37	0.08	0.05	0.54	98.3
7	C	Low	0.91	30.7	3.07	0.70	0.79	56.2	(bdl)	0.69	(bdl)	0.03	0.45	94.7
8	D	High	(bdl)	32.2	(bdl)	(bdl)	0.24	65.1	(bdl)	1.01	0.05	0.03	0.42	99.6
9	D	Low	0.12	30.2	3.10	0.60	0.22	60.1	(bdl)	0.60	(bdl)	0.03	0.32	95.6
10	E	High	(bdl)	32.1	(bdl)	(bdl)	0.15	64.8	(bdl)	0.87	0.06	0.02	0.40	98.9
11	E	Intermediate	(bdl)	29.6	0.66	0.26	0.16	61.3	0.23	0.64	0.06	(bdl)	0.35	93.7
12	F	High	(bdl)	33.7	(bdl)	(bdl)	0.14	65.1	(bdl)	0.92	0.03	(bdl)	0.20	100.4
13	F	High	(bdl)	32.0	(bdl)	(bdl)	(bdl)	65.3	(bdl)	0.88	(bdl)	(bdl)	0.08	98.8
14	F	High	(bdl)	32.1	(bdl)	(bdl)	0.08	65.1	(bdl)	0.83	0.02	(bdl)	0.08	98.6
15	F	High	(bdl)	32.2	(bdl)	(bdl)	(bdl)	64.7	(bdl)	1.35	0.05	(bdl)	0.06	98.9
16	F	High	(bdl)	31.9	(bdl)	(bdl)	(bdl)	64.5	(bdl)	1.40	(bdl)	(bdl)	0.09	98.5
17	G	High	(bdl)	31.9	(bdl)	(bdl)	0.31	64.0	(bdl)	0.84	0.10	0.08	0.72	98.4
18	G	Intermediate	(bdl)	31.4	0.92	0.26	0.30	62.8	(bdl)	1.65	0.19	0.09	0.85	99.2
19	H	High	(bdl)	31.9	(bdl)	(bdl)	0.23	64.0	(bdl)	0.85	0.15	0.09	0.87	98.3
20	H	Low	(bdl)	30.8	1.81	0.13	0.29	62.2	0.14	0.58	0.04	0.11	1.01	98.1
21	H	Low	(bdl)	30.8	1.50	0.10	0.29	62.6	0.15	0.52	0.10	0.09	0.89	97.6
22	I	High	(bdl)	32.0	(bdl)	0.09	0.29	64.0	(bdl)	1.00	0.11	0.07	0.86	99.0
23	I	Low	(bdl)	30.5	2.09	0.27	0.21	61.6	(bdl)	0.43	0.04	0.07	0.86	96.3
24	J	High	(bdl)	31.8	(bdl)	0.09	0.38	63.4	0.23	1.32	0.21	0.16	1.17	99.3
25	J	Low	(bdl)	30.6	1.21	0.04	0.38	61.9	0.14	0.82	0.24	0.13	1.14	96.8
26	K	High	(bdl)	31.7	(bdl)	0.09	0.10	64.3	(bdl)	0.48	0.02	0.02	0.22	97.7
27	K	High	(bdl)	31.7	(bdl)	(bdl)	(bdl)	64.6	(bdl)	0.64	(bdl)	(bdl)	0.22	97.5
Analyses in macro-porous interior regions:														
28	–	High	(bdl)	31.6	0.05	0.07	0.58	62.6	0.19	1.02	0.14	0.11	0.79	97.7
29	–	High	(bdl)	31.6	(bdl)	(bdl)	0.54	62.6	0.23	1.01	0.17	0.10	0.68	97.3
30	–	Intermediate	(bdl)	30.3	0.89	0.33	0.49	61.2	0.16	0.94	0.14	0.08	0.73	95.5
31	–	Intermediate	(bdl)	30.5	0.78	0.22	0.69	61.0	0.18	1.04	0.23	0.11	0.93	96.2
32	–	Low	(bdl)	30.0	3.17	0.58	0.57	58.2	0.20	1.01	0.03	0.10	0.92	95.3
33	–	Low	(bdl)	30.4	1.64	0.43	(bdl)	61.9	(bdl)	1.30	0.04	(bdl)	0.40	96.8
34	–	Low	0.16	29.7	2.18	0.61	0.62	59.3	(bdl)	0.93	0.03	(bdl)	0.38	94.4
35	–	Low	(bdl)	30.3	3.55	0.75	0.58	57.7	(bdl)	1.05	(bdl)	0.08	0.80	95.7
36	–	Low	(bdl)	30.3	2.68	0.48	0.48	59.8	0.18	1.09	0.06	0.10	0.81	96.4
37	–	Low	(bdl)	30.2	3.14	0.40	0.22	59.5	(bdl)	1.05	(bdl)	(bdl)	0.42	95.3
38	–	Low	(bdl)	30.1	2.48	0.41	(bdl)	60.4	(bdl)	0.42	(bdl)	0.02	0.55	95.3
39	–	High	(bdl)	31.5	(bdl)	(bdl)	0.47	62.6	0.17	1.19	0.12	0.09	0.79	97.5
40	–	High	(bdl)	31.5	(bdl)	(bdl)	0.60	62.6	0.16	0.89	0.13	0.10	0.83	97.4
41	–	Intermediate	0.04	30.2	3.74	0.54	0.42	56.8	(bdl)	0.75	0.04	0.05	0.56	93.6
42	–	Low	(bdl)	29.9	3.34	0.54	0.10	59.0	(bdl)	0.97	0.02	(bdl)	0.55	95.1
43	–	High	(bdl)	31.5	(bdl)	0.04	0.17	63.3	(bdl)	1.01	0.09	0.02	0.65	96.9
44	–	High	(bdl)	31.4	(bdl)	(bdl)	0.13	63.3	(bdl)	0.84	0.07	0.04	0.53	96.6
45	–	Low	(bdl)	28.7	2.66	0.38	0.71	57.0	0.25	0.83	0.06	0.13	1.01	92.5
46	–	Low	(bdl)	29.7	2.24	0.35	0.11	59.8	(bdl)	0.53	0.04	(bdl)	0.45	93.8
47	–	Intermediate	(bdl)	30.2	1.23	0.27	(bdl)	60.9	0.14	0.90	0.05	0.02	0.51	94.7
48	–	Low	(bdl)	30.6	3.81	0.54	0.66	57.4	0.13	1.24	0.02	0.14	1.06	96.5
49	–	Intermediate	(bdl)	29.7	0.64	0.15	(bdl)	60.7	(bdl)	0.53	0.07	(bdl)	0.46	93.1
50	–	High	(bdl)	31.3	0.06	(bdl)	0.69	61.8	0.12	1.02	0.16	0.15	0.90	96.7
51	–	High	(bdl)	31.8	(bdl)	(bdl)	0.08	64.2	(bdl)	1.47	0.02	(bdl)	0.20	98.5
52	–	Low	(bdl)	30.5	3.48	0.81	0.66	57.1	0.23	0.94	0.04	0.14	1.14	95.6
53	–	Intermediate	(bdl)	30.3	1.28	0.28	0.24	60.8	0.14	1.19	0.12	0.02	0.68	95.7
54	–	Low	(bdl)	29.9	3.59	0.72	0.10	58.6	0.15	0.94	(bdl)	(bdl)	0.58	95.2
Detection limit[b]			0.04	0.1	0.04	0.07	0.07	0.1	0.12	0.20	0.02	0.02	0.02	–

bdl = not detected, or below the detection limit quoted in the bottom row.
[a] Analyzed single zones within the zoned zircon have been numbered with capital letters, for better comparison of analyses belonging to the same growth zone.
[b] Average detection limit (wt.% oxide; 2σ error by counting statistics of the background signal).

be resolved by our U–Pb data. Second, the transformation could be assigned to a younger (i.e., Phanerozoic) event, possibly related to the (apparent) lower intercept age.

The first interpretation above is problematic as there are no obvious reasons for why, and how, only the central parts of crystals were reworked and transformed into the macro-porous zircon, whereas other parts were not and retained their primary zoning. There exists the possibility that higher levels of incorporated trace elements, structural defects, and perhaps syn-genetic inclusions, may have made the central areas to some degree more susceptible to this alteration process. However, it remains doubtful why the central areas (which were virtually encapsulated by their surrounding zones) were well accessible to alteration fluids whereas the surrounding areas themselves remained unaffected. Note that notable fracturing of the surrounding zoned zircon at the time of the alteration, due to more extensive radiation damage in the central areas (Krogh and Davis, 1975), is unlikely if the alteration occurred shortly after zircon growth: In spite of comparably high U and Th concentrations on the order of 1 wt.% and hence high self-irradiation rates, it would take at least several tens of millions of years to accumulate sufficient radiation

Please cite this article as: Nasdala, L., et al., Retention of uranium in complexly altered zircon: An example from Bancroft, Ontario, Chemical Geology (2009), doi:10.1016/j.chemgeo.2009.10.004

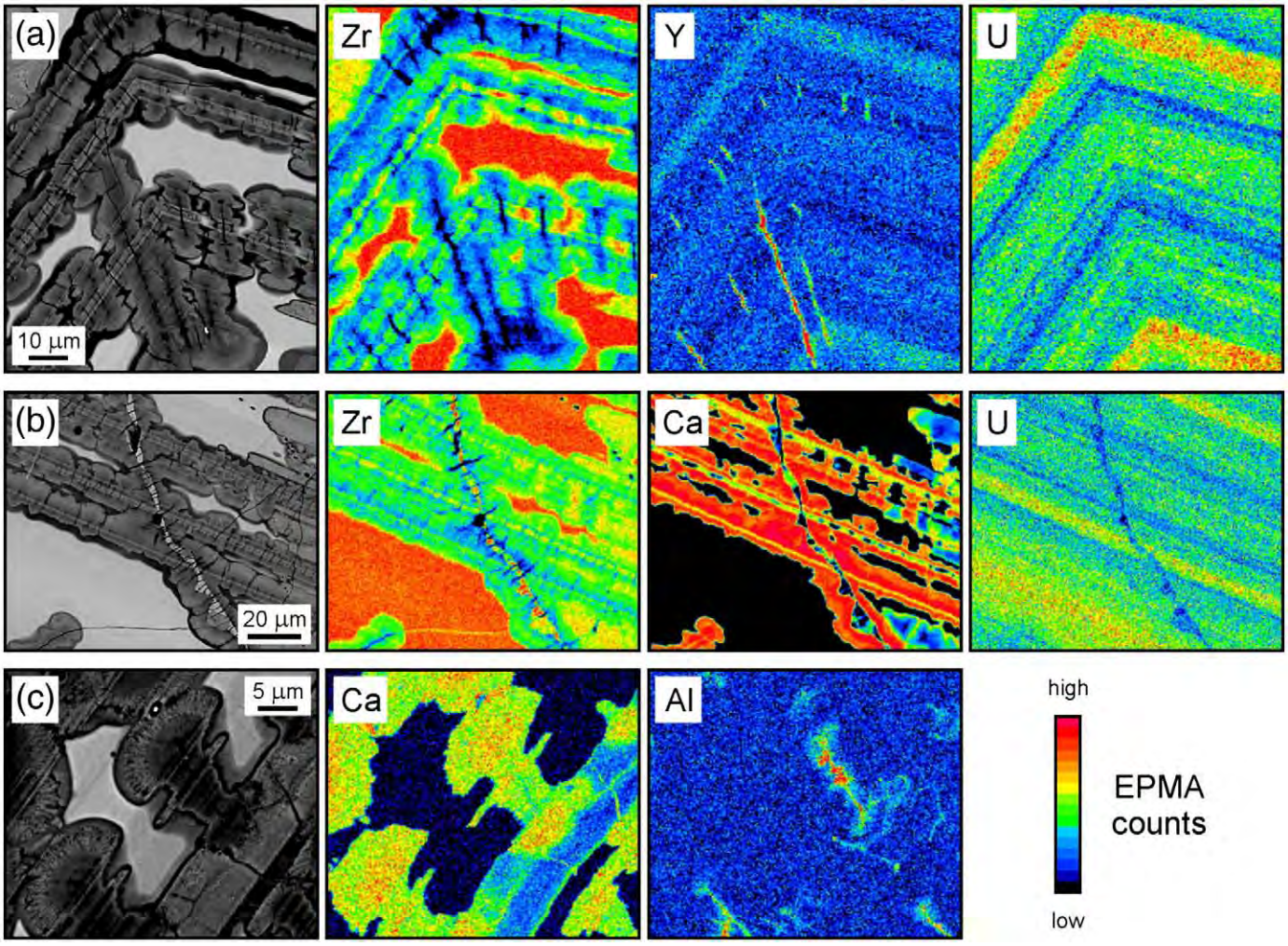

Fig. 4. Three series of EPMA element maps along with the corresponding BSE patterns, obtained in heavily altered areas within the zoned zircon. Color-coded count rate ranges (given in counts per second) are: upper row (15 kV, 4×10^{-8} A, dwell time 1.5 s), 9880−12,262 (Zr), 2−44 (Y), 27−107 (U); middle row (15 kV, 1×10^{-8} A, dwell time 1 s), 3500−4855 (Zr), 226−1333 (Ca), 5−50 (U); lower row (6 kV, 1×10^{-8} A, dwell time 1 s), 6−79 (Ca), 1−35 (Al).

damage to cause fracturing of less metamict zones (cf. Chakoumakos et al., 1987; Lee and Tromp, 1995).

The second interpretation above (in which the alteration is much younger than the upper intercept age) is also problematic as it appears unlikely that the majority of the radiogenic Pb has been retained during a fluid-driven replacement reaction that virtually completely erased the primary zoning during major textural reworking. On the other hand, it is well known that zircon affected by alteration processes may incorporate unusually high concentrations of common Pb (Corfu, 1987; Mathieu et al., 2001; Nasdala et al., 2009). We therefore cannot exclude the hypothetical possibility that the Saranac Prospect zircon may have undergone low-*T* alteration without notable loss of its radiogenic Pb. The assignment of the formation of the macro-porous zircon to a younger event would agree well with earlier interpretations (Krogh and Davis, 1975; rediscussed in Lumpkin, 2001) according to which the central, reworked areas were preferentially altered after having accumulated elevated levels of radiation damage, by fluids accessing though fractures in their surrounding zircon zones.

Alteration within the zoned zircon is clearly controlled by the accessibility of the alteration fluids through fractures (Fig. 2c, d) that formed by heterogeneous volume expansion resulting from heterogeneous self-irradiation. This second alteration process therefore must have occurred a significant time period after the primary zircon growth.

3.4. Self-irradiation damage

Most parts of the zircon crystals are characterized by remarkably low (i.e., 1st order gray) interference colors, or optical isotropy indicated by no interference at all (Fig. 1). Such interference colors correspond to birefringence values in the range 0.000−0.010 (Table 2). Only a small fraction of zones within the zoned interior region, in particular the outermost growth zones at pyramid faces (see Fig. 1a, tip of right crystal), show 2nd order to low 3rd order interference colors, corresponding to birefringence values of up to ~0.040. However, even the latter value is well below the birefringence of well-crystallized zircon (0.059; Tröger, 1982). The low birefringence is assigned to generally high levels of accumulated radiation damage, which is connected with the loss of anisotropy (cf. Morgan and Auer, 1941; Sahama, 1981; Chakoumakos et al., 1987).

This assignment is supported by Raman analyses of the Saranac Prospect zircon crystals. In zones with the highest interference colors, the main internal SiO_4 vibration (ν_3, anti-symmetric stretching; Dawson et al., 1971) was found to have a FWHM of 14–18 cm^{-1}. Zones and areas with 1st order gray interference color yielded low-intensity, asymmetric Raman bands with FWHMs exceeding 30 cm^{-1} (Table 2). In zones that did not show interference colors at all (Fig. 1a), no Raman bands of crystalline zircon were detected; this is assigned to an almost complete metamictization of these zones. The observed general relation between

Please cite this article as: Nasdala, L., et al., Retention of uranium in complexly altered zircon: An example from Bancroft, Ontario, Chemical Geology (2009), doi:10.1016/j.chemgeo.2009.10.004

Table 2
Results of SHRIMP U–Pb isotopic analyses.

Sample/spot				SHRIMP results										α dose[a] (10^{18}/g)	
No.	Δn	FWHM[b] (cm^{-1})	BSE	U (ppm)	Th (ppm)	Th/U	Pb (ppm)	f 206[c] (%)	$^{206}Pb/^{238}U$	$^{206}Pb/^{238}U$ age (Ma)	$^{207}Pb/^{206}Pb$	$^{207}Pb/^{206}Pb$ age (Ma)	Disc.[d] (%)	(1053 myr)	(266 myr)
Analyses in zoned interior regions:															
1	<0.001	(n.d.)	Low	6339	681	0.11	933	0.01	0.1549 ± 0.0031	928 ± 17	0.07372 ± 0.00012	1031 ± 3	11	24.6	5.7
2	<0.001	(n.d.)	High	7585	843	0.11	1421	0.00	0.1970 ± 0.0039	1159 ± 21	0.07424 ± 0.00009	1045 ± 3	−12	29.5	6.9
3	0.001	>30	Low	5249	627	0.12	886	0.01	0.1761 ± 0.0035	1046 ± 19	0.07459 ± 0.00012	1055 ± 3	1	20.5	4.8
4	<0.001	(n.d.)	High	6344	749	0.12	933	0.01	0.1825 ± 0.0031	1081 ± 20	0.07456 ± 0.00011	1054 ± 3	−3	24.7	5.8
5	0.028	27.4–30.2	High	1254	40	0.03	204	0.00	0.1742 ± 0.0034	1035 ± 19	0.07460 ± 0.00028	1055 ± 8	2	4.8	1.1
6	<0.001	(n.d.)	Low	8036	915	0.11	1475	0.00	0.1927 ± 0.0041	1136 ± 22	0.07412 ± 0.00019	1042 ± 5	−10	31.3	7.3
7	0.002	>30	Low	4967	478	0.10	301	0.05	0.0644 ± 0.0013	402 ± 8	0.06149 ± 0.00038	654 ± 13	40	19.3	4.5
8	0.040	14.0–14.8	High	604	30	0.05	95	0.05	0.1671 ± 0.0033	996 ± 18	0.07468 ± 0.00044	1057 ± 12	6	2.3	0.5
9	0.003	>30	Low	4260	365	0.09	681	0.01	0.1691 ± 0.0033	1007 ± 18	0.07459 ± 0.00014	1055 ± 4	5	16.5	3.8
10	<0.001	(n.d.)	Low	5835	594	0.10	802	0.02	0.1447 ± 0.0029	871 ± 16	0.07410 ± 0.00007	1041 ± 2	17	22.7	5.3
11	0.015	>30	High	1696	295	0.17	292	0.03	0.1777 ± 0.0035	1054 ± 19	0.07486 ± 0.00022	1062 ± 6	1	6.7	1.6
12	0.032	23.5–25.0	High	982	129	0.13	170	0.05	0.1807 ± 0.0036	1071 ± 20	0.07461 ± 0.00028	1055 ± 8	−2	3.8	0.9
13	0.005	>30	Low	3794	283	0.07	663	0.00	0.1854 ± 0.0037	1096 ± 20	0.07468 ± 0.00013	1057 ± 3	−4	14.6	3.4
14	0.004	>30	Low	3244	249	0.08	370	0.11	0.1083 ± 0.0021	663 ± 12	0.07082 ± 0.00024	949 ± 7	32	12.5	2.9
15	<0.001	(n.d.)	High	6836	817	0.12	1173	0.01	0.1800 ± 0.0036	1067 ± 19	0.07411 ± 0.00010	1042 ± 3	−3	26.6	6.2
16	0.004	>30	High	4131	309	0.07	730	0.01	0.1876 ± 0.0037	1108 ± 20	0.07422 ± 0.00013	1045 ± 3	−7	15.9	3.7
Analyses in macro-porous interior regions:															
17	<0.001	(n.d.)	Low	8979	1391	0.15	608	0.04	0.0708 ± 0.0015	441 ± 9	0.06262 ± 0.00039	693 ± 13	38	35.3	8.2
18	<0.001	(n.d.)	Low	8324	989	0.12	643	0.02	0.0815 ± 0.0018	505 ± 11	0.06395 ± 0.00050	737 ± 16	33	32.4	7.6
19	0.003	>30	Low	4109	463	0.11	595	0.01	0.1521 ± 0.0030	913 ± 17	0.07410 ± 0.00015	1041 ± 4	13	16.0	3.7
20	0.002	>30	Low	4727	53	0.01	693	0.03	0.1574 ± 0.0033	942 ± 18	0.07411 ± 0.00030	1042 ± 8	10	18.0	4.2
21	0.002	>30	Low	4416	301	0.07	347	0.00	0.0837 ± 0.0019	518 ± 11	0.06485 ± 0.00052	767 ± 17	34	17.0	4.0
22	0.001	>30	Low	4953	489	0.10	579	0.01	0.1226 ± 0.0024	745 ± 14	0.07122 ± 0.00071	961 ± 20	24	19.2	4.5
23	<0.001	(n.d.)	Intermediate	8461	1425	0.17	1417	0.00	0.1737 ± 0.0034	1033 ± 19	0.07373 ± 0.00009	1031 ± 2	0	33.3	7.8
24	0.011	>30	Low	1973	12	0.01	170	0.11	0.0917 ± 0.0021	565 ± 12	0.06977 ± 0.00031	919 ± 9	40	7.5	1.7
25	<0.001	(n.d.)	Low	5895	848	0.14	852	0.00	0.1508 ± 0.0030	905 ± 17	0.07348 ± 0.00012	1025 ± 3	12	23.1	5.4
26	0.001	>30	Low	4310	1169	0.27	619	0.02	0.1486 ± 0.0030	893 ± 17	0.07266 ± 0.00013	1002 ± 4	12	17.3	4.1

Isotopic ratios are corrected for common Pb (^{204}Pb method). Isotopic ratios and ages are quoted with 1σ uncertainties.
[a] Time-integrated alpha fluences, calculated according to (Murakami et al., 1991) from the present U and Th concentrations for assumed self-irradiation periods of 1053 and 266 myr.
[b] Full width at half-maximum of the $\nu_3(SiO_4)$ Raman band of zircon, determined from multiple analyses. n.d. = no Raman signal of crystalline $ZrSiO_4$ detected.
[c] f 206 = common ^{206}Pb/total ^{206}Pb, calculated from the observed ^{204}Pb.
[d] Disc. = U–Pb discordance; difference between the ^{204}Pb-corrected $^{206}Pb/^{238}U$ and $^{207}Pb/^{206}Pb$ ages.

Raman band FWHMs and birefringence values (Table 2) corresponds well to the relation described by Palenik et al. (2003).

The time-integrated alpha fluences listed in Table 2 were calculated for self-irradiation periods matching the calculated upper and lower intercept ages on the Concordia plot. The observed degrees of radiation damage (estimated from Raman band FWHMs and birefringence) are clearly higher than it would correspond to self-irradiation over a 266 myr period (Fig. 6). For instance, zircon micro-areas that have experienced $3–6 \times 10^{15}$ alpha-decay events per mg of material should be expected to be moderately damaged, with birefringence higher than ≥0.020 (compare Equation 3 and Fig. 3 of Palenik et al. (2003) whereas the measured birefringence values are ≤0.004, indicating strong radiation damage (Table 2). Also, zircon that has experienced less than 1×10^{15} alpha-decay events per mg (cf. analyses 8 and 12 in Table 2) should yield $\nu_3(SiO_4)$ Raman band FWHMs smaller than 8 cm^{-1} (Nasdala et al., 2001) whereas much wider bands (14–25 cm^{-1}) were observed (Table 2; white circles in Fig. 6). Consequently, 266 myr alpha doses clearly underestimate the amount of radiation damage that is currently present. This observation indicates that the Saranac Prospect zircon cannot have experienced major structural reconstitution through thermal annealing of the previously existing radiation damage at Late Paleozoic times. On the other hand, the three SHRIMP spots in the unaltered, zoned zircon with the lowest degree of radiation damage (black circles in Fig. 6) are less radiation-damaged than it would correspond to complete damage accumulation since the time of crystal growth, indicating moderate post-growth thermal annealing. We conclude that Pb loss (and perhaps the second chemical alteration) must have occurred at low *T*, probably well below 200 °C. This estimate is based on results of Weber et al. (1994, 1997) and Meldrum et al. (1999) who predicted that long-term annealing of alpha-event damage is expected at temperatures as low as 150–200 °C.

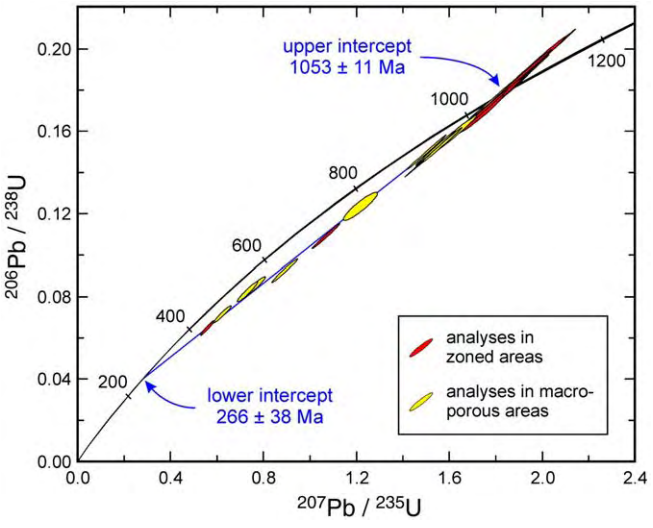

Fig. 5. Results of SHRIMP U–Pb analyses. Error ellipses represent 2σ uncertainties.

3.5. Further discussion

The chemical and physical alteration of the Saranac Prospect zircon was affected by two factors. First, the alteration was controlled by the accessibility of volume areas to the transporting phase, i.e.,

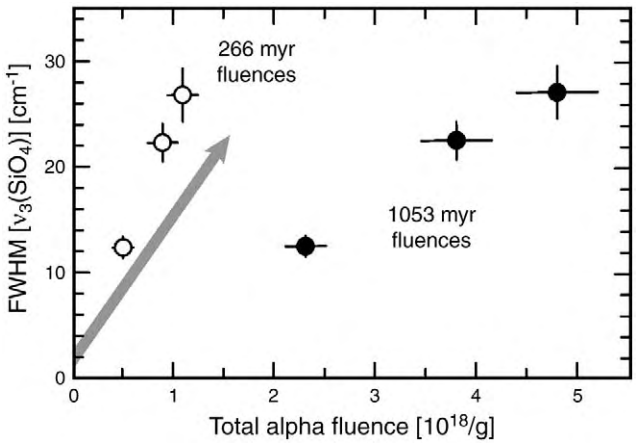

Fig. 6. Plot of Raman band FWHMs (indicating the degree of radiation damage) against time-integrated alpha fluences. The latter were calculated twice, for assumed damage accumulation periods corresponding to the calculated upper and lower intercept ages on the Concordia plot (Fig. 5). Data for the three SHRIMP spots with low to moderate degrees of radiation damage (Table 2) are compared to the trend defined by unannealed zircon samples (Nasdala et al., 2001; gray arrow). Areas are clearly more metamict than it would correspond to damage accumulation over a 266 myr period, which excludes complete thermal annealing in the Late Paleozoic.

hydrothermal fluids. Consequently, initial alteration during this phase is characterized by finger-like patterns along large fractures that have served as "fast pathways" (Figs. 2a–d). Also, alteration appears to be especially intense in the macro-porous zircon whose porosity may have aided circulation of the fluid. The crucial role of pathways is also indicated by varying degrees of U–Th–Pb isotopic discordance: the extent of secondary Pb loss is highly variable and it appears reasonable to speculate that Pb loss was strongly affected by the presence of migration pathways. Second, there are clear effects of the radiation damage. Near large fractures cross-cutting several growth zones, mostly the higher-U, more radiation-damaged zones are preferentially altered whereas the lower U, and less radiation-damaged zones, remained virtually unaffected (Fig. 2c, e, and f). Even though potential effects of variations of the chemical composition on the susceptibility of zircon to dissolution cannot be neglected, we interpret the different degrees of radiation damage among growth zones, resulting from varying initial U and Th concentrations, as the main reason for the different behavior among zones. This agrees very well with the conclusions in Davis and Krogh (2000) and Lumpkin (2001) who assigned fluid-driven alteration to metamictization and concluded that chemical control alone was insignificant. We did not find clear evidence for strain or other effects of mechanical deformation (cf. Timms et al., 2006) affecting the leaching and U retention properties of zircon.

The observations made in the present study correspond well to findings of Lee (1993) who discussed that radiation damage alone does not cause U–Th–Pb isotopic discordance through Pb loss from zircon; rather element and fluid transport along major pathways and chemical leaching are the two dominant cation exchange processes in radiation-damaged minerals. The observation that high-BSE areas in the Saranac Prospect zircon are (close to) concordant, even though being highly radiation-damaged, whereas intensely altered, low-BSE areas tend to have experienced notable Pb loss, suggests that a fluid-driven ion-exchange reaction either causes Pb loss, or strongly enhances the susceptibility of zircon to the subsequent loss of the radiogenic Pb (cf. Krogh and Davis, 1973, 1975).

In contrast to strong variations in radiogenic Pb, the primary U that was incorporated in the zircon structure has remained only mildly affected by the replacement reaction. This is clearly observable if the chemical analyses placed in unaltered and altered regions of the very same growth zone are compared (see zones B, C, D, E, G. H, I, and J in Table 1). The ratios between the content in an altered area and its unaltered counterpart were found to vary in the range 0.87–0.98 (average 0.95 ± 0.04) for ZrO_2, 0.92–0.98 (average 0.95 ± 0.02) for SiO_2, and 0.76–1.16 (average 0.94 ± 0.14) for UO_2, respectively. These average ratios reflect the typical moderate loss of chemical constituents in fluid-driven replacement reactions (cf. Putnis, 2002). Most remarkable, however, is the observation that the U loss is within errors identical to the losses of Zr and Si. The chemical alteration these zircon crystals have experienced has clearly not resulted in preferential leaching of U; rather Zr, Si, and U have been uniformly incorporated in the newly formed zircon. The latter is also strikingly apparent in the preservation of primary U zoning in alteration-overprinted areas (see U distribution maps in Fig. 4a, b). In summary, the multiple, low-*T* chemical alteration of the Saranac Prospect zircon has finally resulted in highly variable loss, of up to 80%, of the radiogenic Pb accumulated since primary crystallization and prior to the last closure of the U–Pb system (cf. again Table 2) whereas there were only minor U losses.

4. Conclusions

If zircon is in the presence of chemically aggressive hydrothermal fluids, for extended periods of time, then an essential question to answer (with regard to both its use in geochronology or as a potential nuclear waste repository material) is, to what degree the radionuclides are preferentially removed? In the present study, we show with the example of naturally altered zircon crystals from Bancroft, Ontario, that extensive low-*T* chemical replacement does not necessarily result in preferential leaching of U from strongly radiation-damaged zircon. This seems to question the general relevance of hydrothermal treatment experiments to a reliable assessment of the (self-irradiation dependent) long-term behavior of zircon and other actinide host materials under moderately "wet", low-*T* environmental conditions. The finding that zircon, under certain environmental conditions, has high ability to retain its trace uranium, might affect the interpretation of radiometric dating results, in particular discussions of possible causes of U–Pb discordance. Second, observations suggest that zircon, and even radiation-damaged zircon, may be a suitable ceramic waste form for the long-term immobilization and storage of radionuclides.

Acknowledgments

The SHRIMP II ion microprobe used in this study is operated by a consortium consisting of Curtin University of Technology, the University of Western Australia, and the Geological Survey of Western Australia. The SHRIMP reference zircon M257 was made available by W. Hofmeister (Institute of Gemstone Research, Idar-Oberstein and Mainz, Germany). We are indebted to D. Moser (University of Western Ontario, London) for providing the original zircon sample to J.M.H. in 1997, and to Robert Ramik (Royal Ontario Museum, Toronto) for providing additional information on the zircon sample and its origin. We thank A. Wagner (Universität Wien) for sample preparation, E. Libowitzky and K. Ruschel (both Universität Wien) for experimental assistance, and D.W. Davis (University of Toronto) for constructive discussions. Also, we are grateful to two anonymous reviewers and associate editor B. Bourdon for helpful comments. Financial support was provided by the European Commission through contract no. MEXC-CT-2005-024878 and the Austrian Science Fund (FWF), grant P20028-N10, to L.N.

References

Armstrong, J.T., 1995. CITZAF: a package of correction programs for the quantitative electron microbeam X-ray analysis of thick polished materials, thin films, and particles. Microbeam Analysis 4, 177–200.

Ashwal, L.D., Tucker, R.D., Zinner, E.K., 1999. Slow cooling of deep crustal granulites and Pb-loss in zircon. Geochimica et Cosmochimica Acta 63, 2839–2851.

Black, L.P., 1987. Recent Pb loss in zircon: a natural or laboratory-induced phenomenon? Chemical Geology (Isotope Geoscience Section) 65, 25–33.

Breiter, K., Förster, H.-J., Škoda, R., 2006. Extreme P-, Bi-, Nb-, Sc-, U- and F-rich zircon from fractionated perphosphorous granites: the peraluminous Podlesí granite system, Czech Republic. Lithos 88, 15–34.

Caruba, R., Mano, J., Dors, R., Turco, G., 1974. Corrosions expérimentales de critaux de zircons et comparaison avec des corrosions naturelles de zircons de granites albitisés. Tschermaks Mineralogische und Petrologische Mitteilungen 21, 33–46.

Chakoumakos, B.C., Murakami, T., Lumpkin, G.R., Ewing, R.C., 1987. Alpha-decay-induced fracturing in zircon: the transition from the crystalline to the metamict state. Science 236, 1556–1559.

Cherniak, D.J., Watson, E.B., 2001. Pb diffusion in zircon. Chemical Geology 172, 5–24.

Cherniak, D.J., Watson, E.B., 2003. Diffusion in zircon. In: Hanchar, J.M., Hoskin, P.W.O. (Eds.), Zircon. Reviews in Mineralogy and Geochemistry 53. Mineralogical Society of America, Washington, DC, pp. 113–143.

Compston, W., Williams, I.S., Meyer, C., 1984. U–Pb geochronology of zircon from lunar breccia 73217 using a sensitive high mass-resolution ion microprobe. Journal of Geophysical Resources 89, 525–534.

Compston, W., Kinny, P.D., Williams, I.S., Foster, J.J., 1986. The age and Pb loss behaviour of zircons from the Isua supracrustal belt as determined by ion microprobe. Earth and Planetary Science Letters 80, 71–81.

Connelly, J.N., 2000. Degree of preservation of igneous zonation in zircon as a signpost for concordancy in U/Pb geochronology. Chemical Geology 172, 25–39.

Corfu, F., 1987. Inverse age stratification in the archaean crust of the superior province: evidence for infra- and subcrustal accretion from high resolution U–Pb zircon and monazite ages. Precambrian Research 36, 259–275.

Corfu, F., Hanchar, J.M., Hoskin, P.W.O., Kinny, P., 2003. Atlas of zircon textures. In: Hanchar, J.M., Hoskin, P.W.O. (Eds.), Zircon. Reviews in Mineralogy and Geochemistry 53. Mineralogical Society of America, Washington, DC, pp. 469–500.

Davis, D.W., Krogh, T.E., 2000. Preferential dissolution of 234U and radiogenic Pb from α-recoil-damaged lattice sites in zircon: implications for thermal histories and Pb isotopic fractionation in the near surface environment. Chemical Geology 172, 41–58.

Davis, D.W., Williams, I.S., Krogh, T.E., 2003. Historical development of zircon geochronology. In: Hanchar, J.M., Hoskin, P.W.O. (Eds.), zircon. Reviews in Mineralogy and Geochemistry 53. Mineralogical Society of America, Washington, DC, pp. 145–181.

Dawson, P., Hargreave, M.M., Wilkinson, G.R., 1971. The vibrational spectrum of zircon ($ZrSiO_4$). Journal of Physics C: Solid State Physics 4, 240–256.

De Laeter, J.R., Kennedy, A.K., 1998. A double focussing mass spectrometer for geochronology. International Journal of Mass Spectrometry and Ion Processes 178, 43–50.

Ewing, R.C., 1994. The metamict state: 1993—the centennial. Nuclear Instruments and Methods in Physics Research Section B: Beam Interactions with Materials and Atoms 91, 22–29.

Ewing, R.C., 1999. Nuclear waste form for actinides. Proceedings of the National Academy of Sciences of the United States of America 96, 3432–3439.

Ewing, R.C., 2001. The design and evaluation of nuclear-waste forms: clues from mineralogy. Canadian Mineralogist 39, 697–715.

Ewing, R.C., Meldrum, A., Wang, L., Weber, W.J., Corrales, L.R., 2003. Radiation effects in zircon. In: Hanchar, J.M., Hoskin, P.W.O (Eds.), Zircon. Reviews in Mineralogy and Geochemistry 53. Mineralogical Society of America, Washington, DC, pp. 387–425.

Geisler, T., Pidgeon, R.T., von Bronswijk, W., Kurtz, R., 2002. Transport of uranium, thorium, and lead in metamict zircon under low-temperature hydrothermal conditions. Chemical Geology 191, 141–154.

Geisler, T., Rashwan, A.A., Rahn, M.K.W., Poller, U., Zwingmann, H., Pidgeon, R.T., Schleicher, H., Tomaschek, F., 2003. Low-temperature hydrothermal alteration of natural metamict zircon from the Eastern Desert, Egypt. Mineralogical Magazine 67, 485–508.

Geisler, T., Schleicher, H., Kurtz, R., van Bronswijk, W., Schleicher, H., 2003. Experimental hydrothermal alteration of partially metamict zircon. American Mineralogist 88, 1496–1513.

Gentry, R.V., Sworski, T.J., Mckown, H.S., Smith, D.H., Eby, R.E., Christie, W.H., 1982. Differential lead retention in zircons: implications for nuclear waste containment. Science 216, 296–298.

Hansen, B.T., Friderichsen, J.D., 1989. The influence of recent lead loss on the interpretation of disturbed U–Pb systems in zircons from igneous rocks in East Greenland. Lithos 23, 209–223.

Hoskin, P.W.O., 2000. Patterns of chaos: fractal statistics and the oscillatory chemistry of zircon. Geochimica et Cosmochimica Acta 64, 1905–1923.

Jaffey, A.H., Flynn, K.F., Glendenin, L.E., Bentley, W.C., Essling, A.M., 1971. Precision measurement of half-lives and specific activities of ^{235}U and ^{238}U. Physical Review C 4, 1889–1906.

Johan, Z., Johan, V., 2005. Accessory minerals of the Cínovec (Zinnwald) granite cupola, Czech Republic: indicators of petrogenetic evolution. Mineralogy and Petrology 83, 113–150.

Keller, L.M., Wirth, R., Rhede, D., Kunze, K., Abart, R., 2008. Asymmetrically zoned reaction rims: assessment of grain boundary diffusivities and growth rates related to natural diffusion-controlled mineral reactions. Journal of Metamorphic Geology 26, 99–120.

Krogh, T.E., 1993. High precision U–Pb ages for granulite metamorphism and deformation in the Archean Kapuskasing structural zone, Ontario: implications for structure and development of the lower crust. Earth and Planetary Science Letters 119, 1–18.

Krogh, T.E., Davis, G.L., 1973. Alteration in zircons with discordant U–Pb ages. Year book / Carnegie Institution of Washington 73, 560–567.

Krogh, T.E., Davis, G.L., 1975. Alteration in zircons and differential dissolution of altered and metamict zircon. Year book / Carnegie Institution of Washington 74, 619–623.

Labotka, T.C., Cole, D.R., Fayek, M., Riciputi, L.R., Stadermann, F.J., 2004. Coupled cation and oxygen–isotope exchange between alkali feldspar and aqueous chloride solution. American Mineralogist 89, 1822–1825.

Lakis, R., Lyman, C., Goldstein, J., 1992. Electron-probe microanalysis of porous materials. 50th Annual Meeting of the Electron Microscopy Society of America. Proceedings, pp. 1660–1661.

Lee, J.K.W., 1993. Problems and progress in the elucidation of U and Pb transport mechanisms in zircon. In: Boland, J.N., Fitz Gerald, J.D. (Eds.), Defects and processes in the solid state: Geoscience applications. The McLaren Volume. Elsevier, pp. 423–446.

Lee, J.K.W., Tromp, J., 1995. Self-induced fracture generation in zircon. Journal of Geophysical Research - Solid Earth 100, 17753–17770.

Ludwig, K.R., 2002. SQUID 1.02, a user's manual: Berkeley Geochronology Center Special Publication 2. 22 pp.

Ludwig, K.R., 2003. User's manual for Isoplot 3.00. A geochronological toolkit for Microsoft Excel: Berkeley Geochronology Center Special Publication 4. 71 pp.

Lumpkin, G.R., 2001. Alpha-decay damage and aqueous durability of actinide host phases in natural systems. Journal of Nuclear Materials 289, 136–166.

Lumpkin, G.R., 2006. Ceramic waste forms from actinides. Elements 2, 365–372.

Mathieu, R., Zetterström, L., Cuney, M., Gauthier-Lafaye, F., Hidaka, H., 2001. Alteration of monazite and zircon and lead migration as geochemical tracers of fluid paleocirculations around the Oklo-Okélobondo and Bangombé natural nuclear reaction zones (Franceville basin, Gabon). Chemical Geology 171, 147–171.

Mattinson, J.M., 1994. A study of complex discordance in zircons using step-wise dissolution techniques. Contributions to Mineralogy and Petrology 116, 117–129.

Mattinson, J.M., 2005. Zircon U–Pb chemical abrasion ("CA-TIMS") method: combined annealing and multi-step partial dissolution analysis for improved precision and accuracy of zircon ages. Chemical Geology 220, 47–66.

McLaren, A.C., Fitz Gerald, J.D., Williams, I.S., 1994. The microstructure of zircon and its influence on the age determination from Pb/U isotopic ratios measured by ion microprobe. Geochimica et Cosmochimica Acta 58, 993–1005.

Meldrum, A., Boatner, L.A., Zinkle, S.J., Wang, S.-X., Wang, L.-M., Ewing, R.C., 1999. Effects of dose rate and temperature on the crystalline-to-metamict transformation in the ABO_4 orthosilicates. Canadian Mineralogist 37, 207–221.

Morgan, J.H., Auer, M.L., 1941. Optical, spectrographic, and radio-activity studies of zircon. American Journal of Science 239, 305–311.

Murakami, T., Chakoumakos, B.C., Ewing, R.C., Lumpkin, G.R., Weber, W.J., 1991. Alpha-decay event damage in zircon. American Mineralogist 76, 1510–1532.

Nasdala, L., Irmer, G., Wolf, D., 1995. The degree of metamictization in zircon: a Raman spectroscopic study. European Journal of Mineralogy 7, 471–478.

Nasdala, L., Wenzel, T., Pidgeon, R.T., Kronz, A., 1999. Internal structures and dating of complex zircons from Meissen Massif monzonites, Saxony. Chemical Geology 156, 331–341.

Nasdala, L., Wenzel, M., Vavra, G., Irmer, G., Wenzel, T., Kober, B., 2001. Metamictisation of natural zircon: accumulation versus thermal annealing of radioactivity-induced damage. Contributions to Mineralogy and Petrology 141, 125–144.

Nasdala, L., Lengauer, C.L., Hanchar, J.M., Kronz, A., Wirth, R., Blanc, P., Kennedy, A.K., Seydoux-Guillaume, A.-M., 2002. Annealing radiation damage and the recovery of cathodoluminescence. Chemical Geology 191, 121–140.

Nasdala, L., Hanchar, J.M., Kronz, A., Whitehouse, M.J., 2005. Long-term stability of alpha particle damage in natural zircon. Chemical Geology 220, 83–103.

Nasdala, L., Hofmeister, W., Norberg, N., Mattinson, J.M., Corfu, F., Dörr, W., Kamo, S.L., Kennedy, A.K., Kronz, A., Reiners, P.W., Frei, D., Kosler, J., Wan, Y., Götze, J., Häger, T., Kröner, A., Valley, J.W., 2008. Zircon M257—a homogeneous natural reference material for the ion microprobe U–Pb analysis of zircon. Geostandards and Geoanalytical Research 32, 247–265.

Nasdala, L., Kronz, A., Wirth, R., Váczi, T., Pérez-Soba, C., Willner, A., Kennedy, A.K., 2009. Alteration of radiation-damaged zircon and the related phenomenon of deficient electron microprobe totals. Geochimica et Cosmochimica Acta 73, 1637–1650.

Palenik, C.S., Nasdala, L., Ewing, R.C., 2003. Radiation damage in zircon. American Mineralogist 88, 770–781.

Pérez-Soba, C., Villaseca, C., Gonzáles del Tánago, J., Nasdala, L., 2007. The composition of zircon in the peraluminous Hercynian granites of the Spanish Central System batholith. Canadian Mineralogist 45, 509–527.

Peterman, Z.E., Zartman, R.E., Sims, P.K., 1986. A protracted Archean history in the Watersmeet gneiss dome, northern Michigan. U.S. Geological Survey Bulletin 1622, 51–64.

Pidgeon, R.T., O'Neil, J.R., Silver, L.T., 1966. Uranium and lead isotope stability in a metamict zircon under experimental hydrothermal conditions. Science 154, 1538–1540.

Pointer, C.M., Ashworth, J.R., Ixer, R.A., 1988. The zircon-thorite mineral group in metasomatized granite, Ririwai, Nigeria. 2. Zoning, alteration and exsolution in zircon. Mineralogy and Petrology 39, 21–37.

Pöml, P., Meneken, M., Stephan, T., Niedermeier, D.R.D., Geisler, T., Putnis, A., 2007. Mechanism of hydrothermal alteration of natural self-irradiated and synthetic crystalline titanate-based pyrochlore. Geochimica et Cosmochimica Acta 71, 3311–3322.

Prasad, E.A.V., Naidu, M.G.C., 1971. Leaching patterns of monazite and zircon. Current Science 40, 14–15.

Putnis, A., 2002. Mineral replacement reactions: from macroscopic observations to microscopic mechanisms. Mineralogical Magazine 66, 689–708.

Putnis, C., Geisler, T., Schmid-Beurmann, P., Stephan, T., Giampaolo, C., 2007. An experimental study of the replacement of leucite by analcime. American Mineralogist 92, 19–26.

Rimša, A., Whitehouse, M.J., Johansson, L., Piazolo, S., 2007. Brittle fracturing and fracture healing of zircon: an integrated cathodoluminescence, EBSD, U–Th–Pb, and REE study. American Mineralogist 92, 1213–1224.

Please cite this article as: Nasdala, L., et al., Retention of uranium in complexly altered zircon: An example from Bancroft, Ontario, Chemical Geology (2009), doi:10.1016/j.chemgeo.2009.10.004

Rizvanova, N.G., Levchenkov, O.A., Belous, A.E., Bezmen, N.I., Maslenikov, A.V., Komarov, A.N., Makeev, A.F., Levskiy, L.K., 2000. Zircon reaction and stability of the U–Pb isotope system during interaction with carbonate fluid: experimental hydrothermal study. Contributions to Mineralogy and Petrology 139, 101–114.

Romer, R.L., 2003. Alpha-recoil in U–Pb geochronology: effective sample size matters. Contributions to Mineralogy and Petrology 145, 481–491.

Sahama, T.G., 1981. Growth structure in Ceylon zircon. Bulletin de Minéralogie 104, 89–94.

Satterly, J, 1957. Radioactive mineral occurrences in the Bancroft area. Ontario Department of Mines: Annual Report 1956, 65 (part 6), pp. 108–115.

Schoene, B., Crowley, J.L., Condon, D.J., Schmitz, M.D., Bowring, S.A., 2006. Reassessing the uranium decay constants for geochronology using ID-TIMS U–Pb data. Geochimica et Cosmochimica Acta 70, 426–445.

Shukolyukov, Yu.A., Prevdivtseva, A.V., Kotov, N.V., 1994. The U–Pb and U–Xe isotope systems in metamict zircons at elevated T and P. Geochemistry International 31, 65–72.

Sinha, A.K., Wayne, D.W., Hewitt, D.A., 1992. The hydrothermal stability of zircon: preliminary experimental and isotopic studies. Geochimica et Cosmochimica Acta 56, 3551–3560.

Sláma, J., Košler, J., Condon, D.J., Crowley, J.L., Gerdes, A., Hanchar, J.M., Horstwood, M.S.A., Morris, G.A., Nasdala, L., Norberg, N., Schaltegger, U., Tubrett, M.N., Whitehouse, M.J., 2008. Plešovice zircon—a new natural reference material for U–Pb and Hf isotopic microanalysis. Chemical Geology 249, 1–35.

Smith, D.G.W., Smith, D.G.W., de St. Jorre, L., Reed, S.J.B., Long, J.V.P., 1991. Zonally metamictized and other zircons from Thor Lake, Northwest Territories. Canadian Mineralogist 29, 301–309.

Sorbier, L., Rosenberg, E., Merlet, C., 2004. Microanalysis of porous materials. Microscopy and Microanalysis 10, 745–752.

Timms, N.E., Kinny, P.D., Reddy, S.M., 2006. Enhanced diffusion of uranium and thorium linked to crystal plasticity in zircon. Geochemical Transactions 7, 10.

Tole, M.P., 1985. The kinetics of dissolution of zircon ($ZrSiO_4$). Geochimica et Cosmochimica Acta 49, 453–458.

Tomaschek, F., Kennedy, A.K., Villa, I.M., Lagos, M., Ballhaus, C., 2003. Zircons from Syros, Cyclades, Greece—recrystallization and mobilization of zircon during high-pressure metamorphism. Journal of Petrology 44, 1977–2002.

Törnroos, R., 1985. Metamict zircon from Mozambique. Bulletin of the Geological Society of Finland 57, 181–195.

Tröger, W.E., 1982. Optical determination of rock-forming minerals. I. Determinative tables. E. Schweitzerbart'sche Verlagsbuchhandlung, Stuttgart. 188 pp.

Utsunomiya, S., Valley, J.W., Cavosie, A.J., Wilde, S.A., Ewing, R.C., 2007. Radiation damage and alteration of zircon from a 3.3 Ga porphyritic granite from the Jack Hills, Western Australia. Chemical Geology 236, 92–111.

Van Lichtervelde, M., Melcher, F., Wirth, R., 2009. Magmatic vs. hydrothermal origins for zircon associated with tantalum mineralization in the Tanco pegmatite, Manitoba, Canada. American Mineralogist 94, 439–450.

Weber, W.J., Ewing, R.C., Wang, L.-M., 1994. The radiation-induced crystalline-to-amorphous transition in zircon. Journal of Materials Research 9, 688–698.

Weber, W.J., Ewing, R.C., Meldrum, A., 1997. The kinetics of alpha-decay-induced amorphization in zircon and apatite containing weapons-grade plutonium or other actinides. Journal of Nuclear Materials 250, 147–155.

Weber, W.J., Ewing, R.C., Catlow, C.R.A., Diaz de la Rubia, T., Hobbs, L.W., Kinoshita, C., Matzke, H., Motta, A.T., Nastasi, M., Salje, E.K.H., Vance, E.R., Zinkle, S.J., 1998. Radiation effects in crystalline ceramics for the immobilization of high-level nuclear waste and plutonium. Journal of Materials Research 13, 1434–1484.

Williams, I.S., Compston, W., Black, L.P., Ireland, T.R., Foster, J.J., 1984. Unsupported radiogenic Pb in zircon: a cause of anomalously high Pb–Pb, U–Pb and Th–Pb ages. Contributions to Mineralogy and Petrology 88, 322–327.

Williams, I.S., Hergt, J.M., 2000. U–Pb dating of Tasmanian dolerites: a cautionary tale of SHRIMP analysis of high U zircon. In: Woodhead, J.D., Hergt, J.M., Noble, W.P. (Eds.), Beyond 2000: New frontiers in isotope geoscience, Lorne, Australia. Abstracts and Proceedings, pp. 185–188.

Please cite this article as: Nasdala, L., et al., Retention of uranium in complexly altered zircon: An example from Bancroft, Ontario, Chemical Geology (2009), doi:10.1016/j.chemgeo.2009.10.004

Appendix 4

Váczi, T., Nasdala, L., Wirth, R., Mehofer, M., Libowitzky, E. & Häger, T. (2009): On the breakdown of zircon upon “dry” thermal annealing. *Mineralogy and Petrology*, **97/1–2:** 129–138.

Miner Petrol (2009) 97:129–138
DOI 10.1007/s00710-009-0087-9

ORIGINAL PAPER

On the breakdown of zircon upon "dry" thermal annealing

Tamás Váczi · Lutz Nasdala · Richard Wirth · Mathias Mehofer · Eugen Libowitzky · Tobias Häger

Received: 14 August 2008 / Accepted: 5 October 2009 / Published online: 17 October 2009

Abstract Zircon samples without and with secondary chemical alteration from diverse sources were subjected to heat treatment at 1400 °C for 96 h. Resulting new phases and textures suggest that decomposition of zircon into component oxides occurred in all experiments to various degrees. The crucible material was found to have a strong influence on the extent of breakdown, especially in the case of altered starting materials. In this study the progressive stages of the breakdown of zircon grains are described. The factors that may govern the decomposition are discussed, including radiation damage, secondary alteration and external reaction conditions (sample container, atmosphere). Alumina crucibles should generally be avoided in dry annealing of zircon, to minimise uncontrolled breakdown into oxides.

Editorial handling: A. Möller

T. Váczi (✉) · L. Nasdala · E. Libowitzky
Institut für Mineralogie und Kristallographie, Universität Wien,
Althanstraße 14,
1090 Wien, Austria
e-mail: tamas.vaczi@univie.ac.at

L. Nasdala
e-mail: lutz.nasdala@univie.ac.at

E. Libowitzky
e-mail: eugen.libowitzky@univie.ac.at

R. Wirth
Helmholtz-Zentrum Potsdam, Deutsches GeoForschungsZentrum,
Telegrafenberg,
14473 Potsdam, Germany
e-mail: wirth@gfz-potsdam.de

M. Mehofer
Vienna Institute for Archaeological Science (VIAS),
Universität Wien,
Franz Klein-Gasse 1,
1190 Wien, Austria
e-mail: mathias.mehofer@univie.ac.at

T. Häger
Institut für Geowissenschaften,
Johannes Gutenberg-Universität Mainz,
Saarstr. 21,
55099 Mainz, Germany
e-mail: tobias.haeger@uni-mainz.de

Introduction

Zircon, $ZrSiO_4$, is a common accessory mineral found in a wide range of igneous and metamorphic rocks. It is the most important mineral for U/Th–Pb geochronology because (i) zircon is an extremely robust container for parent U and Th and daughter isotopes through geologic time and (ii) this mineral mostly excludes Pb at primary growth. For industrial purposes, zircon is a widely used refractory material for high-temperature applications such as furnace linings, barrier coatings, ceramic pigments etc. In addition, zircon is the primary source for zirconium and zirconia (ZrO_2).

Natural zircon has generally a non-ideal structure and composition, and industrial zircon is often processed, perhaps purified, natural zircon (see e.g. Pavlik et al. 2001). Depending on age, thermal history and actinide concentration, natural zircon has a certain level of accumulated radiation damage. The expected high-temperature behaviour of radiation-damaged (but not fully amorphised) zircon is a gradual restoration of short and long-range order (e.g. McLaren et al. 1994; Colombo and Chrosch 1998; Colombo et al. 1999; Begg et al. 2000; Capitani et al. 2000; Zhang et al. 2000; Nasdala et al. 2001; Geisler 2002; Nasdala et al. 2004). In contrast, the structural reconstitution of fully metamict zircon upon dry heating involves an

intermediate stage of ZrO_2 formation between 800 and 1100 °C, prior to the formation of crystalline zircon at above ca. 1150 °C (Mitsuhashi et al. 1974; Ellsworth et al. 1994; Zhang et al. 2000; Nasdala et al. 2002).

Pure, undamaged zircon is predicted to be stable up to ca. 1676 °C (e.g. Butterman and Foster 1967), at which point it decomposes into oxides. However, it is far from uncommon to observe that zircon breaks down at temperatures well below the thermodynamically predicted decomposition temperature. There appears to be no well-defined temperature for the onset of decomposition. Peña and de Aza (1984) and Kaiser et al. (2008) compiled zircon decomposition temperatures from the literature, ranging from 1400 °C to 2000 °C, but cited reports of incongruent melting at higher temperatures as well.

High-temperature treatment of zircon is done for various reasons in radioactive dating methods as well. The zircon whole-grain evaporation method (Kober 1986, 1987) utilises the decomposition of zircon into oxides (ZrO_2 + SiO_2) at elevated temperatures, where Pb is removed from zircon through the volatilisation of the silica component. Zircon evaporation is carried out on grains wrapped in inert rhenium filaments under vacuum (at ca. 1400–1500 °C). The "chemical abrasion" technique (multi-step leaching and thermal ionisation mass spectroscopy of whole zircon grains, CA-TIMS; Mattinson 2005) involves thermal preconditioning, prior to multi-step partial dissolution analysis, in order to partially stabilise radiation-damaged domains for a better-controlled etching behaviour. For this, Mattinson (2005) suggested to do heat treatment in air in alumina crucibles, at 800–1100 °C for 48 h. Note, however, that most geochronology laboratories seem to use SiO_2 crucibles instead of alumina.

This paper presents results of annealing experiments aimed to observe the progress of the breakdown of zircon. In our study the temperature for heat treatment was chosen at 1400 °C. This temperature is within the reported range of decomposition temperatures, high enough to anneal radiation damage (not studied here), yet significantly below the thermodynamically expected decomposition temperature of zircon. We attempt to evaluate factors influencing the decomposition behaviour of zircon, with special attention to chemical alteration of radiation-damaged domains. The role of thermal breakdown in age determination methods involving high-temperature treatment is discussed.

Materials and methods

Table 1 gives a summary of materials and experiments in this study. Three types of samples were included. First, we studied pure (undoped), synthetic zircon single crystals (1–2 mm), grown using the Li–Mo flux method (Hanchar et al. 2001). Second, fragments (0.5–2 mm) of well-characterised, inclusion-free zircon crystals were also studied, including the 1064 Ma old sample 91500 from Ontario, Canada (Wiedenbeck et al. 2004), and the late Precambrian–Cambrian gemstones M257, M127 (Nasdala et al. 2008), M146 and M144 (Nasdala et al. 2004) from Sri Lanka. In addition, zircon grains (sample 87165; Pérez-Soba et al. 2007) from a coarse-grained leucogranite of the Hercynian La Pedriza pluton, Spanish Central System batholith, were also studied. This zircon was heavily altered by secondary hydrothermal processes, and consequently it is chemically impure, significantly hydrated and has a large number of pores and mineral inclusions (Nasdala et al. 2009).

Small (0.5–1 mm) euhedral grains or chips of larger crystals were heated in either platinum or sintered Al_2O_3 crucibles. The crucibles were covered with a lid of the same material and placed in a larger alumina crucible to further reduce the exchange of gaseous species between crucible and furnace atmosphere. The samples were heated at 1400 °C in high-temperature furnaces for 96 h. The heating rate was typically ca. 50 °C/min (fast heat-up). The furnaces were equipped with type B thermocouples, temperature was regulated by the built-in controllers, the temperature accuracy was better than 50 °C. After 96 h the furnaces were switched off. Samples were removed only after the furnaces had cooled to room temperature. An attempt was made to check the effect of the rate of heat-up: a set of unaltered samples (Table 1) was subjected to annealing with a very flat ramp (1 °C/min) in a Pt crucible.

Following heat treatment, outer surfaces of the samples were imaged on uncut grains. Some grains were then embedded in araldite epoxy, ground to approximately half thickness and polished to reveal internal textures for scanning electron microscope (SEM) imaging. For transmission electron microscopy (TEM) analyses, electron transparent foils were prepared with the focused ion beam (FIB) technique (Wirth 2004).

Secondary electron (SE) and back-scattered electron (BSE) images of unprepared grains (i.e., no polishing and carbon coating) were taken in a LEO EVO 60 variable-pressure SEM, used in the low-vacuum mode. Epoxy-mounted samples were carbon coated and imaged using a JEOL JSM-6400 SEM. Sub-micrometer textures and compositions on FIB foils were studied with an FEI Tecnai G^2 F20 X-Twin analytical TEM operated at 200 kV in selected area electron diffraction (SAED), high-resolution (HRTEM) and scanning TEM (STEM) modes. For phase identification TEM and Raman spectroscopy were used. Raman spectra were acquired with a Renishaw RM1000 system in the quasi-confocal mode. The instrument was equipped with a Leica DMLM optical microscope, edge filter-based laser line rejection, an optical grating (1200

Table 1 Summary of sample materials and heat-treatment experiments

Zircon sample			Alpha dose[a]	References	Crucible material[b]	
Name	Origin	Character			50 °C/min	1 °C/min
syn		synthetic	0	Hanchar et al. (2001)	Pt, Al_2O_3	–
91500	Ontario, Canada	unaltered	0.33	Wiedenbeck et al. (2004)	Pt, Al_2O_3	Pt
M144	Sri Lanka	unaltered	0.88	Nasdala et al. (2004)	Pt, Al_2O_3	Pt
M257	Sri Lanka	unaltered	1.71	Nasdala et al. (2008)	Pt, Al_2O_3	Pt
M127	Sri Lanka	unaltered	1.83	Nasdala et al. (2008)	Pt, Al_2O_3	Pt
M146	Sri Lanka	unaltered	1.98	Nasdala et al. (2004)	Pt, Al_2O_3	Pt
87165	La Pedriza, Spain	altered	7–17	Pérez-Soba et al. (2007); Nasdala et al. (2009)	Pt, Al_2O_3	–

[a] Calculated doses, given in 10^{18} alpha events per gram. Values were extracted from the references quoted

[b] Materials: Pt—platinum, Al_2O_3—sintered alumina

grooves/mm), and a Si-based, Peltier-cooled CCD detector. The 632.8 nm emission of a He-Ne laser was used as the excitation source, and the elastic (Rayleigh) scattering was used for spectral calibration. The spectral resolution of the system was ca. 2.2 cm^{-1}; the wavenumber accuracy was better than 1 cm^{-1}. Modal composition and pore space estimates were obtained from BSE images using the ImageJ image processing and analysis program (available at http://rsbweb.nih.gov/ij/). The method is based on the assumption that the volume fractions of different phases or pore space are represented by the relative two-dimensional surface areas of greyscale shades measured on cross-sections.

Results

All samples display, though to largely varying degrees, evidence of reactions after the heat treatment, partly on outer surfaces and partly also internally. Zirconium oxide as a reaction product has been observed in all samples after heat treatment. The monoclinic polytype (baddeleyite) has been identified at room temperature using Raman spectroscopy (Fig. 1) and TEM (electron diffraction and chemical analysis). Zirconia shows pronounced polysynthetic twinning (Fig. 2b), suggesting a transformation from a higher-symmetry polymorph upon cooling. Tetragonal ZrO_2 has not been observed.

Silica has been found in the amorphous state, suggested by a diffuse ring in the TEM SAED patterns. TEM chemical point analysis reveals that silica contains impurity elements (Mg, Ca, Al, P) in the percent range. SiO_2 is positively identified only in sample 87165, in Pt-annealed grains and in internal zones of alumina-annealed grains where a zircon matrix is found after heat treatment (Fig. 2a, c). A thin layer of an unidentified transparent material, seen as coloured interference fringes on a reflected-light optical microscope image, is observed in some reaction pits (e.g. on M257). Raman spectra recorded from these thin layers lack characteristic bands of any known SiO_2 polymorph, but show a very high luminescence background (and peaks from underlying zircon). The thickness of these layers is estimated from the interference colours (assuming refractive index $n = 1.5$) to be less than 0.5 µm.

No strong evidence for the presence of silica is found in most of the reaction pits on the surfaces or in zirconia

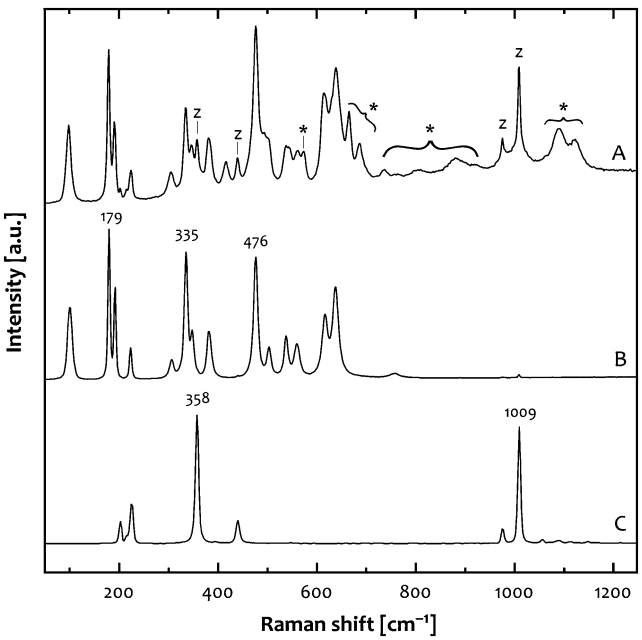

Fig. 1 Representative Raman spectra of decomposition products. **a** Typical spectrum recorded from a baddeleyite (monoclinic ZrO_2) microcrystal on the surface of an annealed grain (as in Fig. 3b). Underlying bulk zircon (bands labelled with "z") is also detected because of the moderate depth resolution of the Raman system used. Asterisks mark rare-earth luminescence artefacts from baddeleyite. Sample M257, fast heating, Al_2O_3 crucible. **b** Spectrum of pure baddeleyite from a porous crust (as in Fig. 3c). Synthetic sample, fast heating, Al_2O_3 crucible. (**c**) Zircon spectrum. Sample 91500, slow heating, Pt crucible (cf. Fig. 5b)

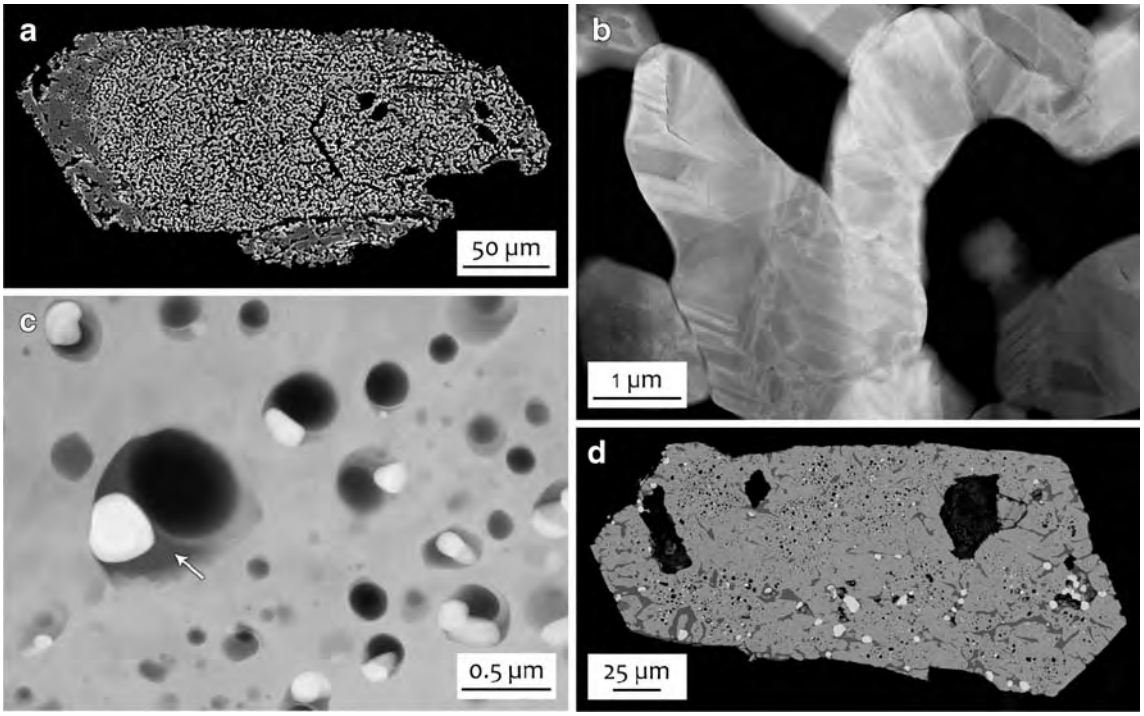

Fig. 2 The heavily altered La Pedriza zircon (sample 87165) after annealing. **a** Cross-section (SE image) of a grain annealed in an alumina crucible. The majority of the grain turned into a porous network of monoclinic zirconia (baddeleyite) while the silica component evaporated. The outer shape retains that of primary zircon. Note the recrystallised zircon zone, showing up in a darker tone on the left. **b** STEM image of a part of the zirconia network, cut out with FIB from the grain in (A). The lamellar fine contrast shows polysynthetic twinning. **c** STEM image of a FIB foil cut from the zircon rim of the grain in (A). White grains are baddeleyite, light grey areas are zircon. The arrow points to impure, amorphous silica. **d** BSE image of another grain, annealed in a Pt crucible. White dots are baddeleyite, mid-grey is zircon and dark grey patches are silica. The larger, angular, black areas are empty spaces left after inclusions (xenotime)

aggregates of heat-treated synthetic and unaltered samples (Figs. 3 and 4). Significant amounts of silica are "missing" from reaction zones that were in close contact with alumina crucibles. However, no reaction phase could be identified with Raman spectroscopy on the inner surface of the alumina crucibles at the sites of contact with the grains.

Decomposition textures have been observed either confined to outer surfaces or scattered throughout the volume of the grain. Surface breakdown has occurred in synthetic $ZrSiO_4$ and natural, unaltered zircon samples (syn, M127, M257, M144, M146 and 91500), while the hydrothermally altered La Pedriza zircon (sample 87165) exhibits oxide phases in the interior of the grains as well.

Synthetic $ZrSiO_4$ and unaltered zircon grains show only minor breakdown after being heated slowly (i.e., at ca. 50 °C/min) in Pt crucibles. The synthetic $ZrSiO_4$ sample

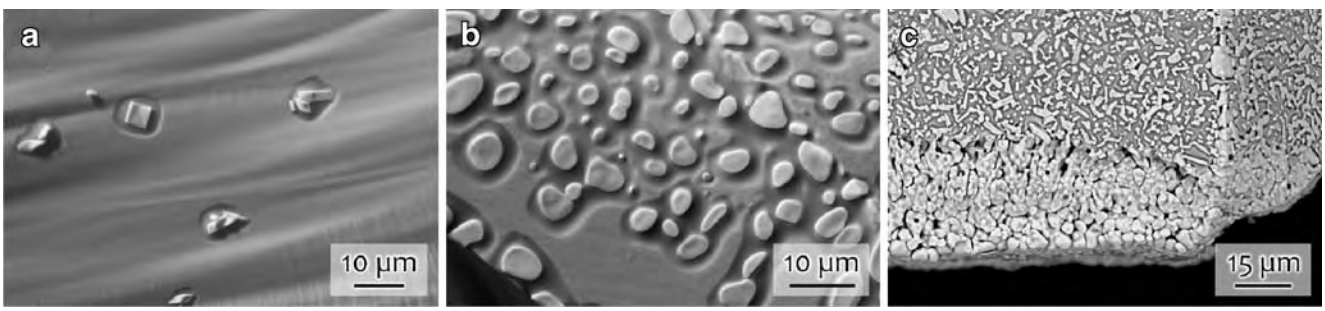

Fig. 3 Images showing the advance of surface corrosion of unaltered zircon (fast heating, alumina crucible). **a** Initial stage. Small pits (less than 0.5 µm deep) develop where zirconia crystals grow. Sample M127, SE image. **b** Intermediate stage. The pits fuse but zirconia crystals are still isolated. Sample M257, SE image. **c** Advanced stage. The breakdown reaction proceeds towards the inside of the zircon grain. Silica has evaporated and an aggregated zirconia rim develops. The bottom face of the crystal was in contact with the alumina crucible (see also Fig. 4). Synthetic $ZrSiO_4$ sample, BSE image

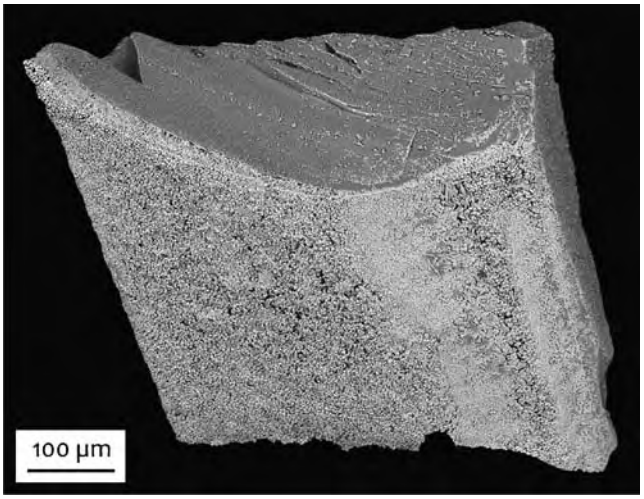

Fig. 4 BSE image of the M146 zircon gem fragment annealed in an alumina crucible. The side facing the page was in contact with the crucible and developed a porous baddeleyite crust. Note the highly accelerated breakdown (up to 30 µm away from the surface) on this side, while other sides of the grain display only point corrosion

displays a great number of very small (<2 µm) reaction pits, whereas the natural grains have very few, slightly larger (up to 10 µm), isolated reaction pits on the grain surfaces. Somewhat different textures have developed after slow heating (ca. 1 °C/min) of the unaltered samples in a Pt crucible. There is again only minor breakdown, and all of the annealed fragments show zirconia grains that lie near the grain surfaces. However, some of these zirconia crystals are found underneath a thin (<5 µm) layer of zircon, while the rest sit recessed into the surface (Fig. 5a–b; compare Fig. 3a–b). No perceptible difference between bulk zircon and the thin cover layer was detected on SEM images (BSE brightness, texture). No trace of silica is observed on polished cross-cuts (Fig. 5b).

Synthetic $ZrSiO_4$ and unaltered zircon samples annealed in alumina crucibles (fast heat-up) decompose more extensively, as shown in Fig. 3a–c. A peculiar feature is that a zirconia aggregate crust develops only on one side of the grain, namely on the side of the fragment, or face of the crystal, that was in physical contact with the crucible during annealing. After heating for 96 h, the reaction front (zircon–porous zirconia interface) has advanced 10–30 µm inwards from the original surface (Figs. 3c and 4). Note that on the same grains the faces that have not been in contact with alumina are sparsely covered with reaction pits and isolated zirconia grains.

From the observed abundance and extent of the breakdown that develops on outer surfaces (synthetic $ZrSiO_4$ and unaltered samples), the progressive stages of the process may be reconstructed. The decomposition of synthetic $ZrSiO_4$ and unaltered zircon during annealing usually starts at the outer surface and proceeds inwards (Figs. 3 and 4). The process starts with isolated, shallow pits on the surface, with a flat zirconia grain in the centre (Fig. 3a). As the decomposition proceeds, the pits grow laterally but not significantly in depth (Fig. 3b). The pits eventually merge and cover the entire surface, but the zirconia grains remain isolated. The further breakdown of zircon then advances away from the surface, and the zirconia grains are eventually sintered into a porous aggregate (Fig. 3c) when a zircon substrate supports them no longer. At this stage the reaction front proceeds inwards, roughly parallel to the surface, leaving a sponge-like zirconia network with very little or no silica. The breakdown may advance so far that the entire zircon material is consumed. The leftover zirconia aggregate retains the outer shape of the original zircon grain.

In annealed grains of sample 87165, the breakdown products are not limited to the surfaces. The zircon grains annealed (fast heat-up) in an alumina crucible show the

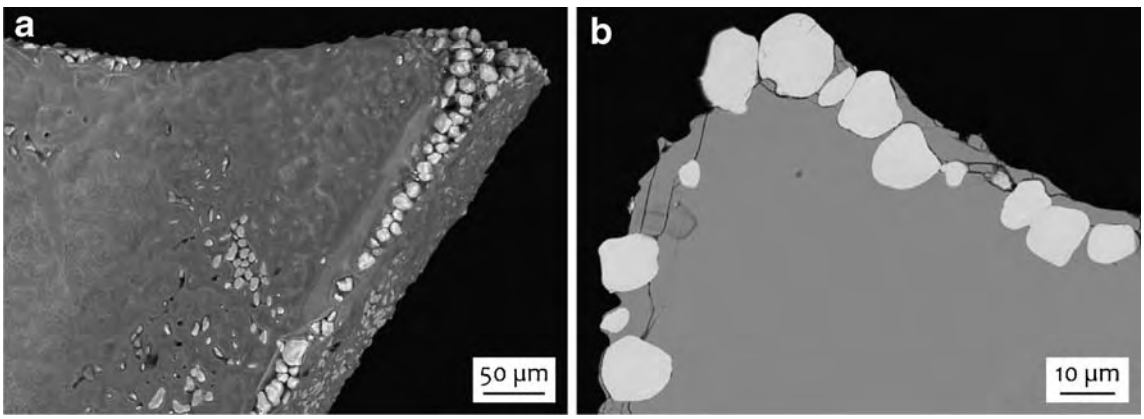

Fig. 5 Images of an annealed grain of sample 91500, after slow heating (1 °C/min) in a Pt crucible. **a** BSE image of the unprepared grain. The zirconia crystallites are partly embedded in the zircon and appear mostly at the edges. The zircon surface shows mottled contrast but no corrosion pits are seen, unlike in Fig. 3. **b** BSE image of a polished section of the grain in (A). Zirconia crystals (bright, rounded grains) are located somewhat below the zircon surface. There is no BSE intensity difference between bulk and cover zircon. Note that there is no visible trace of silica, and pore space is negligible

most extensive breakdown: 80–100 vol% of each grain consists of a sponge-like, porous network of monoclinic zirconia (Fig. 2a–b) without observable traces of silica. The volume ratio of zirconia to pore space is estimated to be close to 50:50, with ±5% error. In some, but not all, grains there are areas of irregular shape where zircon is observed after heat treatment (Fig. 2a). Electron diffraction patterns made on FIB foils cut from such zircon zones reveal polycrystalline zircon. The crystallites are not oriented, suggesting recrystallisation without major directional control by epitaxial growth. There are tiny (0.1–2 μm), round inclusions, scattered irregularly in the zircon matrix. The inclusions are filled with amorphous silica that covers the walls and hosts a rounded ZrO_2 grain. The centre of the inclusions is pore space (Fig. 2c).

Grains of sample 87165 annealed in a Pt crucible (fast heat-up) show a different internal texture. The formation of polycrystalline zircon is much more pronounced and coexisting silica glass and zirconia are also observed after the heat treatment (Fig. 2d). Zircon was identified in ca. 75–90% of the grain volume; the rest of the grains is made up of amorphous silica (8–17%), monoclinic zirconia (2–4%) and pore space (2–5%; Fig. 2d). (Note that these numbers are rough estimates, as the method used to derive them is strongly influenced by the resolution, the contrast and the noise of BSE images. Values for zirconia, silica and pore space may especially have large errors either due to small grain size or small differences in their greyscale levels.) Rounded silica–zirconia–pore inclusions (identical to those found in samples annealed in an alumina crucible, cf. Fig. 2c) are abundant.

Discussion

In the phase diagram of the ZrO_2–SiO_2 system published by Butterman and Foster (1967), pure $ZrSiO_4$ was predicted to be stable up to 1676±7 °C. Kamaev et al. (2005) refined the same stability limit at 1674±7 °C. O'Neill (2006) predicted 1665 °C based on thermodynamical calculations. Most recently, Kaiser et al. (2008) arrived at the value of 1673±10 °C. However, zircon decomposition at the above temperatures seems to be the exception rather than the rule. In this study, decomposition was observed at 1400 °C, Kober (1986) observed breakdown between 1380 and 1480 °C, Mursic et al. (1992) reported a temperature of 1477 °C, Pavlik et al. (2001) recorded 1285 °C, Wang et al. (2006) and Wanthanachaisaeng et al. (2006) saw reaction products after heat treatment at 1400 °C, while Davis (2007) inferred a phase separation below 1550 °C. (See also Peña and de Aza 1984 and Kaiser et al. 2008 for a list of other temperature data.) The appearance of zirconia was observed even at unusually low temperatures by Zhang et al. (2000: 852 °C) Capitani et al. (2000: 927 °C) and Nasdala et al. (2002: between 800 and 950 °C) in fully metamict starting materials.

Effects of radiation damage

The synthetic and unaltered samples used in this study span an initial range in radiation damage from zero (syn) to moderate (M146; see Table 1). The character and the extent of breakdown observed on these samples suggest that initial radiation damage up to moderate levels has little influence on thermal decomposition. This is in agreement with Chapman and Roddick (1994), who found that appreciably different U concentrations and self-irradiation levels (10 ppm U, 1334 Ma vs. 160 ppm U, 2680 Ma; very low to moderate radiation damage) had little or no effect on the rate of zircon decomposition in vacuum.

Moderate radiation damage means that amorphous damage clusters are isolated in a defect-rich crystalline matrix. At high temperatures, a "self-epitaxial" recrystallisation of the damaged volumes, besides point defect annealing, is expected to occur (see Ewing et al. 2003). In contrast, in completely metamict zircon essentially the entire volume is amorphous. Monaghan et al. (2005) stated that amorphous SiO_2–ZrO_2 mixtures are thermodynamically unstable with respect to a mixture of solid oxides. Calculations by Kim and McIntyre (2002) also show that amorphous ZrO_2–SiO_2 mixtures with composition between 40–90 mol% SiO_2 should decompose into amorphous silica-rich and zirconia-rich phases at temperatures as low as 600 °C. Lucovsky and Rayner (2000) observed demixing of vapour-deposited Zr silicate films between 800 and 900 °C. Carrez et al. (2003) arrived at similar conclusions, i.e. at low temperatures amorphous $ZrSiO_4$ should undergo spinoidal decomposition as the component oxides are in the immiscibility domain.

Thus, spontaneous disintegration into a mixture of oxides in the amorphous volume is expected to occur prior to recrystallisation of fully metamict zircon upon heating. The appearance of zirconia in heavily damaged primary (unaltered) zircon at very low temperatures (Zhang et al. 2000; Capitani et al. 2000 and Nasdala et al. 2002; see above) is therefore not due to a decomposition reaction but results from the demixing of amorphous (metamict) zircon into more stable oxides.

Effects of alteration

The chemical resistance of heavily damaged zircon is significantly decreased against dissolution (e.g. Lumpkin 2001). A reaction of damaged zircon with fluids often yields secondary zircon in which the original texture, major and minor element composition and isotope concentrations

are modified (e.g. Geisler et al. 2002; Geisler et al. 2003a). Secondary, altered zircon, such as sample 87165, is generally porous with micrometre to nanometre-scale pores (Putnis 2002; Nasdala et al. 2009), enriched in non-formula elements (especially, P, Fe, Ca, Al etc.; e.g. Geisler et al. 2003b), mineral inclusions (e.g. xenotime) and hydrous species (Nasdala et al. 2009).

The high-temperature behaviour of strongly altered zircon (sample 87165) is poorly understood but alteration apparently has a profound influence on decomposition (Fig. 2). The effects of porosity, non-formula elements, mineral inclusions and hydrous content (Nasdala et al. 2009) are impossible to separate from each other. Enhanced porosity offers abundant pathways for element mobility in contrast to dense zircon. The "colourful" chemistry (non-formula elements in the percent range) is inferred to play a role in lowering temperatures of dissociation reactions and, along with solid (mineral) inclusions, has a strong influence on phase equilibria (see e.g. Peña and de Aza 1984). The hydrous species, apart from lowering reaction temperatures, may react with silica and may chemically bind to or volatilise available SiO_2. In general, SiO_2 appears to be significantly more mobile in altered than in unaltered zircon, as seen from the nearly complete reaction of silica with the alumina crucible (Fig. 2a). At the same time, the reassociation of silica with zirconia is apparently limited, suggested by the coexistence of the two phases after four days of annealing (Fig. 2c–d). Experimental results presented in this paper do not allow us to draw precise conclusions about the effect of alteration on the thermal behaviour of zircon.

Effect of reaction conditions

The decomposition in synthetic $ZrSiO_4$ and unaltered samples is always related to outer surfaces, implying that the reaction is initiated by external influences, i.e. effects not related to bulk zircon properties. However, we have no direct explanation as to what actually starts the point corrosion, which then extends first into pits and then a breakdown front proceeding inwards.

The differences in the extent of breakdown between Pt and Al_2O_3 crucibles are attributed to the crucible material. Generally, surface corrosion (synthetic and unaltered samples) is more advanced in alumina-annealed grains (Figs. 2a, 3c and 4) compared to Pt-annealed analogues. The effect of alumina is most pronounced on the grain surfaces that were in physical contact with the alumina crucible: in these areas the breakdown reaction reached a clearly more advanced stage (Figs. 3c and 4). The same is observed on grains of sample 87165 (altered zircon), where free silica is seen after annealing in a Pt crucible, whereas very extensive silica removal is observed in alumina crucibles.

We assume that the silica reacted with alumina and the equilibrium shifted in favour of further decomposition. According to Zhao et al. (2003), a reaction between amorphous silica (a liquid state was suggested by Peña and de Aza 1984) and Al_2O_3, forming an aluminosilicate glass, occurs already below 1350 °C. However, without crystalline mullite seeds, mullite nucleates from an amorphous state only above 1400 °C (Zhao et al. 2003), which may well explain why no third phase was identified using Raman spectroscopy in alumina crucibles.

Similar conclusions can be drawn for the zircon inclusions in heat-treated ruby (Wang et al. 2006; Wanthanachaisaeng et al. 2006). In a zircon inclusion decomposition should not be observed if the host mineral is inert with respect to the breakdown products. This is not the case with corundum, and thus ZrO_2 is formed because the reaction between SiO_2 and Al_2O_3 forms an aluminosilicate phase, preventing the recrystallisation of zircon.

Our results seem to indicate that zircon is chemically less resistant than it is often assumed. Direct contact of zircon with a potentially reactive material should therefore be avoided during the high-temperature treatment of zircon gems. Also, for long-term nuclear waste storage purposes care should be taken to avoid contact between zircon as waste form and any container material that may react with silica.

A comparison of our results to other studies in the literature reveals that the reaction atmosphere also has an influence on the breakdown of zircon into component oxides well below the thermodynamic decomposition temperature. The products of the breakdown reaction (especially ZrO_2) have been observed when annealing in air (e.g. under atmospheric pressure in this study), under vacuum (e.g. Kober 1986; 1987; Ansdell and Kyser 1993; Chapman and Roddick 1994), in a hot combustion atmosphere (Fritsch et al. 2006) and in a reducing, gaseous atmosphere (Gardner and Buchanan 1975; Barreiro et al. 2009) as well.

The reaction atmosphere appears to influence the activity of silica in the vicinity of the grain surfaces. We assume that the flow of volatile species away from the grain surface, following the concentration/pressure gradient, is the main driving force under vacuum. In a hot combustion atmosphere (significant H_2O partial pressure), such as that found in gas turbine engines, Fritsch et al. (2006) suggested the reaction of SiO_2 with water vapour forming volatile $Si(OH)_4$. In a reducing atmosphere, Gardner and Buchanan (1975) suggested a direct volatilisation of SiO_2 and its reduction into SiO by H_2 or CO. In low-pressure experiments (10^{-3} atm) done in a graphite furnace, Barreiro et al. (2009) reported that an increasing partial pressure of O_2 (2×10^{-9}–2×10^{-4} atm) in the furnace resulted in an increase in the weight loss of heated zircon samples. They explained this trend by suggesting a reaction between the graphite

furnace and oxygen to form CO, which then reduces SiO_2 into volatile SiO. Pavlik et al. (2001) used mass spectroscopy to identify volatile SiO during vacuum heating of zircon, i.e. without a reducing atmosphere.

The zircon samples heated in reducing (Gardner and Buchanan 1975; Barreiro et al. 2009) and hot combustion atmospheres (Fritsch et al. 2006) develop porous zirconia crusts analogous to zircon heated in air (Figs. 3c and 4) or in vacuum (Ansdell and Kyser 1993; Chapman and Roddick 1994). We find it questionable that reducing agents (CO, H_2) or water vapour actually reach the zircon–baddeleyite reaction front once it is covered by a porous zirconia crust. We instead think that a volatilisation of SiO_2 occurs at or near the reaction front, SiO_2(g) diffuses through porous zirconia into the furnace atmosphere and reduction (to SiO) or hydroxide formation ($Si(OH)_4$) may occur only there, accelerating the reaction by decreasing the amount (partial pressure) of SiO_2 available. The decomposition of zircon therefore is not caused, only indirectly enhanced, by reductive gases or water vapour. Gas flow, as in the experiments of Fritsch et al. (2006), further increases the removal of volatile species.

Air is essentially free of reducing gases (given that no reduction occurs in the heated furnace) and the concentration of water vapour is typically very low (<22.9 $g\,m^{-3}$ at 25 °C, which becomes <4.1 $g\,m^{-3}$ when heated to 1400 °C). We expect that if no reaction occurs between evaporated silica and the reaction atmosphere (N_2, O_2, CO_2) and crucible material (e.g. Pt), the reaction rate will be lower in dry-air annealing compared to heat treatment in reductive or hydrous atmospheres. Furthermore, air pressure may also decrease the rate at which SiO_2(g) diffuses away from the reaction environment, therefore we expect the advance of the zircon–baddeleyite reaction front to be slower in a non-reducing gas atmosphere than in vacuum.

Implications for age determination techniques

We propose that thermal decomposition of zircon plays a key role in the success of age determination techniques that employ heat treatment. Two techniques are briefly outlined and the role of thermal decomposition is explained below.

In the whole-grain zircon evaporation technique of Kober (1986, 1987) and related methods (Davis 2007) a zircon grain is wrapped in a strip of rhenium foil (evaporation filament) so that only a thin slit is open facing a second Re filament (ionisation filament). Heating the zircon grain up to ca. 1230 °C is found to remove lead loosely bound (adsorbed) on surfaces and from highly leached (altered) domains. After such preconditioning, successively higher-temperature evaporation steps between 1330–1530 °C are used to decompose and evaporate zircon domains with decreasing Pb loss (for more details see Kober 1987 and Ansdell and Kyser 1993). In the CA–TIMS technique (Mattinson 2005), thermal preconditioning of whole zircon grains is done at 800–1100 °C in air for 48 h. After heat treatment the U/Th–Pb system is analysed through stepwise dissolution and mass spectroscopy (partial dissolution analysis, PDA). The key to the success of PDA is the heat treatment; without annealing PDA is not so effective.

A common feature in the two techniques is that there is an evolution of the isotope ratios in progressive evaporation/dissolution steps from open-system ("discordant") towards closed-system ("concordant") character. Note that Kober (1986; 1987) and Ansdell and Kyser (1993) associated the later stages (i.e., higher temperatures) of breakdown with increasing crystallinity. The results in this study (compare Figs. 3c and 4) and those of Chapman and Roddick (1994) suggest that structural damage up to moderate levels is not a major factor that governs the decomposition reaction. We need to emphasize that structural damage due to self-irradiation does not directly induce Pb loss (or a change in composition in general), only diminishes the resistance of primary zircon against dissolution (leaching).

Our results suggest that in zircon evaporation experiments the decomposition temperature of different domains is a function of the extent of chemical alteration. This is reflected in the order in which the zircon domains undergo breakdown: Pb will be released successively from domains less and less affected by Pb leaching and/or enrichment. The last domains to decompose will have a closed isotope system (no alteration), seen as a plateau $^{207}Pb/^{206}Pb$ age in TIMS.

We propose that in a CA–TIMS experiment different processes occur in zircon domains according to their alteration levels. Moderately damaged but unaltered domains experience a recovery of crystallinity. In altered or amorphous zones a phase separation into component oxides takes place. Partially decomposed zircon or a mixture of oxides is expected to be less stable, while the resistance of recrystallised zircon domains is increased against dissolution by HF. Subsequent PDA steps are therefore able to separate zircon zones according to the extent of breakdown developed during thermal preconditioning. Alumina crucibles (Mattinson 2005) may have the effect of reacting with silica, enhancing the decomposition of zircon. Note that the onset temperature of aluminosilicate glass formation in the reaction between zircon and alumina was put to ca. 1100 °C by Zhao et al. (2003), which is just at the upper limit of zircon annealing in the CA–TIMS technique. Annealing of zircon in SiO_2 crucibles, in contrast, may actually decrease the extent of breakdown by increasing silica activity in the reaction atmosphere. It appears worthwhile to test the two

crucible materials against each other in a chemical abrasion experiment.

Conclusions

The high-temperature breakdown of unaltered zircon below the generally accepted thermodynamical dissociation temperature (1665–1676 °C) is a surface corrosion process producing crystalline ZrO_2 and amorphous SiO_2. Silica is inferred to evaporate below 1400 °C. The extent of the breakdown is controlled by temperature and processes that decrease SiO_2 activity in the reaction environment, such as molecular flow or diffusion due to a concentration gradient, reaction of silica vapour with the atmosphere (e.g. reduction by H_2, CO or hydroxide formation with water vapour), solid-state reactions (e.g. with the crucible or the furnace material) or transport by a gas stream in the experimental chamber. Therefore if minimum decomposition is desired, a small-volume inert (e.g. Pt) crucible and a non-reactive atmosphere (such as N_2 or air) should be used to anneal zircon at high temperatures. Similar constraints may apply to containers designed to be used for nuclear waste storage.

Acknowledgements Samples studied in this research were kindly provided by J.M. Hanchar (synthetic zircon), M. Wiedenbeck (91500), W. Hofmeister (M127, M144, M146, M257), and C. Pérez-Soba (87165). Thanks are due to A. Wagner for the excellent sample preparation, and to B. Ullrich for obtaining a BSE image of an annealed La Pedriza zircon. We are grateful to I. Dódony and D.W. Davis for helpful discussions and suggestions. The constructive reviews by J.M. Hanchar and an anonymous expert, and detailed comments by associate editor A. Möller, greatly contributed to the manuscript. Partial funding for this study was provided by the European Commission through contract no. MEXC-CT-2005-024878 and by the Austrian Science Fund (FWF) through grant no. P20028-N10.

References

Ansdell KM, Kyser TK (1993) Textural and chemical changes undergone by zircon during the Pb-evaporation technique. Am Mineral 78:36–41

Barreiro P, Rey P, Souto A, Guitián F (2009) Porous stabilized zirconia coatings on zircon using volatility diagrams. J Eur Ceram Soc 29:653–659

Begg BD, Hess NJ, Weber WJ, Conradson SD, Schweiger MJ, Ewing RC (2000) XAS and XRD study of annealed ^{238}Pu— and ^{239}Pu-substituted zircons ($Zr_{0.92}Pu_{0.08}SiO_4$). J Nucl Mat 278:212–224

Butterman WC, Foster WR (1967) Zircon stability and the ZrO_2-SiO_2 phase diagram. Am Mineral 52:880–885

Capitani GC, Leroux H, Doukhan JC, Ríos S, Zhang M, Salje EKH (2000) A TEM investigation of natural metamict zircons: structure and recovery of amorphous domains. Phys Chem Minerals 27:545–556

Carrez P, Forterre C, Braga D, Leroux H (2003) Phase separation in metamict zircon under electron irradiation. Nucl Instrum Meth B 211:549–555

Chapman HJ, Roddick JC (1994) Kinetics of Pb release during the zircon evaporation technique. Earth Planet Sci Lett 121:601–611

Colombo M, Chrosch J (1998) Annealing of natural metamict zircons: II high degree of radiation damage. Radiat Phys Chem 53:563–566

Colombo M, Chrosch J, Salje EKH (1999) Annealing metamict zircon: a powder X-ray diffraction study of a highly defective phase. J Am Ceram Soc 82:2711–2716

Davis DW (2007) Sub-m.y. age resolution for Precambrian igneous events by thermal extraction (TE-TIMS) Pb dating of zircon: Application to progressive crystallization of the 1849 Ma Sudbury impact melt. Geochim Cosmochim Acta 71:A206

Ellsworth S, Navrotsky A, Ewing RC (1994) Energetics of radiation damage in natural zircon ($ZrSiO_4$). Phys Chem Minerals 21:140–149

Ewing RC, Meldrum A, Wang L, Weber WJ, Corrales LR (2003) Radiation effects in zircon. In: Hanchar JM, Hoskin PWO (eds) Zircon. Mineral. Soc. Am., Washington, D.C., pp 387–425

Fritsch M, Klemm H, Herrmann M, Schenk B (2006) Corrosion of selected ceramic materials in hot gas environment. J Eur Ceram Soc 26:3557–3565

Gardner RA, Buchanan RC (1975) High temperature loss of silica from zircon and refractory silicates. J Electrochem Soc 122:205–211

Geisler T (2002) Isothermal annealing of partially metamict zircon: evidence for a three-stage recovery process. Phys Chem Miner 29:420–429

Geisler T, Pidgeon RT, van Bronswijk W, Kurtz R (2002) Transport of uranium, thorium, and lead in metamict zircon under low-temperature hydrothermal conditions. Chem Geol 191:141–154

Geisler T, Pidgeon RT, Kurtz R, van Bronswijk W, Schleicher H (2003a) Experimental hydrothermal alteration of partially metamict zircon. Am Mineral 88:1496–1513

Geisler T, Rashwan AA, Rahn MKW, Poller U, Zwingmann H, Pidgeon RT, Schleicher H, Tomaschek F (2003b) Low-temperature hydrothermal alteration of natural metamict zircons from the Eastern Desert, Egypt. Mineral Mag 67:485–508

Hanchar JM, Finch RJ, Hoskin PWO, Watson EB, Cherniak DJ, Mariano AN (2001) Rare earth elements in synthetic zircon: Part 1. Synthesis, and rare earth element and phosphorus doping. Am Mineral 86:667–680

Kaiser A, Lobert M, Telle R (2008) Thermal stability of zircon ($ZrSiO_4$). J Eur Ceram Soc 28:2199–2211

Kamaev DN, Archugov SA, Mikhailov GG (2005) Study and thermodynamic analysis of the ZrO_2–SiO_2 system. Russ J Appl Chem 78:200–203

Kim H, McIntyre PC (2002) Spinodal decomposition in amorphous metal–silicate thin films: Phase diagram analysis and interface effects on kinetics. J Appl Phys 92:5094–5102

Kober B (1986) Whole-grain evaporation for ^{207}Pb/^{206}Pb-age-investigations on single zircons using a double-filament thermal ion source. Contrib Mineral Petrol 93:482–490

Kober B (1987) Single-zircon evaporation combined with Pb^+ emitter bedding for ^{207}Pb/^{206}Pb-age investigations using thermal ion mass spectrometry, and implications to zirconology. Contrib Mineral Petrol 96:63–71

Lucovsky G, Rayner GBJ (2000) Microscopic model for enhanced dielectric constants in low concentration SiO_2-rich noncrystalline Zr and Hf silicate alloys. Appl Phys Lett 77:2912–2914

Lumpkin GR (2001) Alpha-decay damage and aqueous durability of actinide host phases in natural systems. J Nucl Mater 289:136–166

Mattinson JM (2005) Zircon U–Pb chemical abrasion ("CA–TIMS") method: Combined annealing and multi-step partial dissolution analysis for improved precision and accuracy of zircon ages. Chem Geol 220:47–66

McLaren AC, Fitz Gerald JD, Williams IS (1994) The microstructure of zircon and its influence on the age determination from Pb/U isotopic ratios measured by ion microprobe. Geochim Cosmochim Acta 58:993–1005

Mitsuhashi T, Ichihara M, Tatsuke U (1974) Characterization and stabilization of metastable tetragonal ZrO_2. J Am Ceram Soc 57:97–101

Monaghan S, Greer JC, Elliott SD (2005) Thermal decomposition mechanisms of hafnium and zirconium silicates at the atomic scale. J Appl Phys 97:114911

Mursic Z, Vogt T, Frey F (1992) High-temperature neutron powder diffraction study of $ZrSiO_4$ up to 1900 K. Acta Crystallogr B 48:584–590

Nasdala L, Wenzel M, Vavra G, Irmer G, Wenzel T, Kober B (2001) Metamictisation of natural zircon: accumulation versus thermal annealing of radioactivity-induced damage. Contrib Mineral Petrol 141:125–144

Nasdala L, Lengauer CL, Hanchar JM, Kronz A, Wirth R, Blanc P, Kennedy AK, Seydoux-Guillaume A-M (2002) Annealing radiation damage and the recovery of cathodoluminescence. Chem Geol 191:121–140

Nasdala L, Reiners PW, Garver JI, Kennedy AK, Stern RA, Balan E, Wirth R (2004) Incomplete retention of radiation damage in zircon from Sri Lanka. Am Mineral 89:219–231

Nasdala L, Hofmeister WG, Norberg N, Mattinson JM, Corfu F, Dörr W, Kamo SL, Kennedy AK, Kronz A, Reiners PW, Frei D, Kosler J, Wan YS, Götze J, Häger T, Kröner A, Valley JW (2008) Zircon M257 — a homogeneous natural reference material for the ion microprobe U–Pb analysis of zircon. Geostand Geoanal Res 32:247–265

Nasdala L, Kronz A, Wirth R, Váczi T, Pérez-Soba C, Willner A, Kennedy AK (2009) The phenomenon of deficient electron microprobe totals in radiation-damaged and altered zircon. Geochim Cosmochim Acta 73:1637–1650

O'Neill HSC (2006) Free energy of formation of zircon and hafnon. Am Mineral 91:1134–1141

Pavlik RS, Holland HJ, Payzant EA (2001) Thermal decomposition of zircon refractories. J Am Ceram Soc 84:2930–2936

Peña P, de Aza S (1984) The zircon thermal behavior: effect of impurities. Part 1. J Mater Sci 19:135–142

Pérez-Soba C, Villaseca C, González del Tánago J, Nasdala L (2007) The composition of zircon in the peraluminous Hercynian granites of the Spanish Central System batholith. Can Mineral 45:509–527

Putnis A (2002) Mineral replacement reactions: from macroscopic observations to microscopic mechanisms. Mineral Mag 66:689–708

Wang WY, Scarratt K, Emmett JL, Breeding CM, Douthit TR (2006) The effects of heat treatment on zircon inclusions in Madagascar sapphires. Gems Gemol 42:134–150

Wanthanachaisaeng B, Häger T, Hofmeister W, Nasdala L (2006) Raman- und fluoreszenz-spektroskopische Eigenschaften von Zirkon-Einschlüssen in chrom-haltigen Korunden aus Ilakaka und deren Veränderung durch Hitzebehandlung. Z Dt Gemmol Ges 55:123–136

Wiedenbeck M, Hanchar JM, Peck WH, Sylvester P, Valley J, Whitehouse M, Kronz A, Morishita Y, Nasdala L, Fiebig J, Franchi I, Girard JP, Greenwood RC, Hinton R, Kita N, Mason PRD, Norman M, Ogasawara M, Piccoli PM, Rhede D, Satoh H, Schulz-Dobrick B, Skar O, Spicuzza MJ, Terada K, Tindle A, Togashi S, Vennemann T, Xie Q, Zheng YF (2004) Further characterisation of the 91500 zircon crystal. Geostand Geoanal Res 28:9–39

Wirth R (2004) Focused Ion Beam (FIB): A novel technology for advanced application of micro- and nanoanalysis in geosciences and applied mineralogy. Eur J Mineral 16:863–876

Zhang M, Salje EKH, Capitani GC, Leroux H, Clark AM, Schluter J, Ewing RC (2000) Annealing of α-decay damage in zircon: a Raman spectroscopic study. J Phys: Condens Mat 12:3131–3148

Zhao SK, Huang Y, Wang CA, Huang XX, Guo JK (2003) Mullite formation from reaction sintering of $ZrSiO_4/\alpha$-Al_2O_3 mixtures. Mater Lett 57:1716–1722

Appendix 5

Váczi, T., Nasdala, L., Hanchar, J.M., Kronz, A., Götze, J., Dyar, M.D. & Wiedenbeck, M. (2009): Iron incorporation in zircon.
Submitted to *European Journal of Mineralogy*.

Submitted to
Eur. J. Mineral.
Manuscript no. F-203

Iron incorporation in zircon

TAMÁS VÁCZI[1,*], LUTZ NASDALA[1], JOHN M. HANCHAR[2], ANDREAS KRONZ[3], JENS GÖTZE[4], M. DARBY DYAR[5], MICHAEL WIEDENBECK[6]

[1] Institut für Mineralogie und Kristallographie, Universität Wien, Althanstr. 14., A–1090 Austria
[*] Corresponding author, e-mail: tamas.vaczi@univie.ac.at
[2] Department of Earth Sciences, Memorial University of Newfoundland, St. John's, NL A1B 3X5, Canada
[3] Geowissenschaftliches Zentrum, Georg-August-Universität Göttingen, Goldschmidtstrasse 1, D–37077 Göttingen, Germany
[4] Institut für Mineralogie, TU Bergakademie Freiberg, Brennhausgasse 14, D–09596 Freiberg, Germany
[5] Department of Astronomy, Mount Holyoke College, 50 College Street, South Hadley, MA 01075, USA
[6] Helmholtz-Zentrum Potsdam, Deutsches GeoForschungsZentrum, Telegrafenberg, D–14473 Potsdam, Germany

Abstract: Synthetic zircon crystals doped with either regular Fe or ^{57}Fe were grown using the Li–Mo flux method and investigated in detail by using electron probe microanalysis, secondary ion mass spectrometry, and Mössbauer, Raman and cathodoluminescence spectroscopy. Internal textures were studied using back-scattered electron and cathodoluminescence imaging and Raman mapping. The zircon crystals were found to contain ca. 0.01–0.39 wt% Fe, with a clear zonation pattern within all crystals. The Fe concentration decreases, whereas short-range order increases, from crystal centres to rims. Mössbauer spectra of bulk samples, taken at temperatures down to 4 K, suggest that only slightly less than half of the iron present in the zircon crystals is incorporated in the zircon structure, whereas the remainder of the Fe occurs as micro-inclusions of unreacted hematite. In the zircon structure, the majority of the iron is present as Fe^{3+}; however, Fe^{2+} is also present. The Fe^{3+} and Fe^{2+} are predominantly located on the six-coordinated interstitial site. Observations suggest that Fe incorporation into the zircon structure during primary growth is strongly limited. High Fe concentrations in natural zircon samples, in the wt% range, may therefore be a reliable indicator of secondary alteration processes.

Key-words: zircon, iron doping, electron microprobe, Mössbauer spectroscopy, Raman spectroscopy, cathodoluminescence, SIMS

Introduction

Zircon ($ZrSiO_4$) occurs as an accessory mineral in many geological settings. It forms in a wide variety of geological conditions and is ubiquitous due to its enormous physical durability and resistance against chemical alteration and disintegration. Favoured by these extraordinary properties, zircon plays a significant role in many industrial and materials science applications as well. For example, synthetic zircon has been considered as a suitable form for long-term sequestration of actinide nuclear waste (Ewing *et al.*, 1995), while $ZrSiO_4$ doped with elements such as Fe has found uses in the manufacture of glazes in the ceramics industry (*e.g.*, Berry *et al.*, 1996). In the investigation of natural zircon, an understanding of the incorporation of trace levels of non-formula elements is important for understanding crustal and mantle processes. One key application of zircon is its common use in geochronology (Davis *et al.*, 2003, and references therein). This technique is based on the incorporation of trace amounts of U and Th (that decay to form radiogenic Pb), whereas Pb is mostly excluded during primary growth. Furthermore, Ti incorporation in zircon is used for geothermometry (Watson & Harrison, 2005), while rare earth element (REE) concentrations reveal magma sources (*e.g.*, Hoskin & Ireland, 2000; Hoskin & Schaltegger, 2003 and references therein).

Primary and altered zircon crystals show distinct differences in their chemical compositions and internal textures. At the time of primary growth only low concentrations of compatible non-formula elements are normally incorporated into the structure (Speer, 1980; Hoskin & Schaltegger, 2003). Uranium and thorium are common trace elements in natural zircon; however, with time they cause damage to the structure through a series of radioactive decay events (mostly due to the alpha particles and recoil nuclei; Ewing *et al.*, 2003). Radiation damage lowers the chemical (and physical) durability of zircon, making the material more susceptible to chemical alteration by fluids. Alteration involves the dissolution of damaged primary zircon, and new growth of crystalline, but often highly porous, secondary zircon that usually contains a significantly larger number and higher

concentration of non-formula elements. Elements normally not found in primary but often present in secondary zircon include P, Fe, Ca, Pb and many more (*e.g.* Geisler *et al.*, 2003; Nasdala *et al.*, 2009a and b).

Iron, typically found in low concentrations in natural, unaltered zircon (*e.g.*, 0.10 wt% FeO in lunar zircon; Wopenka *et al.*, 1996), may be significantly enriched in certain cases. An extensive list of zircon analyses from the literature was compiled by Görz (1974, and references therein), citing up to 10 wt% Fe; however, it is not clear from that study if inclusions of Fe-bearing minerals were also analysed. Zircon samples reported as being altered were shown to contain FeO well in the wt% range (*e.g.*, Smith *et al.*, 1991: up to 5.5 wt% Fe; Johan & Johan, 2005: up to 1.7 wt% FeO; Breiter *et al.*, 2006 up to 3.6 wt% FeO; Nasdala *et al.*, 2009b: up to 7.24 wt% FeO). It appears that the physical and chemical changes associated with alteration may give rise to such elevated Fe concentrations.

Primary and altered natural zircon always contains a multitude of trace elements (*e.g.*, Hf and REEs, U and Th; Hoskin & Schaltegger, 2003). Synthesis of Fe-doped zircon provides the opportunity to describe the influence of the incorporation of Fe distinct from other elements. Synthetic, Fe-doped $ZrSiO_4$ may have an intense pinkish colour that is likely due to micro-inclusion of hematite, (α-Fe_2O_3; *e.g.*, Berry *et al.*, 1996; Ball & van Wyk, 2000; Llusar *et al.*, 2001; Ardizzone *et al.*, 2002; Carreto Cortés *et al.*, 2004). Due to its refractory nature, Fe-doped zircon has become a popular pink pigment under the name of "iron zircon coral", "pink zircon", "coral zircon" and so on. Opinions differ, however, on the extent of Fe incorporation directly into the zircon structure, and on the structural positions that may be occupied by Fe in zircon (*e.g.*, Berry *et al.*, 1996; Ball & van Wyk, 2000).

This paper addresses the question whether Fe concentration levels detected in natural zircon are artefacts arising from measuring Fe-rich inclusions or coatings such as hematite, or that the detected Fe may indeed be incorporated into the zircon structure. In order to test for the site occupancy and oxidation state of substituent ions, synthetic Fe-doped crystals were prepared, one batch with natural Fe isotope abundances and another one using enriched ^{57}Fe to facilitate acquisition of Mössbauer spectra.

Samples and analytical methods

Iron-doped zircon crystals were synthesized using the Li–Mo flux method described in Hanchar *et al.* (2001). High-purity ZrO_2 (2.53 wt%) and SiO_2 (1.24 wt%) were mechanically mixed in a MoO_3–Li_2MoO_4 flux (85.32 and 8.93 wt%, respectively), with Fe_2O_3 (1.83 wt%) added as a dopant. Phosphorus in the form of $NH_4H_2PO_4$ (0.16 wt%) was added to both batches to assist charge balancing of the incorporated Fe. The oxide starting materials were dried at 100 °C and then mixed under ethanol using an agate mortar and pestle. After drying under a heat lamp, the mixed oxide powders were transferred to a 25 mL platinum crucible with a tightly-fitted platinum lid. The mixtures for each synthesis were then suspended using Pt wire from an alumina rod in the "hot spot" of a Deltech $MoSi_2$ vertical tube furnace at 950 °C for 22 days. The temperature was monitored externally with a Type S thermocouple and was found not to deviate more than ±5 °C. For "Batch 47", high purity Fe_2O_3 (Alfa-Aesar) was used. For "Batch 48", isotope-enriched $^{57}Fe_2O_3$ (WEB Research, Edina, Minnesota) was used instead. The isotopic composition of the latter was ^{54}Fe (<0.1%), ^{56}Fe (1.2%), ^{57}Fe (96.6%) and ^{58}Fe (2.2%).

A few Fe-doped zircon single crystals of each synthesis batch were embedded in epoxy resin and polished to expose a cross-section parallel to the *c* axis of the crystals. Sample mounts were carbon coated before electron imaging and analysis. The samples were gently hand-polished to remove the carbon coat prior to Raman and ion probe (secondary ion mass spectrometry, SIMS) measurements. For SIMS analyses the sectioned grains were ultrasonically cleaned in high-purity ethanol and coated with a 35 nm thick, high purity gold film. For Mössbauer measurements crystals or crystal fragments without noticeable flux inclusions were powdered. Samples were then prepared by gently mixing the zircon powders with sugar to reduce preferred orientation. The mixtures were gently heaped in a sample holder confined by Kapton tape.

Secondary electron (SE), backscattered electron (BSE) and panchromatic cathodoluminescence (CL) images as well as electron probe microanalyses (EPMA) were acquired using a JEOL JXA-8900RL electron microprobe operated at 20 kV accelerating voltage. The beam current was 20 nA for imaging and 80 nA for chemical analyses. Concentration calibration was done on pure synthetic $ZrSiO_4$ (Zr, Si), natural hematite (Fe), natural apatite (P) and metallic molybdenum (Mo). Counting times were 30 s (peak) + 2 × 15 s (lower and upper backgrounds) for Zr and P, 15 + 2 × 5 s for Si, and 120 + 2 × 60 s for Fe. Matrix corrections were made using the $\Phi(\sigma Z)$ method of Armstrong (1991, 1995).

Colour CL images and CL spectra were recorded using a "hot-cathode" CL microscope HC1–LM (*cf.* Neuser *et al.*, 1995), operating at 14 kV accelerating voltage and a current density of *ca.* 10 μA/mm^2. Spectra were acquired with an Acton Research SP-2356 digital triple-grating spectrograph and a Princeton Spec-10 charge-coupled device (CCD) detector that was connected to the CL microscope through a silica-glass fibre guide. CL spectra were measured under standardised conditions (wavelength calibration by a Hg–halogen lamp, spot width 30 μm, measuring time variable).

Raman analyses were done using a JobinYvon LabRam HR system using 632.8 nm excitation (3 mW measured under the objective). The spectral calibration was done using the Rayleigh line and neon lamp emissions, resulting in a wavenumber accuracy of 0.5 cm^{-1}. The spectral resolution (i.e., apparatus function)

was 0.8 cm^{-1}. More experimental details on the Raman experimental setup are reported elsewhere (Nasdala *et al.*, 2005). Band-width correction for the apparatus function was done in accordance with Irmer (1985).

Mössbauer spectra were acquired at 293 K, 240 K, 190 K, 80 K and 4 K, using a source of ~95 mCi ^{57}Co in Rh on a WEB Research Co. model WT302 spectrometer equipped with a Janus closed-cycle He cooling system to allow variable-temperature measurements. Each spectrum was corrected to subtract the fraction of the baseline counts due to the Compton scattering. Run times were 6–24 hours for each spectrum, and baseline counts were ~6–14 million after the Compton correction. Data were collected in 1024 channels and corrected to a linear velocity scale. Before fitting, the spectra were folded about the channel value that produces the minimum least squares sum difference between the first half of the spectrum and the reflected second half. To model the data, we used the Mexdist program from the University of Ghent, which solves for the full Hamiltonian. Overall errors on isomer shift and quadrupole splitting are ±0.05–0.1 mm/s, while errors on doublet areas are approximately ±3% absolute.

Secondary ion mass spectrometry data were collected using the Cameca ims 6f SIMS instrument at the GeoForschungsZentrum Potsdam. The analyses employed a 2 nA, nominally 12.5 kV, $^{16}O^-$ primary beam, focused to a ca. 5 µm diameter spot at the sample surface. Total pressure in the sample chamber was *ca.* $7 \cdot 10^{-7}$ Pa. Analysis domains were pre-sputtered with an unrastered beam for five minutes to suppress any Li surface contamination and to establish equilibrium sputtering conditions. A single analysis consisted of 20 cycles of the peak stepping sequence 6.9 Da (0.1 s used for magnet cycling purposes), ^7Li (2 s) and ^{30}Si (2 s). The mass spectrometer was operated at a mass resolving power of $M/\Delta M \approx 3100$, sufficient to resolve the mass interference between $^1H^{29}Si$ and ^{30}Si. A 50 V energy band pass was used to which no offset voltage was applied. Data collection was done with a discrete dynode pulse counting system with count rates on ^{30}Si typically around 25 kHz.

In order to estimate roughly the absolute Li concentrations in the synthetic zircon (a flux component used in the synthesis), we ran multiple analyses of the NIST 610 glass at the beginning and the end of each day's analysis. This material's "preferred average" Li concentration of 484.6 µg/g (Pearce *et al.*, 1997) was used for data assessment. Because the calibration material was neither chemically nor structurally matrix-matched to the zircon being analyzed, the determined concentration values must be viewed as semi-quantitative at best. In contrast, the relative variations in Li contents observed within and between zircon crystals can be viewed as correct.

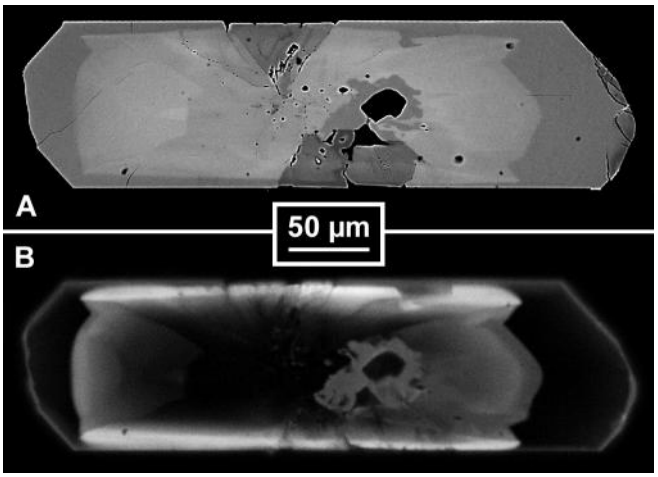

Fig. 1. A cross-section of a synthetic, iron-doped zircon crystal parallel to the *c* axis reveals growth and sector zoning. (A) BSE and (B) panchromatic CL image. Irregular black holes are locations of flux inclusions.

Results and discussion

The synthetic zircon crystals are clear, almost colourless with a faint brownish tint. The morphology is dominated by tetragonal prisms (Fig. 1), with lengths between 250 and 500 µm. Under a microscope irregular dark inclusions are seen inside the crystals. On cross-cut grains, these inclusions appear black in BSE (Fig. 1a) and CL images (Fig. 1b), and are identified as inclusions of the flux reagents.

Growth and sector zoning is observed in all samples. Zoning is most easily visualised in the CL images. There is often a clearly-outlined dark centre surrounded by a zone with strong luminescence that often shows oscillatory zoning (Fig. 1b and the inset in Fig. 2). The rims of the crystals display dark CL. Cathodo-luminescence spectroscopy reveals that crystal centres are weaker CL emitters than rims, especially if the broad Fe^{3+} band around 760 nm is measured (Fig. 2). Groups of narrow-band emissions arise from very minor concentrations of REEs (especially Dy^{3+} and Sm^{3+}, below electron microprobe detection limits); these are probably due to lowest-level (*i.e.*, sub-µg/g) contaminations present in the ultrapure ZrO_2 used for synthesis. The CL signal intensity was used for targeting chemical analysis spots, and the CL properties (low-CL rim, high-CL or intermediate zone, low-CL centre) are used to describe growth zones in the discussion below.

The EPMA analyses (Table 1) demonstrate that only Zr, Si, P and Fe are present, and the abundance of the non-formula elements follows the textures seen in the images (Fig. 1). Crystal centres have been found to contain the highest concentrations of P and Fe, decreasing gradually towards the rims. Total Fe contents ranged between 0.45–0.55 wt% Fe_2O_3 in low-CL centres, 0.12–0.37 wt% Fe_2O_3 in the intermediate zone and 0.02–0.14 wt% Fe_2O_3 in rims. The decrease of Fe_2O_3 concentration from centre to rim is either a result of the depletion of Fe in the reaction mixture or of internal

Table 1. Chemical analyses on ^{57}Fe-doped synthetic zircon. Values in weight percent (wt%) are electron microprobe data; Li was measured with SIMS. Lithium concentration values are to be regarded as semi-quantitative but relative variations are accurate (see text).

Analysis point	Crystal #, character	ZrO_2 [wt%]	SiO_2 [wt%]	P_2O_5 [wt%]	Fe_2O_3 [wt%]	MoO_3 [wt%]	Total [wt%]	Li [µg/g]
1	5, centre (low CL)	66.7	30.3	2.54	0.48	b.d.l.	100.1	$4.4\cdot10^2$
2	5, centre (low CL)	66.7	30.4	2.55	0.46	b.d.l.	100.2	$3.8\cdot10^2$
3	5, high-CL	66.6	30.4	2.52	0.46	b.d.l.	100.0	93
4	6, high-CL	67.5	32.0	0.89	0.18	b.d.l.	100.7	5.0
5	7, high-CL	67.2	31.4	1.59	0.28	b.d.l.	100.5	$1.1\cdot10^2$
6	7, high-CL	67.1	32.0	0.89	0.19	b.d.l.	100.2	81
7	7, high-CL	67.3	32.0	0.81	0.16	b.d.l.	100.2	35
8	7, rim (low CL)	67.5	32.4	0.32	0.06	b.d.l.	100.3	0.3
9	9, centre (low CL)	66.9	30.4	2.50	0.45	b.d.l.	100.3	$1.3\cdot10^3$
10	9, high-CL	67.2	31.3	1.65	0.32	b.d.l.	100.4	$1.4\cdot10^2$
11	10, high-CL	67.1	31.3	1.59	0.29	b.d.l.	100.3	$1.2\cdot10^2$
	Detection limits*	0.06	0.06	0.04	< 0.01	0.01		< 1

The full set of EPMA data can be found in the online supporting material.
b.d.l.: below detection limit.
* Average detection limit (wt% oxide; 2*s* error by counting statistics of the background signal).

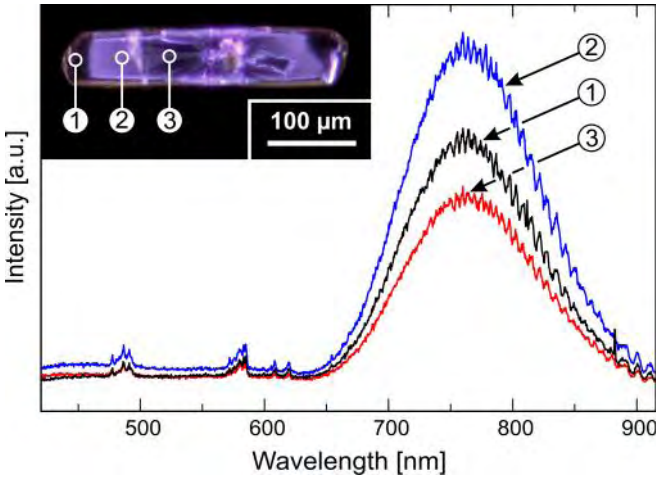

Fig. 2. Three CL emission spectra from a ^{57}Fe-doped synthetic zircon crystal; the inset shows a hot-cathode CL image. The spectra are dominated by the broad-band Fe^{3+} emission at around 760 nm. The groups of narrow-band emissions in the 470–620 nm range are due to very minor REE impurities (below EPMA detection limits). Note that the centre of the grain has the highest Fe concentration (>0.4 wt% Fe_2O_3; spectrum/spot 3) but is "darker" in CL than the rim with the lowest Fe concentration (<0.1 wt% Fe_2O_3; spectrum/spot 1). The intermediate zone (~0.25 wt% Fe_2O_3; spectrum/spot 2) emits the highest CL intensity.

strain in the crystals caused by impurity elements (Finch *et al.*, 2001). The depletion phenomenon is generally consistent with observations made by Berry *et al.* (1996), *i.e.*, that Fe incorporation depends on the availability of Fe.

The charge imbalance caused by incorporation of Fe into zircon was intended to be compensated by the addition of pentavalent P to the reaction mixture. A very good correlation is seen between Fe and P concentrations (see Fig. O1a in the online supporting material), though with a ratio of 1 Fe to *ca.* 1:6.4 P (expressed in atoms per formula unit, apfu). If Fe substituted for tetravalent structure cations, then the Fe to P ratio should be between 1:1 (if only Fe^{3+} were present) and 1:2 (for Fe^{2+} only). Finch *et al.* (2001) and Hanchar *et al.* (2001) reported P in zircon samples doped with light REEs in excess of the 1:1 ratio (xenotime-type substitution). Note, however, that REEs were found to replace Zr in the dodecahedral site and in natural zircon REEs may reach a concentration of several 1000 µg/g (Hoskin & Schaltegger, 2003) In contrast, Fe mostly occupies an interstitial site in our samples (see below) and in unaltered zircon the concentration is typically very low (tens to hundreds of µg/g, but often below EPMA detection limits; see *e.g.* Nasdala *et al.*, 2004). The 6-fold enrichment in P concentrations suggests that there is an unknown mechanism, most likely independent from the presence of Fe, causing P to be incorporated. Phosphorus also shows a very good correlation with Si deficiency (1 – Si) in calculated formulas (see Fig. O1b). It appears therefore that P primarily substitutes for Si in the zircon structure (Si + P = 0.98–1 .00 apfu; Table O1).

The peculiar ratio of Fe to P required further investigation to test for flux contaminants incorporated in the Fe-doped synthetic zircon crystals (*e.g.*, Finch *et al.*, 2001; Hanchar *et al.*, 2001). Electron microprobe results (Table 1) suggest that the Mo concentration is negligible (*i.e.*, below detection limits). Molybdenum is in the hexavalent oxidation state under the synthesis conditions (Hanchar *et al.*, 2001) and does not easily fit in the zircon structure. Lithium (as Li^+) concentration values (SIMS

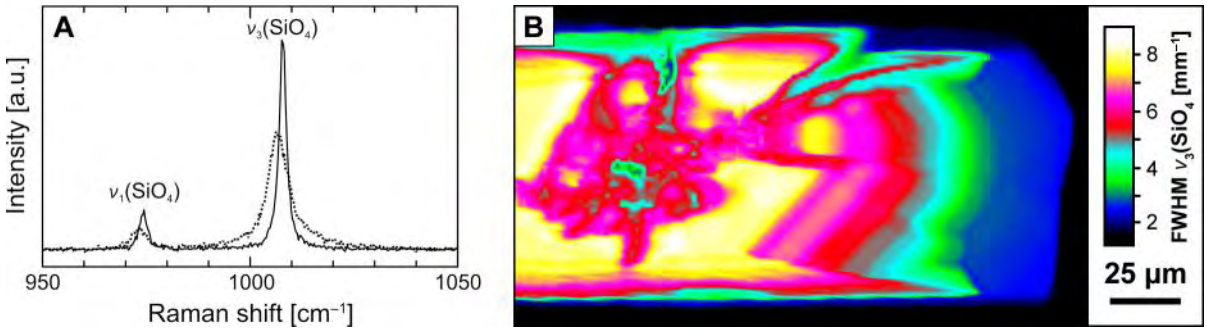

Fig. 3. Results of Raman analysis. (A) Two spectra extracted from the Raman map in (B). Dotted line: centre region (high Fe concentration, yellow–white in B); solid line: rim zone (low Fe concentration, dark blue in B). (B) Raman map created from the FWHM parameter of the zircon $\nu_3(SiO_4)$ band. Band broadening increases gradually from rim to centre.

analyses, Table 1) broadly follow the zones outlined by CL imaging; in the low-CL rims and intermediate (high-CL) zones are measured invariably below 140 µg/g. Higher concentrations (380–1300 µg/g) are found only in grain centres. We assume, however, that the few outstandingly high values (> 500 µg/g) come from analysis points where an unrecognised flux inclusion (smaller in size than the resolution of imaging methods) was sputtered by the ion beam.

Lithium concentrations can either be explained by Li in the zircon structure (Finch *et al.*, 2001; Hanchar *et al.*, 2001) or by very small (*e.g.*, sub-micrometre) inclusions of the flux. In both cases, the chemical zoning may be attributed to the growth of more "regular" (i.e., stoichiometric) zircon towards the rims (less non-formula elements and/or fewer inclusions). Lithium concentrations, however, do not correlate as well with Fe as does P (Table 1; note again that the variation between Li concentrations is accurate but actual values are semi-quantitative at best). Thus, it cannot be confidently stated whether Li acts as a charge compensator or not. Calculations indicate that *ca.* 0.2 wt% Li_2O (on the order of 1000 µg/g Li) is needed to charge balance 3 wt% P_2O_5 (which is the maximum P concentration measured in our samples; see Table O1). Given the systematic uncertainties present in our quantitative SIMS data, the possibility of Li compensating the charge of P (and Fe) cannot be fully excluded.

The FWHM (full width at half maximum) of the $\nu_3(SiO_4)$ zircon Raman band, which is strongly controlled by the degree of short-range order (Nasdala *et al.*, 1995; Geisler *et al.*, 2005), gradually increases from the outermost rim (1.6 cm^{-1}) to the centre (8.1 cm $^{-1}$; Fig. 3). The broadening is accompanied by a slight shift in the band position (*ca.* 1008 cm^{-1} at the rim to 1005 cm^{-1} at the centre). Figure 4 demonstrates the relationship between the FWHM of the $\nu_3(SiO_4)$ Raman band and Fe concentrations, measured on the same spots. However, changes in zircon Raman parameters are large, and most likely cannot be assigned only to the incorporation of Fe. The concentrations Fe and P are strongly correlated while P concentration is *ca.* 6.4 times higher (expressed as apfu; Fig. O1a). Therefore it is safer to say that the decrease in short-range order, seen as Raman band broadening, shows a dependence on dopant levels and is most likely representative of internal strain in the zircon crystals.

Low CL emission in the crystal rims is due to a low concentration of emission centres (Fe^{3+}). Increasing Fe concentrations give rise to a stronger CL signal but the most Fe-rich zone is dark again (Figs. 1B and 2). This may either be due to a concentration quenching phenomenon or to a change in the valence state of Fe during synthesis. While Fe^{3+} is a CL emitter (broad band around 760 nm), Fe^{2+} is not a CL centre and has been reported to suppress CL emission in minerals (*e.g.*, Habermann, 2002). The Mössbauer results (see below) suggest that both Fe^{2+} and Fe^{3+} are present. However, because the Mössbauer measurements were made on

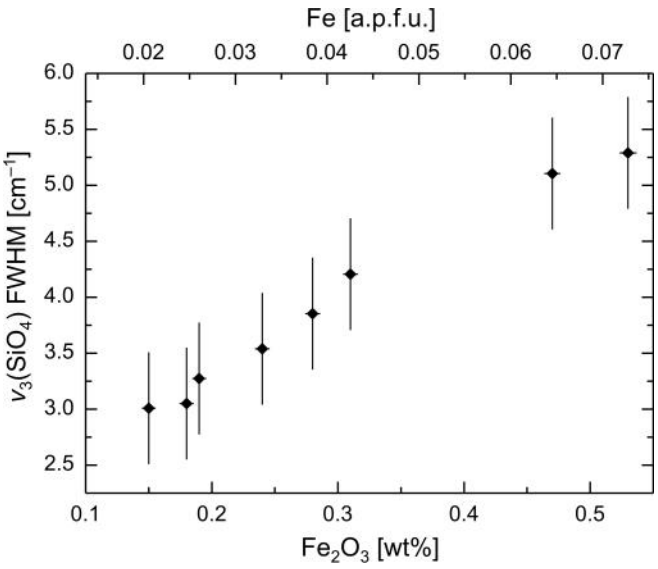

Fig. 4. Plot showing the dependence of the $\nu_3(SiO_4)$ zircon Raman band width on Fe concentrations, measured on seven Fe-doped zircon crystals. Uncertainties in the Raman data include those of fitting, the correction for the apparatus function and the scatter of individual measurements in a given growth zone.

powdered samples, we have no information on the spatial distribution of Fe valences in the sample grains.

The Mössbauer results (Table 2) indicate that more than half (59–63%) of the iron incorporated in the zircon crystals is present in the form of α-Fe_2O_3 (hematite). In addition to the hematite components, there were signals arising from Fe incorporated structurally in zircon (Fig. 5) distributed between two sites. A normally-vacant 6-fold site (Robinson *et al.*, 1971; Finch *et al.*, 2001) hosts 59–65% of the Fe in zircon (22–26% of the total Fe) in the form of Fe^{3+}. Between 25 and 38% of the Fe in zircon (10–14% of the total Fe) was refined at the 6-coordinated site as Fe^{2+}. The rest of the Fe^{2+} was located in an 8-fold coordination, thus replacing Zr; the matching doublet represents 3–10% of the Fe in zircon (1–4% of the total Fe). The isomer shifts measured for the doublets corresponding to 6 and 8-coordinated Fe^{2+} (Table 2) are slightly higher than those that are typical for $^{VI}Fe^{2+}$ and $^{VIII}Fe^{2+}$ in silicates, presumably due to an effect of Zr neighbours.

The Mössbauer results of the present contribution agree reasonably well with the main findings of earlier studies of Fe in zircon. An extended portion of the iron is present as hematite, and Fe can only be incorporated in the zircon structure at low concentrations. Our results seem to support conclusions by Berry *et al.* (1996), who deduced from Mössbauer and electron paramagnetic resonance (EPR) spectroscopy measurements that paramagnetic Fe^{3+} is in low-symmetry rhombic interstitial sites. Those authors stated that iron enters

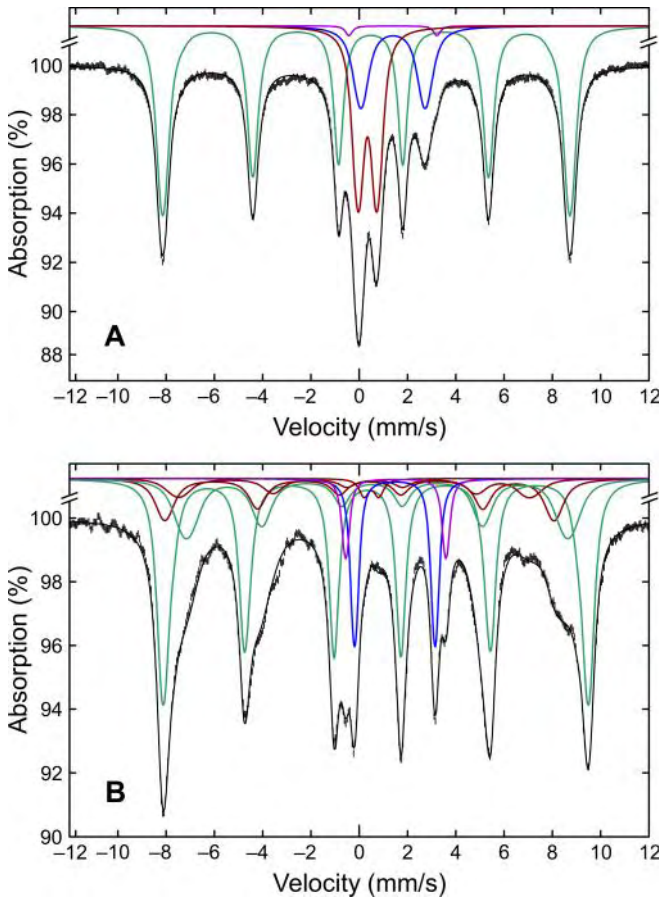

Fig. 5. ^{57}Fe Mössbauer spectra recorded on Batch 48 (^{57}Fe-doped zircon) (A) at room temperature (293 K) and (B) at 4 K. See Table 2 for Mössbauer parameters. Red — $^{VI}Fe^{3+}$; blue — $^{VI}Fe^{2+}$; purple — $^{VIII}Fe^{2+}$; green — hematite.

Table 2. ^{57}Fe Mössbauer parameters from the 293 K and 4 K measurements on ^{57}Fe-doped zircon (see also Fig. 5).

No.	Species	Parameter*	Temperature 293 K	Temperature 4 K
1	hematite	δ [mm/s]	0.38	0.51
		Δ [mm/s]	–0.18	0.34
		W [mm/s]	0.47	0.48
		B_{hf} [T]	52.3	54.7
		area [%]	63	48
2	hematite	δ [mm/s]		0.22
		Δ [mm/s]		–0.44
		W [mm/s]		0.80
		B_{hf} [T]		50.0
		area [%]		11
3	$^{VI}Fe^{3+}$	δ [mm/s]		0.21
		Δ [mm/s]		–0.85
		W [mm/s]		0.80
		B_{hf} [T]		44.9
		area [%]		6
4	$^{VI}Fe^{3+}$	δ [mm/s]		0.63
		Δ [mm/s]		0.21
		W [mm/s]		0.80
		B_{hf} [T]		49.1
		area [%]		19
5	$^{VI}Fe^{3+}$	δ [mm/s]	0.34	0.50
		Δ [mm/s]	0.72	0.58
		W [mm/s]	0.44	0.40
		area [%]	22	1
6	$^{VI}Fe^{2+}$	δ [mm/s]	1.40	1.47
		Δ [mm/s]	2.65	3.34
		W [mm/s]	0.62	0.30
		area [%]	14	10
7	$^{VIII}Fe^{2+}$	δ [mm/s]	1.39	1.51
		Δ [mm/s]	3.65	4.14
		W [mm/s]	0.30	0.30
		area [%]	1	4
		χ^2	2.67	2.56

* Parameters:
δ: isomer shift
Δ: quadrupole splitting
W: line width (FWHM)
B_{hf}: hyperfine field

higher-symmetry sites (*i.e.*, replaces cations in structural sites) only at higher concentrations. Also, Ardizzone *et al.* (2002) assigned certain features in diffuse reflectance spectra to Fe^{3+} in octahedral (interstitial) sites. Berry *et al.* (1996), Llusar *et al.* (2001) and Ardizzone *et al.* (2002) agree that a slight "creamy" or "peachy" colouration is due to interstitial Fe. The results of the present study and the above cited papers, however, contradict those of Ball & van Wyk (2000) and Carreto Cortés *et al.* (2004). Electron paramagnetic resonance spectroscopy results reported in Ball & van Wyk (2000) suggest that no Fe^{3+} occurs in interstitial sites, only in two distinct axial sites, and do not explicitly exclude Fe^{3+} occupancy in the Si site in the zircon structure. However, Ball & van Wyk (2000) did not quantify Fe concentration in their samples. Carreto Cortés *et al.* (2004) found only paramagnetic Fe^{3+}, apart from hematite, and assigned it to the dodecahedral (Zr) site in the zircon structure, which is not confirmed by our data (Table 2). Four-coordinated Fe, such as suggested by Nasdala *et al.* (2003) for a natural zircon sample, was similarly not found by our study.

In closing, we cannot comment on previous findings that the pink colour found in zircon pigments is due to hematite inclusions (*e.g.*, Berry *et al.*, 1996; Tartaj *et al.*, 1997; Ball & van Wyk, 2000; Llusar *et al.*, 2001; Ardizzone *et al.*, 2002; Carreto Cortés *et al.*, 2004). Even though the presence of hematite was confirmed, our samples did not show notable pink colouration. This may be due to too low hematite content: in the present study the maximum Fe_2O_3 content was 0.55 wt%, as opposed to up to 3.5 mol% Fe_2O_3 in Carreto Cortés *et al.* (2004) or 1.82 wt% in Berry *et al.* (1996).

Conclusions

Iron was found in synthetic zircon both in the form of hematite inclusions (α-Fe_2O_3) and incorporated in the zircon structure. These results suggest that in natural zircon the presence of elevated concentrations of Fe may be as oxide phases (*e.g.*, hematite), even if the resolution of imaging and analysis methods does not allow one to identify them. In this study, most of the Fe in the zircon structure was located in octahedral, interstitial sites, whereas only a small fraction was found to replace Zr in the dodecahedral site. Four-coordinated Fe substituting for Si was not detected. Phosphorus was found to replace Si. However, interstitial Fe (in contrast to Fe replacing Zr) introduces excess positive charge and hence cannot be charge-compensated by P–Si substitution alone. Although the nature of Fe in natural zircon still remains controversial, we may safely say that high Fe concentration in zircon is a reliable indicator of alteration. If iron is found in the wt% range, it is likely hosted by Fe oxide phases.

Acknowledgements: The Mexdist program for Mössbauer data modelling was generously made available to us by Eddy de Grave and Toon van Alboom at the University of Ghent, in Belgium. The authors are grateful to Andreas Wagner for sample preparation. This study was partially funded by the European Commission through contract no. MEXC-CT-2005-024878 and by the Austrian Science Fund (FWF) through grant no. P20028-N10.

References

Ardizzone, S., Binaghi, L., Cappelletti, G., Fermo, P. & Gilardoni, S. (2002): Iron doped zirconium silicate prepared by a sol–gel procedure. The effect of the reaction conditions on the structure, morphology and optical properties of the powders. *Phys. Chem. Chem. Phys.*, **4**, 5683–5689.

Armstrong, J.T. (1991): Quantitative elemental analysis of individual microparticles with electron beam instruments. *in* "Electron Probe Quantitation", Heinrich, K.F.J. & Newbury, D.E., eds., Plenum Press, New York, London, 261–315.

Armstrong, J.T. (1995): CITZAF: a package of correction programs for the quantitative electron microbeam X-ray analysis of thick polished materials, thin films, and particles. *Microbeam Anal*, **4**, 177–200.

Ball, D. & van Wyk, J.A. (2000): The electron paramagnetic resonance of Fe^{3+} observed in two axial sites in synthetic single crystals of zircon ($ZrSiO_4$). *Phys. Stat. Sol. B*, **218**, 545–551.

Berry, F.J., Eadon, D., Holloway, J. & Smart, L.E. (1996): Iron-doped zirconium silicate. Part 1.–The location of iron. *J. Mater. Chem.*, **6**, 221–225.

Breiter, K., Förster, H.J. & Škoda, R. (2006): Extreme P-, Bi-, Nb-, Sc-, U- and F-rich zircon from fractionated perphosphorous granites: The peraluminous Podlesí granite system, Czech Republic. *Lithos*, **88**, 15–34.

Carreto Cortés, E., Montoya de la Fuente, J.A., Morgado, J., Piña Pérez, C., Cordoncillo, E. & Carda Castelló, J.B. (2004): Solid-solution formation in the synthesis of Fe-zircon. *J. Am. Ceram. Soc.*, **87**, 612–616.

Davis, D.W., Williams, I.S. & Krogh, T.E. (2003): Historical development of zircon geochronology. *in* "Zircon", Hanchar, J.M. & Hoskin, P.W.O., eds., Mineralogical Society of America, Washington, D.C., 145–181.

Ewing, R.C., Lutze, W. & Weber, W.J. (1995): Zircon: A host phase for the disposal of weapons plutonium. *J. Mater. Res.*, **10**, 243–246.

Ewing, R.C., Meldrum, A., Wang, L., Weber, W.J. & Corrales, L.R. (2003): Radiation effects in zircon. *in* "Zircon", Hanchar, J.M. & Hoskin, P.W.O., eds., Mineralogical Society of America, Washington, D.C., 387–425.

Finch, R.J., Hanchar, J.M., Hoskin, P.W.O. & Burns, P.C. (2001): Rare-earth elements in synthetic zircon: Part 2. A single-crystal X-ray study of xenotime substitution. *Am. Mineral.*, **86**, 681–689.

Geisler, T., Rashwan, A.A., Rahn, M.K.W., Poller, U., Zwingmann, H., Pidgeon, R.T., Schleicher, H. & Tomaschek, F. (2003): Low-temperature hydrothermal alteration of natural metamict zircons from the Eastern Desert, Egypt. *Mineral. Mag.*, **67**, 485–508.

Geisler, T., Burakov, B.E., Zirlin, V., Nikolaeva, L. & Pöml, P. (2005): A Raman spectroscopic study of high-uranium zircon from the Chernobyl "lava". *Eur. J. Mineral.*, **17**, 883–894.

Görz, H. (1974): Microprobe studies of inclusions in zircons and compilation of minor and trace elements in zircons from the literature. *Chem. Erde*, **33**, 326–357.

Habermann, A. (2002): Quantitative cathodoluminescence (CL) spectroscopy of minerals: possibilities and limitations. *Mineral. Petrol.*, **76**, 247–259.

Hanchar, J.M., Finch, R.J., Hoskin, P.W.O., Watson, E.B., Cherniak, D.J. & Mariano, A.N. (2001): Rare earth elements in synthetic zircon: Part 1. Synthesis, and rare earth element and phosphorus doping. *Am. Mineral.*, **86**, 667–680.

Hoskin, P.W.O. & Ireland, T.R. (2000): Rare earth element chemistry of zircon and its use as a provenance indicator. *Geology*, **28**, 627–630.

Hoskin, P.W.O. & Schaltegger, U. (2003): The composition of zircon and igneous and metamorphic petrogenesis. *in* "Zircon", Hanchar, J.M. & Hoskin, P.W.O., eds., Mineralogical Society of America, Washington, D.C., 27–62.

Irmer, G. (1985): Zum Einfluh der Apparatefunktion auf die Bestimmung von Streuquerschnitten und Lebensdauern aus optischen Phononenspektren. *Exp. Tech. Phys.*, **33**, 501–506.

Johan, Z. & Johan, V. (2005): Accessory minerals of the Cínovec (Zinnwald) granite cupola, Czech Republic: indicators of petrogenetic evolution. *Mineral. Petrol.*, **83**, 113–150.

Llusar, M., Calbo, J., Badenes, J.A., Tena, M.A. & Monrós, G. (2001): Synthesis of iron zircon coral by coprecipitation routes. *J. Mater. Sci.*, **36**, 153–163.

Nasdala, L., Irmer, G. & Wolf, D. (1995): The degree of metamictization in zircon: a Raman spectroscopic study. *Eur. J. Mineral.*, **7**, 471–478.

Nasdala, L., Zhang, M., Kempe, U., Panczer, G., Gaft, M., Andrut, M. & Plötze, M. (2003): Spectroscopic methods applied to zircon. *in* "Zircon", Hanchar, J.M. & Hoskin, P.W.O., eds., Mineralogical Society of America, Washington, D.C., 427–467.

Nasdala, L., Reiners, P.W., Garver, J.I., Kennedy, A.K., Stern, R.A., Balan, E. & Wirth, R. (2004): Incomplete retention of radiation damage in zircon from Sri Lanka. *Am. Mineral.*, **89**, 219–231.

Nasdala, L., Hanchar, J.M., Kronz, A. & Whitehouse, M.J. (2005): Long-term stability of alpha particle damage in natural zircon. *Chem. Geol.*, **220**, 83–103.

Nasdala, L., Hanchar, J.M., Rhede, D., Kennedy, A.K. & Váczi, T. (2009a): Retention of uranium in complexly altered zircon: An example from Bancroft, Ontario. *Chem. Geol.*, 10.1016/j.chemgeo.2009.10.004 (in press).

Nasdala, L., Kronz, A., Wirth, R., Váczi, T., Pérez-Soba, C., Willner, A. & Kennedy, A.K. (2009b): The phenomenon of deficient electron microprobe totals in radiation-damaged and altered zircon. *Geochim. Cosmochim. Acta*, **73**, 1637–1650.

Neuser, R.D., Bruhn, F., Götze, J., Habermann, D. & Richter, D.K. (1995): Kathodolumineszenz: Methodik und Anwendung. *Zbl. Geol. Paläont. I*, **1995**, 287–306.

Pearce, N.J.G., Perkins, W.T., Westgate, J.A., Gorton, M.P., Jackson, S.E., Neal, C.R. & Chenery, S.P. (1997): A compilation of new and published major and trace element data for NIST SRM 610 and NIST SRM 612 glass reference materials. *Geostandards Newslett., J. Geostandards Geoanal.*, **21**, 115–144.

Robinson, K., Gibbs, G.V. & Ribbe, P.H. (1971): The structure of zircon: A comparison with garnet. *Am. Mineral.*, **56**, 782–790.

Smith, D.G.W., de St. Jorre, L., Reed, S.J.B. & Long, J.V.P. (1991): Zonally metamictized and other zircons from Thor Lake, Northwest Territories. *Can. Mineral.*, **29**, 301–309.

Speer, J.A. (1980): Zircon. *in* "Orthosilicates", Ribbe, P.H., ed. Mineralogical Society of America, Washington, D.C., 67–112.

Tartaj, P., González-Carreño, T., Serna, C.J. & Ocaña, M. (1997): Iron zircon pigments prepared by pyrolysis of aerosols. *J. Solid State Chem.*, **128**, 102–108.

Watson, E.B. & Harrison, T.M. (2005): Zircon thermometer reveals minimum melting conditions on earliest Earth. *Science*, **308**, 841–844.

Wopenka, B., Jolliff, B.L., Zinner, E. & Kremser, D.T. (1996): Trace element zoning and incipient metamictization in a lunar zircon: Application of three microprobe techniques. *Am. Mineral.*, **81**, 902–912.

Submitted 11 Nov 2009

Online supporting material

These pages contain a hard copy of the online supporting material. Figure O1 shows the correlations in selected chemical data, whereas Table O1 (overleaf) presents the full EPMA data set measured on the ^{57}Fe-doped synthetic zircon.

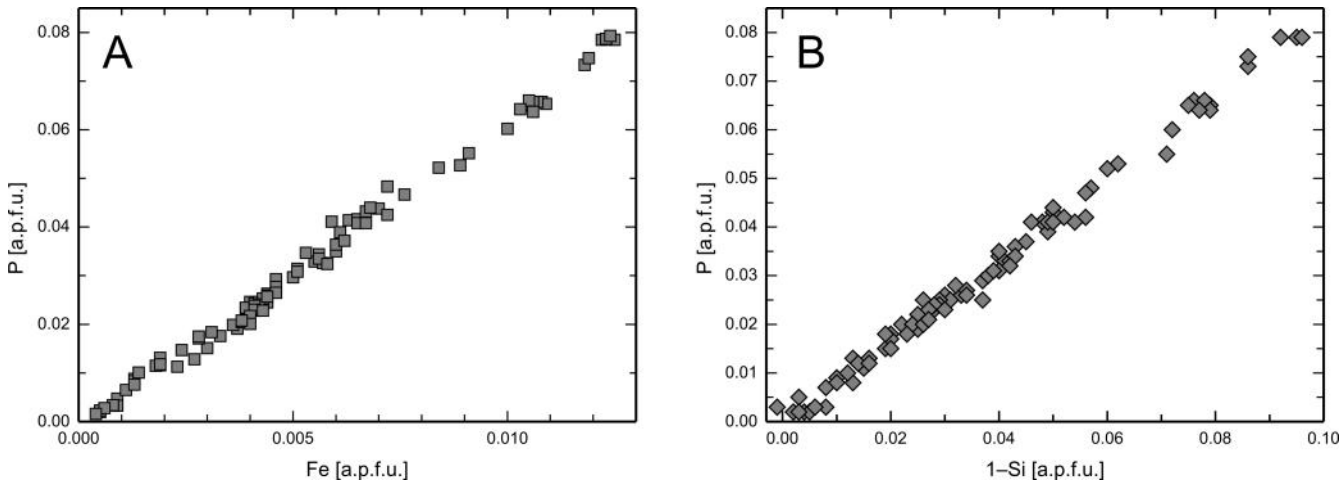

Fig. O1. (A) Plot showing the correlation between Fe and P concentrations. The ratio of P to Fe is 6.36. (B) Plot showing Si deficiency *vs.* P concentration.

Table O1. The full set of EPMA analyses.

No.	Analysis spot	zone	ZrO_2 [wt%]	SiO_2 [wt%]	P_2O_5 [wt%]	Fe_2O_3 [wt%]	Total [wt%]	Zr [apfu]	Si [apfu]	P [apfu]	Fe [apfu]	Total cation [apfu]
1	Line1Fe_Zrc01	high CL	66.7	31.4	1.33	0.24	99.7	0.99	0.96	0.03	0.01	1.99
2	Line2Fe_Zrc01	high CL	67.0	31.5	1.27	0.24	99.9	1.00	0.96	0.03	0.01	1.99
3	Line3Fe_Zrc01	high CL	67.3	31.6	1.22	0.22	100.2	1.00	0.96	0.03	0.01	1.99
4	Line4Fe_Zrc01	high CL	67.2	31.7	1.14	0.20	100.2	1.00	0.96	0.03	0.00	1.99
5	Line5Fe_Zrc01	high CL	67.2	31.8	1.04	0.20	100.2	1.00	0.97	0.03	0.00	1.99
6	Line6Fe_Zrc01	high CL	67.3	31.8	1.02	0.19	100.3	1.00	0.97	0.03	0.00	1.99
7	Line7Fe_Zrc01	high CL	67.2	31.9	0.94	0.19	100.3	1.00	0.97	0.02	0.00	2.00
8	Line8Fe_Zrc01	high CL	67.4	32.1	0.74	0.16	100.4	1.00	0.97	0.02	0.00	2.00
9	Line9Fe_Zrc01	rim (low CL)	67.1	32.2	0.59	0.13	100.0	1.00	0.98	0.02	0.00	2.00
10	Line10Fe_Zrc01	rim (low CL)	67.3	32.3	0.44	0.10	100.2	1.00	0.98	0.01	0.00	2.00
11	Line1Fe_Zrc02	high CL	66.9	31.1	1.88	0.32	100.2	0.99	0.94	0.05	0.01	1.99
12	Line2Fe_Zrc02	high CL	66.8	31.2	1.70	0.31	100.0	0.99	0.95	0.04	0.01	1.99
13	Line3Fe_Zrc02	high CL	66.9	31.3	1.59	0.29	100.0	0.99	0.95	0.04	0.01	1.99
14	Line4Fe_Zrc02	high CL	67.0	31.4	1.60	0.26	100.3	0.99	0.95	0.04	0.01	1.99
15	Line5Fe_Zrc02	high CL	67.2	31.7	1.35	0.23	100.5	0.99	0.96	0.03	0.01	1.99
16	Line6Fe_Zrc02	high CL	67.3	32.0	1.08	0.20	100.5	0.99	0.97	0.03	0.00	1.99
17	Line7Fe_Zrc02	high CL	67.0	32.0	0.95	0.18	100.2	0.99	0.97	0.02	0.00	1.99
18	Line8Fe_Zrc02	high CL	67.2	32.2	0.77	0.16	100.3	0.99	0.98	0.02	0.00	2.00
19	Line9Fe_Zrc02	high CL	67.1	32.3	0.68	0.14	100.2	1.00	0.98	0.02	0.00	2.00
20	Line10Fe_Zrc02	rim (low CL)	67.1	32.5	0.49	0.12	100.1	0.99	0.99	0.01	0.00	2.00
22	Line2Fe_Zrc03	high CL	67.5	31.7	0.98	0.19	100.3	1.00	0.96	0.03	0.00	1.99
23	Line3Fe_Zrc03	high CL	67.0	30.5	2.14	0.40	100.0	1.00	0.93	0.06	0.01	1.99
24	Line4Fe_Zrc03	high CL	67.6	31.1	1.63	0.29	100.6	1.00	0.94	0.04	0.01	1.99
25	Line5Fe_Zrc03	high CL	67.2	31.1	1.61	0.28	100.2	1.00	0.95	0.04	0.01	1.99
26	Line6Fe_Zrc03	high CL	67.1	31.2	1.61	0.28	100.1	0.99	0.95	0.04	0.01	1.99
27	Line7Fe_Zrc03	high CL	67.1	31.3	1.51	0.27	100.1	1.00	0.95	0.04	0.01	1.99
28	Line8Fe_Zrc03	high CL	67.0	31.3	1.68	0.29	100.3	0.99	0.95	0.04	0.01	1.99
29	Line9Fe_Zrc03	high CL	67.5	31.7	1.27	0.25	100.7	1.00	0.96	0.03	0.01	1.99
30	Line10Fe_Zrc03	rim (low CL)	67.3	32.6	0.34	0.06	100.3	1.00	0.99	0.01	0.00	2.00
31	Line1Fe_Zrc04	rim (low CL)	67.3	32.8	0.08	0.02	100.2	1.00	1.00	0.00	0.00	2.00
32	Line2Fe_Zrc04	high CL	67.3	32.3	0.66	0.12	100.3	1.00	0.98	0.02	0.00	2.00
33	Line3Fe_Zrc04	high CL	67.4	32.0	0.95	0.18	100.4	1.00	0.97	0.02	0.00	1.99
34	Line4Fe_Zrc04	high CL	67.2	31.9	0.95	0.18	100.1	1.00	0.97	0.02	0.00	1.99
35	Line5Fe_Zrc04	high CL	67.2	32.0	1.01	0.19	100.4	0.99	0.97	0.03	0.00	1.99
36	Line6Fe_Zrc04	high CL	67.1	31.9	0.95	0.19	100.2	0.99	0.97	0.02	0.00	1.99
37	Line7Fe_Zrc04	high CL	67.4	31.9	0.98	0.19	100.5	1.00	0.97	0.03	0.00	1.99
38	Line8Fe_Zrc04	high CL	67.3	32.1	0.99	0.19	100.5	0.99	0.97	0.03	0.00	1.99
39	Line9Fe_Zrc04	high CL	67.1	32.0	0.90	0.17	100.2	1.00	0.97	0.02	0.00	2.00
40	Line10Fe_Zrc04	rim (low CL)	67.1	32.7	0.18	0.04	100.1	1.00	1.00	0.00	0.00	2.00
41	Line1Fe_Zrc05	rim (low CL)	67.3	32.6	0.25	0.05	100.2	1.00	0.99	0.01	0.00	2.00
42	Line2Fe_Zrc05	high CL	66.9	31.6	1.36	0.26	100.1	0.99	0.96	0.04	0.01	1.99
43	Line3Fe_Zrc05	centre (low CL)	66.6	30.5	2.33	0.44	99.9	0.99	0.93	0.06	0.01	1.99
44	Line4Fe_Zrc05	centre (low CL)	66.7	30.4	2.55	0.47	100.1	0.99	0.92	0.07	0.01	1.99
45	Line5Fe_Zrc05	centre (low CL)	66.7	30.3	2.54	0.48	100.1	0.99	0.92	0.07	0.01	1.99
46	Line6Fe_Zrc05	centre (low CL)	66.6	30.4	2.55	0.47	100.0	0.99	0.92	0.07	0.01	1.99
47	Line7Fe_Zrc05	centre (low CL)	66.7	30.4	2.55	0.46	100.1	0.99	0.92	0.07	0.01	1.99
48	Line8Fe_Zrc05	centre (low CL)	66.6	30.4	2.52	0.46	100.0	0.99	0.93	0.07	0.01	1.99
49	Line9Fe_Zrc05	high CL	67.2	31.6	1.42	0.26	100.5	0.99	0.96	0.04	0.01	1.99
50	Line10Fe_Zrc05	rim (low CL)	66.9	32.2	0.45	0.08	99.7	1.00	0.99	0.01	0.00	2.00
52	Line2Fe_Zrc06	high CL	67.1	32.0	0.91	0.17	100.1	1.00	0.97	0.02	0.00	2.00
53	Line3Fe_Zrc06	high CL	67.0	31.9	0.88	0.18	100.0	1.00	0.97	0.02	0.00	2.00
54	Line4Fe_Zrc06	high CL	67.0	31.9	0.94	0.18	100.0	1.00	0.97	0.02	0.00	1.99
55	Line5Fe_Zrc06	high CL	67.2	32.0	0.93	0.18	100.3	1.00	0.97	0.02	0.00	1.99
56	Line6Fe_Zrc06	high CL	67.5	32.0	0.89	0.18	100.6	1.00	0.97	0.02	0.00	2.00
57	Line7Fe_Zrc06	high CL	67.2	32.1	0.84	0.17	100.3	0.99	0.98	0.02	0.00	2.00
58	Line8Fe_Zrc06	high CL	67.5	32.2	0.80	0.17	100.7	1.00	0.98	0.02	0.00	2.00
59	Line9Fe_Zrc06	high CL	67.3	32.4	0.72	0.14	100.5	0.99	0.98	0.02	0.00	2.00
60	Line10Fe_Zrc06	rim (low CL)	67.1	32.9	0.13	0.04	100.2	0.99	1.00	0.00	0.00	2.00
61	Line1Fe_Zrc07	high CL	66.8	31.3	1.71	0.30	100.1	0.99	0.95	0.04	0.01	1.99
62	Line2Fe_Zrc07	high CL	67.2	31.4	1.59	0.28	100.4	0.99	0.95	0.04	0.01	1.99
63	Line3Fe_Zrc07	high CL	67.2	31.5	1.45	0.27	100.4	0.99	0.95	0.04	0.01	1.99
64	Line4Fe_Zrc07	high CL	67.1	32.0	0.89	0.19	100.2	1.00	0.97	0.02	0.00	2.00
65	Line5Fe_Zrc07	high CL	67.4	32.1	0.78	0.18	100.4	1.00	0.97	0.02	0.00	2.00
66	Line6Fe_Zrc07	high CL	67.3	32.0	0.81	0.16	100.2	1.00	0.97	0.02	0.00	2.00
67	Line7Fe_Zrc07	high CL	67.4	32.2	0.68	0.12	100.4	1.00	0.98	0.02	0.00	2.00
68	Line8Fe_Zrc07	rim (low CL)	67.4	32.4	0.51	0.08	100.4	1.00	0.98	0.01	0.00	2.00
69	Line9Fe_Zrc07	rim (low CL)	67.5	32.4	0.32	0.06	100.3	1.00	0.99	0.01	0.00	2.00
70	Line10Fe_Zrc07	rim (low CL)	67.6	32.6	0.13	0.04	100.3	1.00	0.99	0.00	0.00	2.00
71	Line1Fe_Zrc08	rim (low CL)	67.6	32.8	0.08	0.02	100.4	1.00	1.00	0.00	0.00	2.00
72	Line2Fe_Zrc08	rim (low CL)	67.4	32.5	0.30	0.06	100.3	1.00	0.99	0.01	0.00	2.00
73	Line3Fe_Zrc08	high CL	67.3	31.8	1.03	0.20	100.4	1.00	0.97	0.03	0.00	1.99
74	Line4Fe_Zrc08	high CL	66.7	30.8	2.04	0.39	99.9	0.99	0.94	0.05	0.01	1.99
75	Line5Fe_Zrc08	centre (low CL)	66.5	30.1	2.85	0.52	99.9	0.99	0.91	0.07	0.01	1.98
76	Line6Fe_Zrc08	centre (low CL)	66.5	29.9	3.05	0.55	100.1	0.98	0.91	0.08	0.01	1.98
77	Line7Fe_Zrc08	centre (low CL)	66.7	30.4	2.57	0.46	100.1	0.99	0.92	0.07	0.01	1.99
78	Line8Fe_Zrc08	high CL	67.1	31.1	1.82	0.33	100.3	0.99	0.94	0.05	0.01	1.99
79	Line9Fe_Zrc08	high CL	67.3	32.4	0.45	0.08	100.2	1.00	0.99	0.01	0.00	2.00
80	Line10Fe_Zrc08	rim (low CL)	67.5	32.7	0.09	0.02	100.3	1.00	1.00	0.00	0.00	2.00
81	Line1Fe_Zrc09	rim (low CL)	67.4	32.3	0.46	0.08	100.3	1.00	0.98	0.01	0.00	2.00
82	Line2Fe_Zrc09	high CL	67.2	31.3	1.65	0.32	100.4	0.99	0.95	0.04	0.01	1.99
83	Line3Fe_Zrc09	centre (low CL)	67.1	30.4	2.48	0.46	100.5	0.99	0.92	0.06	0.01	1.99
84	Line4Fe_Zrc09	centre (low CL)	66.6	30.1	2.91	0.52	100.1	0.98	0.91	0.07	0.01	1.98
85	Line5Fe_Zrc09	centre (low CL)	66.7	30.0	3.06	0.54	100.2	0.98	0.91	0.08	0.01	1.98
86	Line6Fe_Zrc09	centre (low CL)	66.7	29.8	3.06	0.54	100.1	0.99	0.91	0.08	0.01	1.98
87	Line7Fe_Zrc09	centre (low CL)	66.8	29.8	3.09	0.54	100.2	0.99	0.90	0.08	0.01	1.98
88	Line8Fe_Zrc09	centre (low CL)	66.9	30.4	2.50	0.45	100.3	0.99	0.92	0.06	0.01	1.99
89	Line9Fe_Zrc09	high CL	66.9	31.0	2.03	0.37	100.2	0.99	0.94	0.05	0.01	1.99
90	Line10Fe_Zrc09	high CL	67.4	31.8	1.00	0.19	100.5	1.00	0.97	0.03	0.00	1.99
91	Line1Fe_ZrC10	rim (low CL)	67.6	32.7	0.11	0.03	100.4	1.00	0.99	0.00	0.00	2.00
92	Line2Fe_ZrC10	high CL	67.6	32.3	0.57	0.11	100.5	1.00	0.98	0.01	0.00	2.00
93	Line3Fe_ZrC10	high CL	67.2	31.6	1.15	0.22	100.3	1.00	0.96	0.03	0.01	1.99
94	Line4Fe_ZrC10	high CL	67.1	31.3	1.59	0.29	100.3	0.99	0.95	0.04	0.01	1.99
95	Line5Fe_ZrC10	high CL	67.3	31.5	1.30	0.24	100.4	1.00	0.96	0.03	0.01	1.99
97	Line7Fe_ZrC10	high CL	67.4	31.6	1.26	0.25	100.5	1.00	0.96	0.03	0.01	1.99
98	Line8Fe_ZrC10	high CL	67.3	31.6	1.20	0.22	100.3	1.00	0.96	0.03	0.01	1.99
99	Line9Fe_ZrC10	rim (low CL)	67.4	32.5	0.39	0.06	100.3	1.00	0.99	0.01	0.00	2.00
100	Line10Fe_ZrC10	rim (low CL)	67.6	32.8	0.06	0.02	100.5	1.00	1.00	0.00	0.00	2.00
Min			66.5	29.8	0.08	0.02	99.7	0.98	0.90	0.00	0.00	1.98
Max			67.6	32.9	3.09	0.55	100.7	1.00	1.00	0.08	0.01	2.00
Average			67.1	31.6	1.27	0.24	100.2	0.99	0.96	0.03	0.01	1.99
Median			67.2	31.8	1.03	0.20	100.2	1.00	0.97	0.03	0.00	1.99
Standard deviation (1s)			0.3	0.8	0.80	0.14	0.2	0.00	0.02	0.02	0.00	0.00